AGARD-R-703

AGARD-R-703

AGARD

ADVISORY GROUP FOR AEROSPACE RESEARCH & DEVELOPMENT

7 RUE ANCELLE 92200 NEUILLY SUR SEINE FRANCE

AGARD REPORT No. 703

Recent Transonic Flutter Investigations for Wings and External Stores

NORTH ATLANTIC TREATY ORGANIZATION

DISTRIBUTION AND AVAILABILITY ON BACK COVER

NORTH ATLANTIC TREATY ORGANIZATION

ADVISORY GROUP FOR AEROSPACE RESEARCH AND DEVELOPMENT

(ORGANISATION DU TRAITE DE L'ATLANTIQUE NORD)

AGARD Report No.703

RECENT TRANSONIC FLUTTER INVESTIGATIONS FOR WINGS AND EXTERNAL STORES

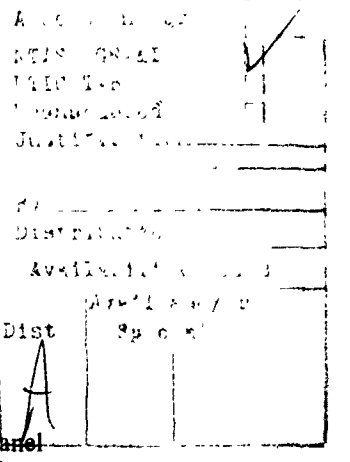

Papers presented at the 56th Structures and Materials Panel Meeting held in Toronto, Canada in September 1982

THE MISSION OF AGARD

The mission of AGARD is to bring together the leading personalities of the NATO nations in the fields of science and technology relating to aerospace for the following purposes

- Exchanging of scientific and technical information,
- Continuously stimulating advances in the aerospace sciences relevant to strengthening the common defence posture,
- Improving the co-operation among member nations in aerospace research and development,
- Providing scientific and technical advice and assistance to the North Atlantic Military Committee in the field of aerospace research and development,
- Rendering scientific and technical assistance, as requested, to other NATO bodies and to member nations in connection with research and development problems in the aerospace field,
- Providing assistance to member nations for the purpose of increasing their scientific and technical potential,
- Recommending effective ways for the member nations to use their research and development capabilities for the common benefit of the NATO community

The highest authority within AGARD is the National Delegates Board consisting of officially appointed senior representatives from each member nation. The mission of AGARD is carried out through the Panels which are composed of experts appointed by the National Delegates, the Consultant and Exchange Programme and the Aerospace Applications Studies Programme. The results of AGARD work are reported to the member nations and the NATO Authorities through the AGARD series of publications of which this is one.

Participation in AGARD activities is by invitation only and is normally limited to citizens of the NATO nations

Published January 1983

ISBN 92-835-1443-2

Printed by Specialised Printing Services Limited
40 Chigwell Lane, Loughton, Essex IG10 3TZ

PREFACE

The AGARD/SMP Subcommittee on "Aeroelasticity" heard four technical papers at the Fall 82 meeting in Toronto, Canada. Three of the papers represent a cross section of recent activities in aeroelasticity, covering subsonic flutter-clearance procedures in Canada, transonic flutter research in Germany, and transonic unsteady aerodynamic measurements in the United States. A fourth paper by Dr Erwin Johnson of the United States discussed very promising results Northrop has achieved in developing an adaptive flutter-suppression system. Wind tunnel tests on an aeroelastic model of a wing with external stores demonstrated rapid sensing of a suddenly violent flutter mode, computation of desired control system gains and phases, and resulting suppression of the flutter-instability. All four papers indicate the great strides being made in aeroelasticity by the NATO countries and promise even greater understanding and progress within the next few years.

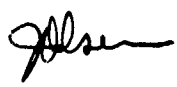

JAMES J.OLSEN
Chairman, Subcommittee on Aeroelasticity

CONTENTS

A CANADIAN APPROACH TO FLUTTER CLEARANCE FOR EXTERNAL STORES

by

B.H.K. Lee*
National Aeronautical Establishment
National Research Council Canada
Ottawa, Ontario, Canada

and

J.H. Goodey+
Canadair Limited
Montreal, Quebec, Canada

ABSTRACT

The Canadian capability in flutter clearance of military aircraft carrying underwing stores is reviewed. The flight test facilitie and procedures, on-line analogue and post-flight digital data analysis, and analytical flutter model are described. Some results for the LAU-5003/A rocket launchers carrying C14 rockets armed with Mk I warheads are presented. Frequencies and damping values obtained from strip derivatives and doublet lattice aerodynamics methods used in the flutter computational code are discussed. Experimental results from on-line and post-flight analyses are compared for one aircraft/store configuration.

1.0 INTRODUCTION

Most certification programs for Canadian aircraft with external stores were in the past performed by the manufacturer of the aircraft, USAF or the Netherlands. Reliance on a foreign country's clearance program whose requirements were not identical with the Canadian requirements could result in Canada having to compromise some of its operational options for usage of the program. In 1972 (Ref. 1) a study for an "in house" certification program to meet Canadian needs was completed and it was concluded in the report that an independent Canadian capability for external stores was technically feasible and economically justifiable. Such a capability would free the Canadian Forces from the constraints of foreign bias and allow for a flexible choice in the selection of a foreign-domestic mix of aircraft and stores.

The first of an "all Canadian" effort in stores clearance on the CF-5 aircraft was in 1981 at Cold Lake CFB. Prior to that, clearance on the CF-5 was contracted to National Aerospace Laboratory (NLR) of the Netherlands. The flight test techniques adopted by the Canadian Forces were similar to those which had proved reasonably successful in previous Netherlands tests on their NF-5 aircraft and in a CF/NLR program on the CF-5 (Ref. 2).

This paper gives an overview of the flutter phase of the stores clearance program. The major participants in this multi-agency effort are the Aerospace Engineering Test Establishment of the Canadian Forces, Canadair Limited and the National Aeronautical Establishment. The flight test facilities and procedures, on-line analogue and post-flight digital data analysis, and analytical flutter model will be described. The discussions will be limited to the CF-5 aircraft carrying LAU-5003/A stores fitted with nose cones.

2.0 FLUTTER FLIGHT TESTS

An essential part of a certification program is to investigate whether the aircraft is safe from flutter for all stores configurations within the proposed flight régime. Generally, the flutter investigation is carried out both experimentally and analytically. The analytic modelling will be described in a later section. The flutter calculations include a large number of possible stores configurations, and some of the more critical ones are usually selected for flutter flight testing so that the estimated damping margins can be confirmed by measurements.

2.1 Ground Vibration Testing

For the safe carriage of LAU-5003/A stores on the CF-5 aircraft, flutter flight tests were carried out at Cold Lake CFB during February and March of 1981. In the pre-flight flutter analysis, ground vibration testing (GVT) had been performed (Ref. 3) and the data used in the calculations of flutter trends which formed the basis for flight testing. Since no suitable ground vibration testing facility was available in Canada for stores clearance work, the data for the LAU-5003A/C14 launcher/weapon configurations on the CF-5 aircraft was obtained from a joint USAF/CF test program at the Air Force Armament Laboratory at Eglin AFB between September-October of 1979.

The vibration tests were conducted in the Overhead Soft Suspension System in which four cables were attached to the jack/hoist adapters on the aircraft fuselage as shown in Figure 1. Each cable was suspended from an Air Spring Isolator, and this arrangement provided excellent aircraft stability for modal testing with the landing gear retracted. Two shakers were used for exciting the aircraft structure. For most of the configurations, the shakers were attached at the tip tanks, while in other configurations they were attached to the outboard stores.

A block diagram of the data acquisition and analysis system is shown in Figure 2. A total of 83 accelerometers were used to measure modal response and two load cells (one at each shaker) provided force input data. Most of the accelerometers were installed on the right wing to give a detailed vibration characteristic of the wing. Since only 32 channels of data could be analyzed at a time, the accelerometer signals were separated in three multiplexed sets with a common reference included in each set. The data could be either stored on disk for future analysis or fed directly to a fast fourier analyzer. The modal amplitude and phase information were sent by direct line to a CDC 6600 computer for additional manipulation and graphic display.

---

* Senior Research Officer, High Speed Aerodynamics Laboratory

\+ Senior Staff Specialist, Flight Sciences

For validation purposes, the GVT results were compared with those determined by the Netherlands for the NF-5 aircraft. A comparison of the resonant frequencies for the two aircraft are shown in the following table:

MODE		NLR NF-5GVT	EGLIN CF-5GVT
Wing 1st Bending	Sym	3.69 Hz	3.63 Hz
Wing 1st Torsion	Sym	5.93 Hz	5.87 Hz
Wing 1st Torsion	A/S	5.67 Hz	5 74 Hz
Wing 1st Bending	A/S	6.67 Hz	7.14 Hz
OTBD Store Yaw	A/S	9.01 Hz	9.53 Hz
Centerline Tank Roll	A/S	10.03 Hz	10.08 Hz

The results are very close since the two aircraft are structurally very similar; the primary difference is that the NF-5 is configured with a maneuvering leading edge flap whereas the CF-5 has the standard flap.

2.2 Aircraft and Airborne Instrumentation

Figure 3 shows a CF-5 test aircraft fitted with centerline tank and carrying two LAU-5003/A stores at the outboard station. A view of an empty rocket launcher with the nose cone removed is given in Figure 4. The launcher may be loaded with from one to nineteen C14 rockets, fitted with either six, ten or sixteen pound warheads.

The test aircraft was equipped with the necessary test instrumentation for determining the flight conditions which included the flight altitude, indicated airspeed, total temperature, position of elevator and aileron, yaw/pitch/roll rate and angle of attack. For flutter analysis purposes, eight accelerometers were installed on the aircraft (Fig 5). Four of them were positioned at the front and rear of the tip tanks and these were the primary ones used for flutter investigation. The remaining four accelerometers were located at the nose of the stores and served mainly to provide data in the vibration of the stores. All accelerometers were of the piezoelectric type.

Figure 6 shows the airborne data system. To provide data acquisition back-up, all data transmitted to the ground station was also recorded onboard. The recording signal conditioning and telemetry transmission equipment were housed in the left-hand nose gun bay. No special equipment was provided for the stick pulse excitation. For simplicity, this was achieved by rapping the stick directly, either laterally or longitudinally as appropriate. The aircraft was fitted with aileron and elevator position sensors, and these signals were used for triggering the start of analysis of the Fourier analyzer.

2.3 Ground Station and Instrumentation

Most of the flight testing was performed in airspace over the Primrose Lake Evaluation Range approximately 30 miles north of the Cold Lake CF base. This range was equipped with cinetheodolites, tracking radar, a range trials control center and an auto tracking antenna. Data sent from the aircraft was transmitted to the ground station where data acquisition and analysis were performed (Fig. 7). The serial PCM telemetry data was processed through decommutation and word selection systems to provide parallel display of selected channels on a strip chart recorder. Other parallel data feeds were supplied to a Hewlett-Packard Fourier Analyzer and the spectra could be displayed both on an oscilloscope or X-Y plotter. A data flow schematic for the ground station is shown in Figure 8. Digital tapes for post-flight processing could be written simultaneously during data acquisition or afterwards by playback of PCM data from the analogue tapes.

2.4 Test Procedure

The basic procedure adopted was to excite the airframe by means of control pulse inputs generated by stick raps. The airframe response, as sensed by the accelerometers, was then monitored and analyzed to determine frequencies and damping of the modes of interest.

The sequence of the various flight tests was chosen in such a manner that the chance of encountering flutter during a flight would become greater as the test program proceeded. In this way, it was assured that the test team would have acquired a certain level of experience before entering the more critical configurations For the LAU-5003/A trials, tests were performed at an altitude of approximately 7,000 ft above sea level. To minimize fuel used in achieving the required test conditions, the flight technique adopted was to trade-off altitude for speed; pulling up after each test point and diving to achieve the next. When a given test point was stabilized, the pilot was then given the instruction to initiate a lateral stick pulse. After the stick rap, the pilot remained hands-off for a sufficient time for the response to decay before recovering. If the response records were satisfactory, the pilot was cleared to proceed with the longitudinal stick pulse followed by a speed reduction prior to clearance to the next speed increment.

The limitations of flight duration was always a primary constraint, especially when obtaining the higher speed points. The test aircraft was at all times accompanied by a safety/chase aircraft. Since this aircraft was also required for other test flying, it was not equipped with external tanks. Consequently the higher duration available when the test aircraft was carrying inboard fuel tanks was not fully realized and the flight time was limited by chase aircraft fuel limits.

The aircraft was flown in a 'dogbone' pattern as shown in Figure 9. With the out and back headings shown in the figure, optimum telemetry reception could be achieved except when turning. This pattern was later modified by extending it directly over

the ground station and out to a similar distance to the southwest. In spite of a brief loss of signal when the aircraft was over the ground station, this modification resulted in improved flight efficiency.

2.5 Measurement Procedure

Representing the aerodynamic forces generated by the stick pulses as an impulse or delta function, the resulting response of the aircraft can be represented by a decaying time function as shown in Figure 10a. For single mode response, frequency and damping can be obtained using the usual logarithmic decrement method. More commonly, however, the response of the aircraft is composed of several modes of vibration, and spectral analysis must be used instead. Figure 10b shows how damping can be obtained using the half-power and central frequency method.

Based on analytical predictions and on previous experience, four structural modes were of primary interest in the LAU-5003/A flutter trials. They were the symmetric and anti-symmetric wing bending and torsional modes. To improve identification of individual modes, power spectral densities were obtained for four different linear combinations of the four accelerometer signals. Each linear combination was aimed at enhancing the power spectrum of one of the four modes of interest, and the signal summations used are summarized in Figure 11. These summations could be done readily on the HP 5451B analyzer since the machine could be programmed to do arithmetic operations on the four input signals before performing the Fourier transform.

Frequency range up to 10 Hz was desired for the power spectral densities since this range covered the important fundamental wing modes of interest. A data sampling frequency of 20 Hz was selected giving a frequency resolution of approximately 0.02 Hz for a block size of 1024. Since the response of the wing usually decayed to essentially ambient level within approximately 3 seconds of the stick rap, the analyzer was programmed to read data into a block size of 128 at 50 millisecond intervals. Positions beyond 80 were then set to zero keeping only the first 4 seconds of data. The block size was then switched to 1024. This resulted in the data being stored in the first 80 positions with the rest padded with zeros. In this way, the data acquisition time was kept to a minimum. The truncation error was considered to be within acceptable limits based on tests performed by NLF (Ref. 2).

The power spectral densities were displayed on an oscilloscope and on a X-Y plotter. Damping was determined by manual location of the central frequency and half power points. Based on the damping thus calculated, a decision was then made whether to proceed to the next higher speed test point. For quick look analysis and for monitoring during acceleration to the next test point, the time signals were displayed on a strip chart recorder which usually could indicate qualitatively the damping of the modes under investigation.

3.0 POST-FLIGHT DATA ANALYSIS

Damping values obtained from power spectral density plots are simple and direct with minimum subjective interpretations when the modes are adequately excited and the frequencies are sufficiently far apart. However, turbulence and buffet, which can be quite intense at the high Mach number tests, degrade the response signal making damping measurements difficult and uncertain. Also, for some store configurations in the LAU-5003/A trials, insufficient response of the anti-symmetric bending mode was detected since the node line for this mode ran across the aileron so that aileron forces did not produce sufficiently large acceleration in this mode for analysis purposes. In order that more reliable results can be obtained, an interactive computer program has been developed which is more versatile and accurate than analogue techniques. This program has been used mainly for post-flight data analysis, but it can also be used to supplement the on-line analogue monitoring of subcritical damping in flutter flight tests

3.1 Damping from Impulsive Input

Considering the symmetric and anti-symmetric bending and torsion modes to be the important ones in the flutter trials, the acceleration at location 'A' (Fig. 5) for a given excitation function can be written as follows:

$$Y_A(t) = f_A(t) + p_A(t) + n_A(t) \tag{1}$$

where $f_A(t)$ is a deterministic signal determined by the input excitation function, $p_A(t)$ is a random signal for the response due to turbulence or buffeting, and $n_A(t)$ is the noise in the measuring equipment. Equation (1) gives the general form of the response signal, and the only assumptions made for later analysis purposes are that f_A, p_A and n_A are uncorrelated, and p_A and n_A are statistically stationary. Similar expressions can be written for the signals from accelerometers 'B', 'C' and 'D'.

Treating the input as an impulse function, and neglecting $p_A(t)$ and $n_A(t)$ for the time being, Equation (1) can be written as:

$$\begin{aligned} Y_A(t) = {} & A^A_{SB} e^{-\alpha_{SB} t} \sin(\omega_{SB} t + \psi^A_{SB}) \\ & + A^A_{AB} e^{-\alpha_{AB} t} \sin(\omega_{AB} t + \psi^A_{AB}) \\ & + A^A_{ST} e^{-\alpha_{ST} t} \sin(\omega_{ST} t + \psi^A_{ST}) \\ & + A^A_{AT} e^{-\alpha_{AT} t} \sin(\omega_{AT} t + \psi^A_{AT}) \end{aligned} \tag{2}$$

where A is the amplitude of the vibratory signal of one mode, ω is the circular frequency, t is the time, α is the damping and ψ is the phase angle. The subscript 'A' in Y and superscript 'A' in A and ψ denote the right forward accelerometer 'A'. The subscripts 'SB', 'AB', 'ST' and 'AT' denote the first symmetric bending, anti-symmetric bending, symmetric torsion and anti-symmetric torsion modes respectively. Using accelerometer 'A' as the reference, the amplitudes of the various modes at 'C' are the same as those at 'A'. The symmetric modes are in phase but the anti-symmetric modes are 180 degrees out of phase. At location 'B', the amplitudes for the bending modes may not necessarily be the same as those at 'A', but the phase angles are in phase. For the torsion modes, not only are the amplitudes in general different at 'A' and 'B', but the phase angles differ by 180 degrees. Making use of these conditions, the four accelerometer signals from the front and rear of the tip tanks can be combined to give the following:

$$F_1 = Y_A - Y_C + \frac{A^A_{AT}}{A^B_{AT}}(Y_B - Y_D)$$

$$= 2\left(A^A_{AB} + A^B_{AB}\frac{A^A_{AT}}{A^B_{AT}}\right)e^{-\alpha_{AB}t}\sin(\omega_{AB}t + \psi^A_{AB}) \tag{3}$$

Knowing the amplitude ratio A^A_{AT}/A^B_{AT}, the anti-symmetric bending mode can be separated as shown in the above equation. Similar expressions can be obtained for the anti-symmetric torsion, symmetric bending and symmetric torsion modes and they are represented by the functions F_2, F_3 and F_4 respectively in Reference 4. The modal frequency and damping for the individual modes can be obtained by forming the power spectral density curves for these F functions and locating the central frequency and half power points on these spectra. As shown in Figure 10b, the damping is given as

$$g = \frac{\Delta f}{f_{max}} \tag{4}$$

3.2 Damping from Exponentially Decaying Input

For input excitation to the aircraft of the form of an exponential decaying cosine function, that is, $I \sim e^{-\alpha' t}\cos\omega_o t$, where I, α' and ω_o are the applied force, decay coefficient and circular frequency respectively, the power spectrum of I can be written as (Ref. 5).

$$S_I(\omega) = S_o\left\{\frac{1}{1+\beta^2(\omega-\omega_o)^2} + \frac{1}{1+\beta^2(\omega+\omega_o)^2}\right\} \tag{5}$$

where S_o is a constant and $\beta = 1/\alpha'$. Referring to Figure 12, let

$$\eta = \frac{S_I(\omega_o)}{S_I(O)} \tag{6}$$

then β can be solved in terms of η and ω_o by the following equation:

$$\beta = \frac{1}{2\omega_o}\left\{(4\eta - 2) + \sqrt{16\eta^2 - 16\eta + 1}\right\}^{1/2} \tag{7}$$

for $\eta > 0.9333$. From Figure 13 which shows the response to an exponential decaying cosine input, the damping ratio based on $S_Y(\omega_{max})$ and $S_Y(\omega_1)$ can be expressed as

$$g^2 = \frac{[(1-\Omega^2)^2 + \Psi_1]\theta_1 - (1-\Omega^2)^2\bar{S}_1}{\Omega^2\bar{S}_1 - (\Omega^2 + \delta_1)\theta_1} \tag{8}$$

A similar expression can be obtained using $S_Y(\omega_{max})$ and $S_Y(\omega_2)$, with all subscripts changed to '2'. To determine ω_n, the following expression is used:

$$\omega_n = \left\{\frac{-E + \sqrt{E^2 - 4DF}}{2D}\right\}^{1/2} \tag{9}$$

The terms given in Equations (8) and (9) are functions of ω_n, ω_{max}, ω_1, ω_2, ω_o, β, $S_Y(\omega_{max})$, $S_Y(\omega_1)$ and $S_Y(\omega_2)$. The expressions are rather lengthy and they are given in Reference 4.

3.3 Random Input and Noise

In Equation (1), the effect of noise in the measuring equipment is given by the term $n_A(t)$. In forming the F functions such as Equation (3), the noise can be included by simply adding a term $n_1(t)$, $n_2(t)$ etc. to the expressions for F. Since the response of the aircraft has no correlation with equipment noise, the effect of $n_1(t)$ etc. on the response spectra can be accounted for by the addition by terms $S_{n_1}(\omega)$, $S_{n_2}(\omega)$ etc. These noise spectra are usually small and neglected in analyzing the flight test data.

In the presence of turbulence or wing buffeting, the exciting force has a random component as represented by $p_A(t)$ in Equation (1). The mode separation procedure using expressions like Equation (3) can still be used for the deterministic part of the response signal. Spectra of F_1, F_2 etc. will show not only the modes as given by these equations, but also other modes which are excited by the random force. Treating the power spectrum of this force to be that for a white noise, the effect of a random component in the input excitation on the determination of the damping of a single mode of vibration system can be accounted for by taking the excitation power spectral density to be the sum of a deterministic and a random power spectral density since it is assumed that the two components are uncorrelated. If S_w is the power spectral density of a white noise random force, then Equations (8) and (9) can still be used to determine damping and resonant frequency provided that the ratio S_w/S_o be included in the terms θ_1, θ_2 and D as given in Reference 4.

If two of the modes are close together, it will not be possible to separate them and give satisfactory results if the turbulence level or the buffet intensity is high. In Figure 14 suppose the random load that generates the 'β' mode has a white noise power spectral density S_w. To find the true damping and resonant frequency for the 'α' mode from the combined power spectral density plot, the following equations can be used based on measurements from the LHS of the power spectral density curve:

$$g_\alpha = \left\{ \frac{-B_1 - \sqrt{B_1^2 - 4A_1C_1}}{2A_1} \right\}^{1/2} \tag{10}$$

and

$$G_1\omega_{n_\alpha}^8 + G_2\omega_{n_\alpha}^6 + G_3\omega_{n_\alpha}^4 + G_4\omega_{n_\alpha}^2 + G_5 = 0 \tag{11}$$

Using measurements from the RHS of the combined power spectral density curve, a similar expression as Equation (10) can be obtained for the damping except that terms A_1, B_1 and C_1 be replaced by A_2, B_2 and C_2. These terms together with those appearing in Equation (11) are functions of ω_{max}, ω_o, ω_{n_α}, ω_{n_β}, ω_1, ω_2, $S_Y(\omega_{max})$, $S_Y(\omega_1)$, $S_Y(\omega_2)$, S_w and g_β. Reference 4 gives the expressions for these terms.

3.4 Interactive Computer Program Description

When the computer program is first called, the accelerometer signals Y_A, Y_B, Y_C and Y_D together with the aileron or elevator position are displaced on the screen of a graphics terminal. On examining these signals, the user chooses the beginning and end of the samples to be analyzed. The experimental data is sampled at a fixed frequency, but the program can change the sampling frequency to a lower value if desired. Also, the sample length can be increased by padding the data block with zeros. The user then has the option of applying a window to the data. If a rectangular window is chosen, the range of data where the window applies is inputted from the terminal. For an exponential window, the data is being multiplied by the exponential function $e^{-\gamma t}$, and the program requires an input value for the damping γ.

The next step involves computing the functions $Y_A \pm Y_C$ and $Y_B \pm Y_D$ and displaying the power spectral density plots of of these functions. From these plots, the movement of a joystick will determine the ratios of A^A_{AT}/A^B_{AT} etc. in the expressions for the F functions. If the value of a particular A cannot be determined, an arbitrary value can be entered with the joystick. Also, values of A can be chosen at 'A' and 'B' so as to prescribe values for the amplitude ratios to be used as first estimates in evaluating the F functions. These will generate a guide for the operator to choose the next set of amplitude values which will improve on the mode separation. The decision that good mode separation is achieved is made by the operator from observation of the power spectral density curves. The user then chooses the mode to be analyzed by specifying the F function.

From the selected power spectral density plot, the user is prompted by the computer to specify a frequency window in the vicinity of ω_{max} which is the frequency at which the power spectral density is a maximum. This is achieved by the movement of the joystick. An enlarged display of the spectrum is then shown on the terminal screen. The operator has the option of obtaining ω_{max} and the frequencies at the half power points from an automatic computer search. This procedure is used if the spectrum is relatively noise free. The second option is to fit a smooth curve and locate ω_{max} using the joystick. The computer then determines the half power points and proceeds to calculate the damping ratio.

The determination of damping can be carried out by two methods. The user can choose the first option which treats the aerodynamic forces generated by a stick rap to be an impulse function. The damping can readily be determined from the location of the peak of the power spectral density curve and the half power points. The second option treats the behaviour of the aerodynamic forces as that of an exponential decaying cosine function. The user is then requested by the computer to input the values of η and ω_o, and then proceeds to evaluate β from Equation (7). Setting $\bar{S}_1 = 2$ and using ω_1 and $\Delta\omega_1$, g is determined from Equation (8).

Using ω_2 and $\Delta\omega_2$ corresponding to $\bar{S}_2 = 2$, another value of g can be obtained. The damping is obtained from the average of these two values. Equation (9) is then evaluated for ω_n which is used in Equation (8) to give an improved value of g. An iterative procedure is set up and a solution is obtained when g is within 1% in two consecutive iterations. On completion of damping analysis for the modes of interest, final plots for the F functions and their corresponding spectra are displayed at the option of the user.

In the interactive computer program the analysis of Section 3.3 for random input and noise has not been implemented yet. A separate program for investigating the effect of turbulence and wing buffeting has been developed and it can be interfaced with the interactive program rather easily. The effect of measuring equipment noise has not been considered since it is usually small and can be neglected. However, implementing this into the computer program is rather straightforward. Using the values of ω_{max}, ω_1 and ω_2 for $\bar{S}_1 = \bar{S}_2 = 2$, Equations (8) and (9) can be used to investigate the effect of the presence of a random input component of the form given in Equation (1) on the damping of a single mode vibrating system. For two closely spaced modes denoted as the 'α' and 'β' modes, the procedure is to use the interactive program to give an estimate for the resonant frequencies and damping ratios for these two modes by treating them to be non-interfering. For known white noise input, Equation (10) can be used to calculate an average value of g_α based on ω_{max}, ω_1 and ω_2 for the 'α' mode. ω_{n_α} is then determined from Equation (11). An iterative procedure is required to solve these two equations until g_α in two consecutive iterations is within the specified tolerance. Using the values of g_α and ω_{n_α}, the same equations can be used to calculate 'β' mode. The calculations are repeated until g_α and g_β converge to within the desired tolerance, which is 1% in this program.

4.0 COMPUTATIONAL METHOD FOR FLUTTER CLEARANCE

A computer code has been developed to analyze flutter characteristics of aircraft carrying under-wing stores. To calculate the vibration modes, the aircraft is separated into its main structural 'branches', i.e. port wing, starboard wing, front fuselage, etc The cantilever modes of these primary structural branches are determined first to obtain the so-called branch modes. The complete aircraft normal modes are subsequently evaluated in terms of these branch mode degrees of freedom and aircraft rigid body motion. By this means a good physical description of the aircraft modes is obtained with a minimum number of degrees of freedom. Aerodynamic generalized forces are computed using either aerodynamic derivative data or aerodynamic influence coefficients. The flutter equation for selected equivalent airspeeds and Mach numbers is set up as an eigenvalue problem and is solved for modal frequencies and dampings by the British 'p' method.

Figure 15 shows a flow diagram of the analysis procedure. Flutter solutions are obtained by using a sequence of three computer programs. The first of these computes the branch modes, the second computes aircraft normal modes and flutter coefficients and the third computes flutter solutions. A brief description of the individual computer modules is given in the following sections. More details on the computer code can be found in Reference 6.

4.1 Branch Modes Analysis

The method for deriving natural modes and frequencies of non-uniform beams uses the Holzer-Myklestad approach. The method is currently restricted to beams having straight flexural axes and bending in only one plane. Figure 16 shows the beam axis system. The whole aircraft is related to orthogonal axes having their origin on the fuselage centerline at the station vertically above or below the wing elastic axis. Positive directions are x forward, y starboard and z downward. Rotations about these axes are ϕ, θ and ψ. The elastic properties of the beam are concentrated in an idealized weightless beam lying along the flexural axis. The beam's mass is represented by a series of points, having both mass and rotary inertia, whose centres of gravity do not necessarily lie on the flexural axis. These points are connected to the idealized beam at the series of stations known as datum points. The bending and torsional flexibilities (1/EI and 1/GJ) of the idealized beam vary linearly with distance along the beam between adjacent datum points.

Pylons perpendicular to the flexural axis may be attached at any datum point. Pylons are assumed to be below the main beam and have principal elastic axes aligned with those of the main beam (Fig. 17). Pylon stores are represented by rigid bodies possessing mass, inertias and cross inertias about all axes and offsets in three directions. The pylon is permitted to bend both in and across its plane and to twist about its (vertical) axis. The pylon flexibilities are assumed constant over the depth of the pylon.

The beam and pylon damping being assumed zero, and the stiffness linear, this model can execute harmonic motion in a finite number of modes.

The idealized model is considered at an instant of maximum deflection in an oscillation at some chosen frequency ω. The displacements and forces acting at a section of the beam are represented by the vector q. Due to the in-plane rigidity of the model the only significant elements of the vector for the beam are:

q = Z bending deflection
ϕ bending slope
θ rotation
V lateral shear force
M bending moment
T torsion

A similar q vector with six degrees of freedom and six forces describes the pylon store.

The essence of the Holzer-Myklestad approach is to relate the vector q_{n+1} at datum point n+1 to the vector q_n. A matrix equation can be generated which relates the forces, moments and displacements (six in all) at the beam root to the forces, moments and displacements at the tip. When boundary conditions are imposed, a determinant can be evaluated whose zeros occur at the natural frequencies of the beam. The method is programmed to locate the zeros within a specified frequency range and to evaluate the associated beam deflection modes.

For the CF-5 aircraft, front and rear fuselage cantilever branch modes have been computed for the full fuselage fuel configuration. The empty fuselage configuration is assumed to have the same cantilever mode shapes as the full fuel case. To obtain branch modes, the forward fuselage is divided into 13 stiffness segments, 5 of which have associated mass. The aft fuselage is represented by 6 segments, 4 with mass. The fuselage stiffness and mass data is given in Reference 7. Half-wing cantilever branch modes are evaluated for each different wing store configuration. The wing is modelled by 19 stiffness segments, 7 of which have associated mass. The stiffness and mass values used are also given in Reference 7.

4.2 Calculation of Aircraft Modes and Flutter Coefficients

4.2.1 Aircraft Modes

The method for deriving aircraft modes takes as starting point the availability of normal branch modes for aircraft components such as wing, front fuselage, rear fuselage. Once these normal branch modes are obtained, the derivation of the complete aircraft modes is routine from the initial weight, stiffness and geometry data through to the required aircraft modes. The method is applicable to all conventional aircraft structures where such components as wings, fin, stabilizer and fuselage can be idealized as beams. Sweepback, dihedral and differences in vertical level between wings, fuselage and stabilizer can be taken into account.

The basic premise is that the deformed shape of the aircraft (in the modes of interest) can be adequately represented by a summation over the original branch modes and including certain "rigid-body" motions of the whole aircraft. Limited experience indicates that, if the first k aircraft modes are required, it is necessary to use a total of at least 2k branch modes and rigid body modes. To obtain good accuracy the use of 3k modes is recommended.

For most aircraft components the mode of deformation involves flexible motion in only 3 of the freedoms, any motion in the other 3 freedoms being effectively rigid body motion. For example, wing bending and torsion affect only the heave, roll and pitch (z, ϕ, θ) of any bay on the wing. For the forward, sideslip and yawing motions (x, y, ψ) the whole wing may be represented by a rigid body. For the aircraft fuselage, the number of degrees of freedom is restricted to 3 (or ever 2) by considering separately the symmetric and antisymmetric aircraft modes.

Having formed the generalized inertia matrix [a], the corresponding generalized stiffness matrix [e] is derived by multiplying the diagonal elements of [a] by the corresponding values of ω^2, where ω is the branch mode frequency. The equation of motion (with zero damping or excitation) can be written as:

$$[a] \cdot \ddot{q} + [e] \cdot q = 0 \tag{12}$$

where q, an n × 1 matrix, represents the amplitude in each of the n modes. For motion in a normal mode of vibration i this becomes

$$[e] \cdot q_i = [a] \cdot \omega_i^2 \cdot q_i \tag{13}$$

where ω_i is the circular frequency in the normal mode. The problem thus reduces to the determination of the eigenvalues (latent roots) and vectors of Equation (13).

Now, in general, where rigid body motions of the whole aircraft have been included in the n modes chosen, there will be a corresponding number of zero roots to the above equation. The elimination of these roots facilitates computation of those remaining.

Equation (13) can be partitioned into the rigid body and elastic modes (denoted by o and e subscripts, respectively). Thus

$$\left[\begin{array}{c|c} e_{oo} & e_{oe} \\ \hline e_{eo} & e_{ee} \end{array}\right] \left[\begin{array}{c} q_o \\ \hline q_e \end{array}\right] = \omega_i^2 \left[\begin{array}{c|c} a_{oo} & a_{oe} \\ \hline a_{eo} & a_{ee} \end{array}\right] \left[\begin{array}{c} q_o \\ \hline q_e \end{array}\right] \tag{14}$$

The stiffness associated with the rigid body modes is zero, i.e. $[e_{oo}] = [e_{eo}] = [e_{oe}] = 0$. Equation (14) can be simplified to the following:

$$q^* = \omega^2 \left(\sqrt{e_{ee}}^{-1} [\tilde{a}] \sqrt{e_{ee}}^{-1}\right) q^* \tag{15}$$

where

$$q^* = \sqrt{e_{ee}}\, q_e \tag{16}$$

and

$$[\tilde{a}] = [a_{ee}] - [a_{eo}] [a_{oo}]^{-1} [a_{oe}] \tag{17}$$

Equation (15) gives the latent roots $(1/\omega^2)$ and vectors (q*). The complete q matrix can be obtained from its partitioned components q_o and q_e.

4.2.2 Flutter Coefficients from Strip Derivatives

The lifting surface under consideration is divided into strips of width ΔS as shown in Figure 18. For two degrees of freedom in heave and pitch, the lift and moment for a strip of the wing surface oscillating at a frequency ω can be written as:

$$\Delta L = \rho V^2 c \Delta S \left[(\ell_z + i\upsilon \ell_{\dot{z}}) \cdot \frac{z}{c} + (\ell_\alpha + i\upsilon \ell_{\dot{\alpha}}) \cdot \alpha \right] \tag{18}$$

$$\Delta M = \rho V^2 c^2 \Delta S \left[(m_z + i\upsilon m_{\dot{z}}) \cdot \frac{z}{c} + (m_\alpha + i\upsilon m_{\dot{\alpha}}) \cdot \alpha \right] \tag{19}$$

where $\upsilon = \omega c/V$, V being the aircraft velocity and c is the average chord of the strip; ℓ_z, ℓ_α, m_z, m_α, $\ell_{\dot{z}}$, $\ell_{\dot{\alpha}}$, m_z and $m_{\dot{\alpha}}$ are the local aerodynamic strip derivatives and their values for the CF-5 'clean wing' aircraft are given in Reference 7. Using Equations (18) and (19), the generalized aerodynamic force can be obtained in terms of the strip derivatives as

$$Q_{rn} = -\rho V^2 (C + i\upsilon_m B) \cdot q_n \tag{20}$$

where

$$B = \sum_{\text{span}} [z_r \mid C \cdot \alpha_r] \left[\begin{array}{c|c} \ell_{\dot{z}} & \ell_{\dot{\alpha}} \\ \hline (-m_{\dot{z}}) & (-m_{\dot{\alpha}}) \end{array} \right] \cdot \left[\begin{array}{c} z_n \\ \hline C \cdot \alpha_n \end{array} \right] \frac{C}{C_m} S \tag{21}$$

$$C = \sum_{\text{span}} [z_r \mid C \cdot \alpha_r] \left[\begin{array}{c|c} \ell_z & \ell_\alpha \\ \hline (-m_z) & (-m_\alpha) \end{array} \right] \cdot \left[\begin{array}{c} z_n \\ \hline C \cdot \alpha_n \end{array} \right] \Delta S \tag{22}$$

Q_{rn} is the generalized aerodynamic force in the r^{th} mode due to a displacement q_n in the nth mode, and υ_m is a mean frequency parameter $\upsilon_m = \upsilon C_m/C$.

The generalized matrix equation which is solved to obtain flutter roots, frequencies and speeds is

$$(A + \sigma \hat{A})\ddot{q} + (B\sqrt{\sigma} V_E + D)\dot{q} + (CV_E^2 + E)q = 0 \tag{23}$$

where $\sigma = \rho/\rho_o$, ρ_o being the air density at sea level and V_E is the ratio of the equivalent airpseed to a reference airspeed (usually taken as 1000 ft/sec). A is the structural mass inertia matrix, $\hat{A}$ the aerodynamic inertia matrix, B the aerodynamic damping matrix given by Equation (21), C the aerodynamic stiffness matrix given by Equation (22), D the structural damping matrix and E the structural stiffness matrix.

4.2.3 Flutter Coefficients from Aerodynamic Influence Coefficients

The strip aerodynamics method described above for flutter calculations uses derivatives available for the 'clean wing' case. To include the effects of stores, a more complete aerodynamic model is required to give better results. The doublet-lattice computer code H7WC (Ref. 8) has been modified to produce aerodynamic influence coefficients (AIC's) for wing/store configurations (Ref. 9) in calculating flutter coefficients.

The evaluation of the aerodynamic coefficients for the flutter equation from aerodynamic influence coefficient (AIC) data can be determined from the generalized aerodynamic forces. It is assumed that the AIC matrix is such as to give the lift and moment at selected points resulting from unit heave and pitch accelerations of those points. For such an AIC matrix [F], a typical term in the generalized aerodynamic force matrix is

$$\begin{aligned} Q_{ij} &= 2 \cdot \sigma \cdot \{g_i\}^T \cdot [F] \cdot \{g_j\} \cdot \ddot{q}_j \\ &= 2 \cdot \sigma \cdot \omega^2 \cdot \{g_i\}^T \cdot [F] \cdot \{g_j\} \cdot q_j \end{aligned} \tag{24}$$

where $\{g_i\}$ and $\{g_j\}$ are vectors of heave and pitch displacements in the i^{th} and j^{th} modes. [F] is a function of Mach number and reduced frequency K defined by

$$K = \frac{\omega C_R}{2V} \tag{25}$$

and C_R is the AIC reference chord. Using Equations (20) and (24), the aerodynamic damping and stiffness matrices can be obtained. Sensitivity of these matrices to the K value for which the AIC matrix has been derived can be reduced if the AIC matrix has been evaluated for two fairly well separated values of K, by including the effect of an aerodynamic inertia coefficient. The expression for generalized aerodynamic force, becomes

$$Q_{ij} = -\rho V^2 \cdot \left(C_{ij} + \frac{i\omega C_m}{V} \cdot B_{ij} - \frac{\omega^2 C_m{}^2}{V^2} \cdot A_{ij} \right) \tag{26}$$

If $[F]_{REAL}$ is expressed as a parabolic function 1/K

$$[F]_{REAL} = \frac{1}{K^2} [F_C] + [F_A] \tag{27}$$

then

$$\hat{A}_{ij} = \frac{2}{\rho_o C_m{}^2} \cdot \left[\{g_i\}^T \cdot [F_A] \cdot \{g_j\} \right] \tag{28}$$

and

$$C_{ij} = \frac{-8}{\rho_o C_R{}^2} \cdot \left[\{g_i\}^T \cdot [F_C] \cdot \{g_j\} \right] \tag{29}$$

$[F]_{IMAG}$ can be written as a linear function of 1/K as

$$[F]_{IMAG} = \frac{1}{K} \cdot [F_B] \tag{30}$$

and B_{ij} is then given by the expression

$$B_{ij} = -\frac{4}{\rho_o C_R C_M} \left[\{g_i\}^T \cdot [F_B] \cdot \{g_j\} \right] \tag{31}$$

a form compatible with expressions (26) and (27).

Values for $[F_A]$ and $[F_C]$ in Equation (27) are obtained from the following expressions

$$[F_A] = \frac{[F_{K_2}]_{REAL} \cdot K_2^2 - [F_{K_1}]_{REAL} \cdot K_1^2}{\left(K_2^2 - K_1^2 \right)} \tag{32}$$

$$[F_C] = K_1^2 \cdot \left\{ [F_{K_1}]_{REAL} - [F_A] \right\} \tag{33}$$

where $[F_{K_1}]$, $[F_{K_2}]$ are the AIC matrix at K_1 and K_2 respectively.

4.3 Flutter Solutions

Flutter solutions are obtained from Equation (23). The basic input to the program are the generalized structural mass matrix, generalized aerodynamic damping matrix, generalized aerodynamic stiffness matrix, and generalized stiffness matrix. The aerodynamic inertia and structural damping matrices can also be read into the program, but they are usually omitted in the calculations. Define

$$\begin{aligned} X &= A + \sigma \hat{A} \\ Y &= B \sqrt{\sigma} V_E + D \\ Z &= C V_E^2 + E \end{aligned} \tag{34}$$

Equation (23) can be written as

$$X\ddot{q} + Y\dot{q} + Zq = 0 \tag{35}$$

which is an eigenvalue problem of the form

$$\lambda \begin{pmatrix} q \\ --- \\ \dot{q} \end{pmatrix} = [T] \begin{pmatrix} q \\ --- \\ \dot{q} \end{pmatrix} \tag{36}$$

where

$$[T] = \begin{bmatrix} 0 & I \\ -X^{-1}Z & -X^{-1}Y \end{bmatrix} \tag{37}$$

The eigenvalues λ are extracted from the T matrix using the Upper Hessenberg method.

5.0 SOME RESULTS FROM LAU-5003/A ROCKET LAUNCHERS

For illustration purposes, some results for the LAU-5003/A rocket launchers are given in this section. The configuration corresponds to that for Mission 1 in the Cold Lake Flutter trials: two LAU-5003/A rocket launchers carrying nineteen C14 rockets with Mk 1 warheads at the outboard pylon and eleven C14 rockets with Mk 1 warheads at the inboard pylon. All launchers were equipped with nosecones.

Figure 19 shows the geometry of the aerodynamic configuration used in the doublet-lattice method. The tip tanks and launchers are represented by slender bodies with conical noses, cylindrical central bodies and truncated cones at the ends. The wing root is considered to end at a plane of symmetry at y/S = 0.2. The steady state spanwise load and moment distributions at Mach number M = 0.8 are shown in Figure 20. The computation is obtained by giving the model a rigid body, nose-up pitch and setting the frequency parameter to zero. All moments are taken about the local leading edge, and in the tip tank region, the moment is about the wing leading edge extended outboard. The unsteady load and moment distributions for unit heave and pitch oscillation about mid-chord of the wing root are given in Figures 21 and 22 for M = 0.8 and reduced frequency K = 0.2.

In Figure 23, the node lines for the symmetric and anti-symmetric bending and torsion modes are shown for the full tip tanks case. It is seen that the node line for the anti-symmetric bending mode runs across the aileron and some difficulties had been encountered in flight tests where insufficient response of this mode was detected when stick pulses were used to excite the aircraft.

The interactive computer program has been used primarily to perform post-flight data analysis for flutter trials. Figure 24 shows a typical display of the accelerometer signals at the four positions Y_A, Y_B, Y_C and Y_D indicated in Figure 5. Also shown on top of this figure is the aileron position. In this particular case, the aircraft tip tanks were full, and a lateral stick pulse was initiated by the pilot to excite the anti-symmetric modes. The aircraft speed was 437 KEAS at an altitude of 7382 ft above sea level. Approximately 2400 points per channel of data were transmitted by telemetry to the ground station and recorded on tapes. Since only the first few seconds of the accelerometer signals after the stick rap are of interest, it is desirable to suppress the noise by applying an exponential window to the data. This is simply done by inputting into the graphics terminal the beginning and end of the range of data points for analysis and the damping for the exponential window. Figure 25 shows the edited data.

In Figure 26 the function F_2 for the anti-symmetric torsion mode and its power spectral density plots are shown. The bottom curve is an enlarged plot of the power spectral density. The curve with the open circles is a curve fit of the original data, and the user of the computer program is given the option of choosing the number of points. The peak of the power spectral density curve is determined by the movement of the joystick of the graphics terminal to the point selected by the operator. The horizontal and vertical lines show the half power points and the frequency correcponding to the maximum peak respectively. By moving the joystick to the two half power points, the values of ω_1, $\Delta\omega_1$, ω_2, and $\Delta\omega_2$ are inputted automatically to the program for calculating the damping.

To determine the spectra of the aerodynamic forces generated by stick raps, a panel method as described in Reference 10 may be used. However, this method may not be suitable in the flutter flight trials described here since the technique requires the fluctuating pressures on a large number of locations on the wing surfaces to be measured. An approximate estimate can be obtained by assuming the forces to be proportional to the control surface displacements generated by a stick rap. Also, the force spectrum is assumed to be similar to the displacement spectrum. Figure 27 shows typical time histories of the aileron and elevator pulses together with their spectra. It can be seen that treating the stick rap as an impulse function is only a rough approximation. The aileron pulse damps out much faster than the elevator pulse. The experimental power spectral density plots are obtained after passing the signals through a high pass filter. Also shown in the figure are the curves obtained from Equation (5) using experimentally measured values of η and frequencies ω_o or f_o. Figure 28 shows that the frequency f_o for the aileron and elevator pulses can be treated to be approximately constant with aircraft speed and independent on whether the tip tanks are empty or full. The values of η are also nearly the same within the range of airspeeds considered except for the elevator pulse at airspeeds below 470 KEAS.

Damping and frequencies for symmetric and anti-symmetric modes are shown in Figures 29 to 32 for full and empty tip tanks. Theoretical predictions using the doublet-lattice and strip derivatives methods are compared and it is seen that the bending frequencies are almost identical in all the cases while the strip derivatives method gives larger values for the torsion frequencies. In the calculations, no structural damping has been included.

The analytical damping values between the two methods are reasonably good for the symmetric modes while large differences are detected for the anti-symmetric modes. Also shown in the figures are the on-line flight test and post-flight data. In post-flight analysis, the damping values are calculated from Equation (8) using ω_n determined from Equation (9). Values of ω_o and η

needed in these equations are determined from either the aileron or elevator pulse. The frequencies obtained from on-line flight analysis and post-flight analysis are very close. When compared to theory, the symmetric bending modes agree very well, and reasonable agreement is obtained for the other cases.

The experimental damping values from the two methods show the largest discrepancies in the anti-symmetric torsion mode. This may be due to the different windows applied in the data reduction and to the different forms of the excitation power spectral density used in determining the damping values. Comparisons with calculations show that analytic computations give reasonable results and hence are useful in predicting flutter trends. Shown also in Figure 31 are results for the torsional damping taking into consideration interference from the adjacent bending mode. The value used for S'_w, which is a nondimensional quantity denoting the magnitude of the input white noise spectra, is taken to be 0.15. This is chosen arbitrarily in order to indicate the effect on the damping as no experiment has been performed to determine this quantity. Furthermore, the results given do not involve any iteration between the two modes as described in Section 3.3 The differences in damping are not very significant, but the value of S'_w used is considered small for actual conditions when wing buffeting occurs. Figure 32 also gives a comparison for damping values between a purely exponential decaying cosine input and one including a random input component with a value of S_w/S_o equals to 0.2. Again representative values of S_w/S_o in flight tests are not available and the value of 0.2 used is simply for illustration purposes It does, however, indicate that at high turbulence levels or buffet intensities, corrections should be applied in determining damping values.

6.0 CONCLUSIONS

An overview of the Canadian capability in flutter clearance on the CF-5 aircraft carrying underwing stores has been described. The Aerospace Engineering Test Establishment at Cold Lake offers excellent range facilities and on-line data reduction for flutter trial tests.

The use of stick raps to excite the modes of vibrations of an aircraft in flutter flight tests is simple and can be quite effective. There are, however, some store configurations for the CF-5 aircraft which give insufficient response of the anti-symmetric bending mode. This is due to the fact that the node line for this mode runs across the aileron so that aileron forces do not produce sufficiently large acceleration in this mode for analysis purposes.

The computer program for post-flight flutter analysis developed for the Canadian Forces operates in the interactive mode. It can also be used to supplement on-line analogue monitoring of subcritical damping in flutter tests. The ability of the program to display the power spectral density in any desired frequency range makes it quite useful to analyze weakly excited modes. Treating the stick rap to be an impulse function can only be taken as a rough approximation. The damping results obtained by assuming the spectra of the forces generated by stick raps to have the same form as that for an impulse function may be quite different from those where the forces are considered to be represented by an exponential decaying cosine function. The differences are generally larger for the symmetric modes since the elevator pulses usually oscillate a few cycles before decaying to zero in about 1 second.

For the LAU-5003/A trials, the frequencies obtained from on-line flight analysis and post-flight analysis are very close. The damping values show the largest discrepancies in the anti-symmetric torsion mode. This may be due to the different windows applied in the data reduction and to the different forms of the excitation power spectral density used in the calculations.

Theoretical predictions using the doublet-lattice and strip derivative methods give almost identical bending frequencies, while the strip derivative method gives larger values for the torsion frequencies. Agreement in damping values between the two methods is reasonably good for the symmetric modes while large differences are detected for the anti-symmetric modes. Comparisons with experimental results show that the analytic flutter computational method gives reasonable results and is a useful tool in predicting flutter trends.

7.0 REFERENCES

1. Solnoky, P.; Leech, C. — *A Review of Foreign External Store Clearance Methodology and A Proposal for the Establishment of a Canadian Aircraft/Store Certification Program (U).* DREV TN 2033/72, Defence Research Establishment, Valcartier, Aug. 1972.

2. van Nunen, J.W.G.; Zwaan, R.J. — *Flight Flutter Tests on the CF-5A/B Aircraft Equipped with BL-755 and SUU-25C/A Stores.* NLR TR 78049 C, National Aerospace Laboratory, The Netherlands, 1978.

3. — *Air Standardization Coordinating Committee (ASCC) Test Report on Joint CF/USAF CF-5A Ground Vibration Test.* Accomplished at the Air Force Armament Laboratory, Eglin AFB, FL, 10 Sept. – 25 Oct. 1979.

4. Lee, B.H.K. — *An Interactive Computer Program for the Determination of Sub-critical Damping in Flutter Flight Tests.* 1982 Aircraft/Stores Compatibility Symposium, Naval Surface Weapons Center, White Oak, Maryland, 26-28 Oct. 1982.

5. Bendat, J.S.; Piersol, A.G. — *Random Data: Analysis and Measurement Procedures.* Wiley-Interscience, 1971.

6. Riedel, F. — *CF-5 Stores Flutter Model Computer Program Documentation. Vols. I-V.* Canadair Ltd. Rept. RAU-261-106, 1980.

7. Riedel, F. — *Clearance of LAU-5003/A Configurations on the CF-5. Final Flutter Analysis Results.* Canadair Ltd., RAU-261-105, 1980.

8. Giesing, J.P.; Kalman, T.P.; Rodden, W.P. — *Subsonic Unsteady Aerodynamics for General Configurations.* Part I, Vol. I -- Direct Application of the Nonplanar Doublet-Lattice Method. Part I, Vol. II - Computer Program H7WC. Part I, Vols. I and II - AFFDL-TR-71-5 Air Force Flight Dynamics Laboratory, Wright Patterson Air Force Base, Ohio, November 1971.

9. Riedel, F. — *Incorporation of the Doublet-Lattice Method in Stores Clearance Flutter Analysis.* Canadair Ltd., RAU-261-111, 1982.

10. Lee, B.H.K. — *A Method for the Predication of Wing Response to Non-Stationary Buffet Loads.* National Research Council, Canada LR-601, 1980.

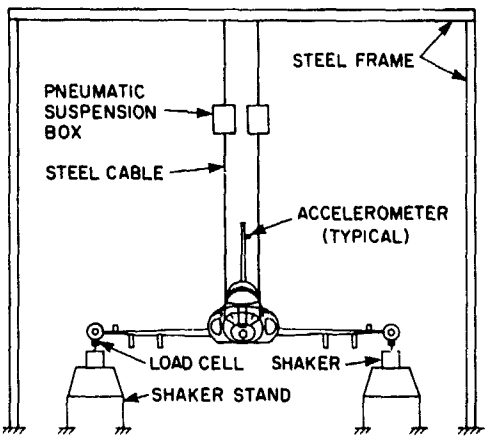

FIG. 1: SCHEMATIC OF THE GVT SET UP

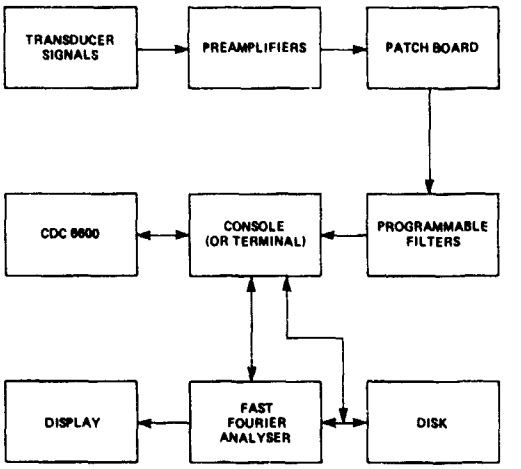

FIG. 2: BLOCK DIAGRAM OF DATA ACQUISITION AND DATA ANALYSIS SYSTEM

FIG. 3: CF-5 AIRCRAFT FITTED WITH CENTERLINE TANK AND CARRYING LAU-5003/A STORES

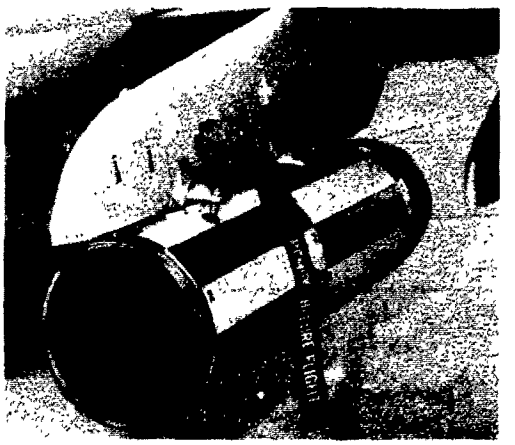

FIG. 4: LAU-5003/A ROCKET LAUNCHER

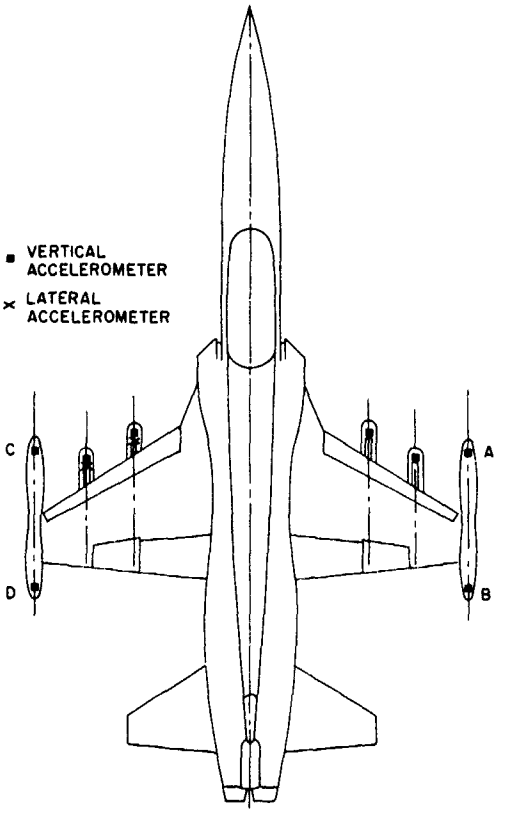

FIG. 5: LOCATION OF ACCELEROMETERS ON THE CF-5 AIRCRAFT

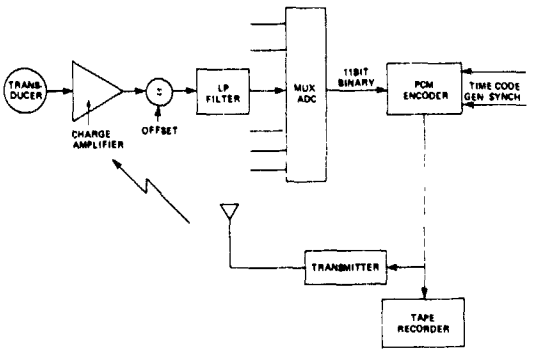

FIG. 6: AIRBORNE DATA SYSTEM

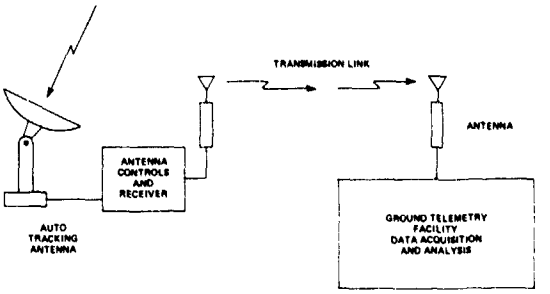

FIG. 7: DATA CHAIN AT AETE

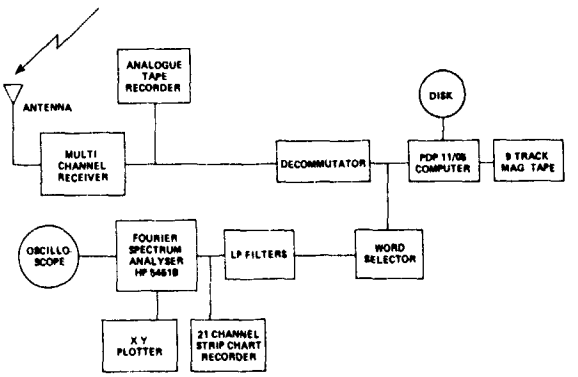

FIG. 8: GROUND TELEMETRY AND DATA SYSTEM

COMMUNICATION FREQUENCY 358.2 MHz
RATCON TO MONITOR TEST AIRCRAFT

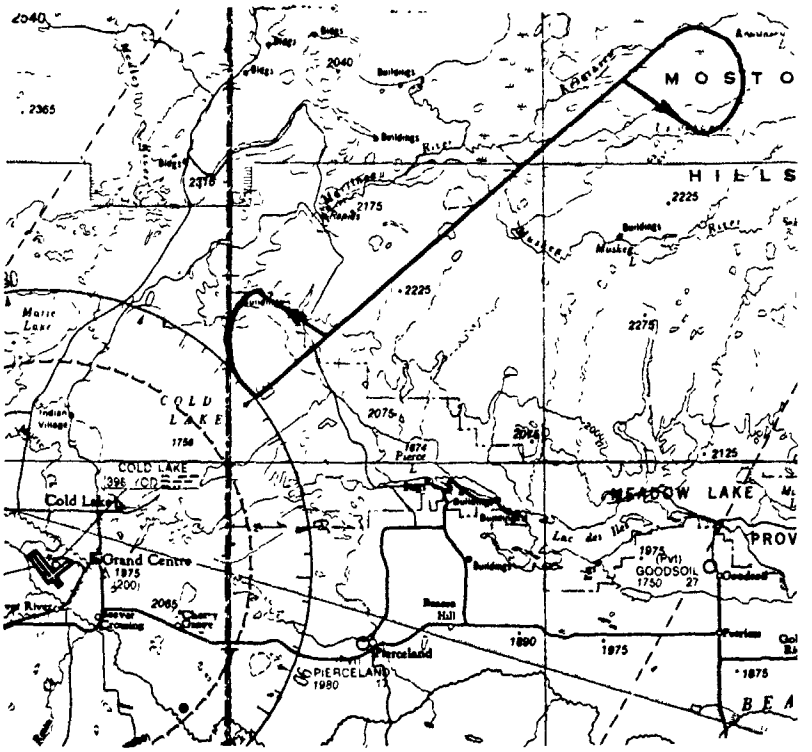

FIG. 9: FLIGHT TEST PATTERN

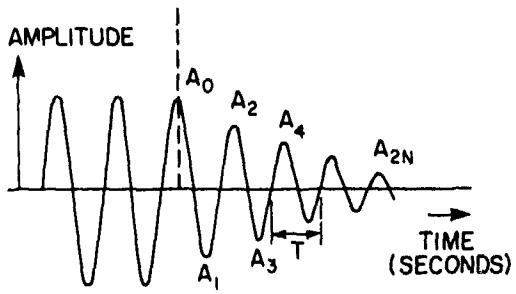

RESONANCE FREQUENCY: $f = \frac{1}{T}$ (Hz)

DAMPING: $g = \frac{1}{\pi N} \ln \frac{A_0}{A_{2N}}$

where N = NUMBER OF CYCLES

FIG. 10a: PROCEDURE TO DETERMINE FREQUENCY AND DAMPING FROM A DECAYING SIGNAL

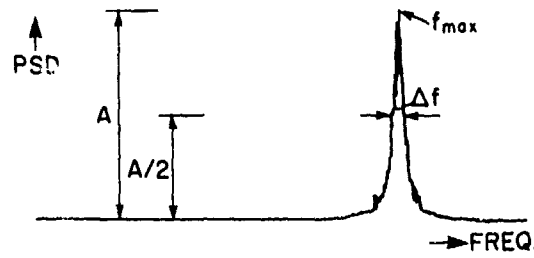

f_{max} ⇒ DETERMINED BY LOCATION OF MAXIMUM AMPLITUDE, A

$g = \frac{\Delta f}{f_{max}}$ ⇒ Δf DETERMINED AT HALF MAXIMUM AMPLITUDE, A/2

FIG. 10b: DETERMINATION OF RESONANCE FREQUENCY AND DAMPING FROM POWER SPECTRAL DENSITY (PSD)

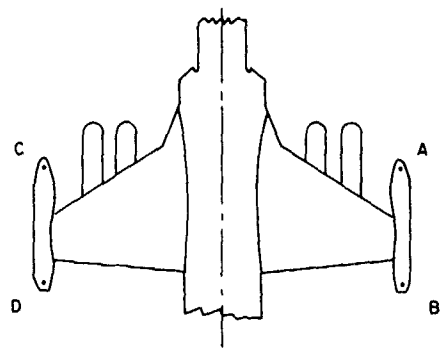

• VERTICAL SENSING ACCELEROMETERS

EMPHASIZED MODE	ACCELEROMETER SIGNAL SUMMATION
ANTISYMMETRIC WING BENDING	Σ ASIB = A + B - C - D
ANTISYMMETRIC WING TORSION	Σ ASIT = A - B - C + D
SYMMETRIC WING TORSION	Σ SIT = A - B + C - D
SYMMETRIC WING BENDING	Σ SIB = A + B + C + D

FIG. 11: ACCELEROMETER SIGNAL SUMMATIONS

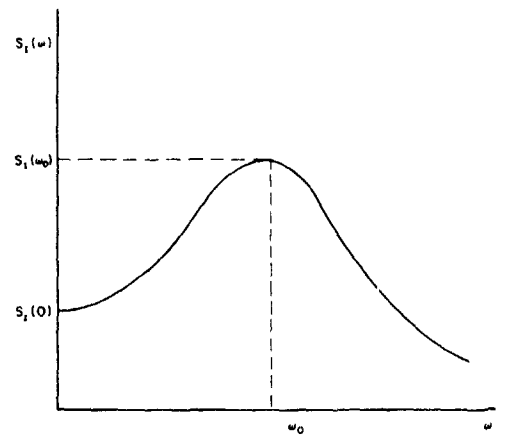

FIG. 12: POWER SPECTRAL DENSITY FOR EXPONENTIAL DECAYING COSINE INPUT

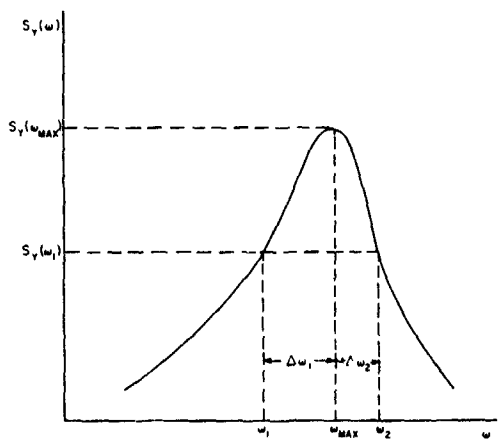

FIG. 13: RESPONSE SPECTRUM

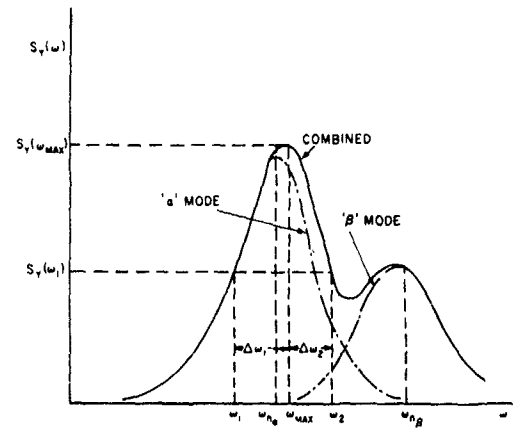

FIG. 14: RESPONSE SPECTRUM OF TWO CLOSELY SEPARATED MODES

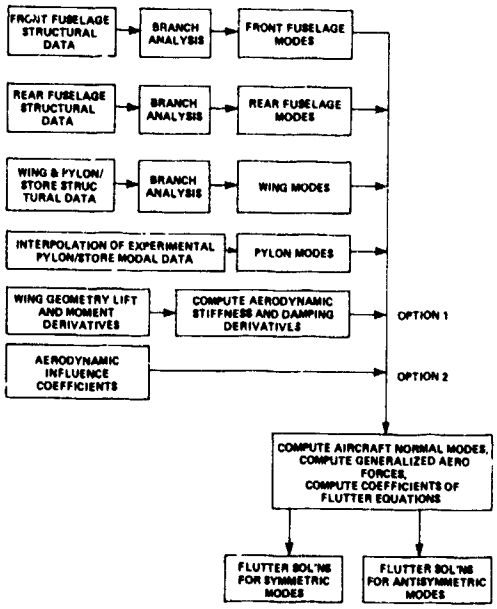

FIG. 15: ANALYSIS PROCEDURE

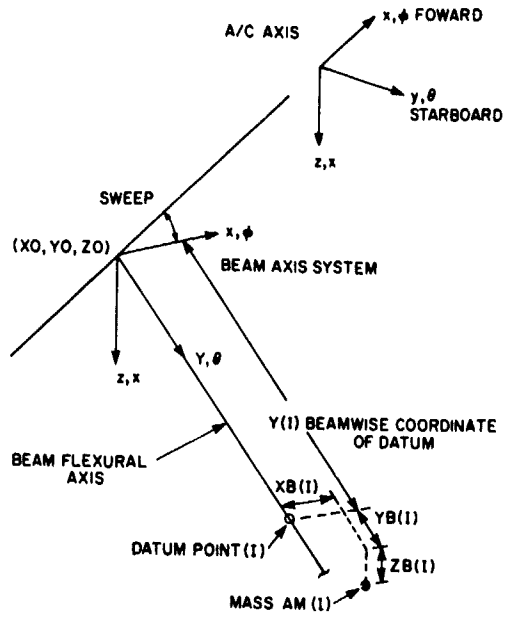

FIG. 16: BEAM AXIS SYSTEM

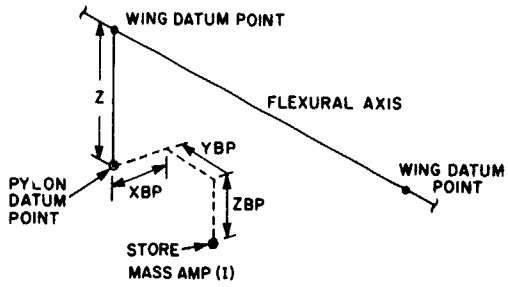

FIG. 17: PYLON DATUM POINT AND STORE OFFSETS

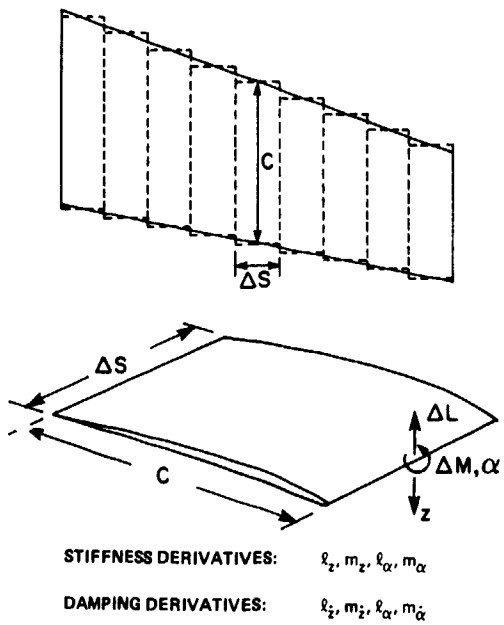

FIG. 18: EQUIVALENT CONSTANT STRIP AERODYNAMIC DERIVATIVES

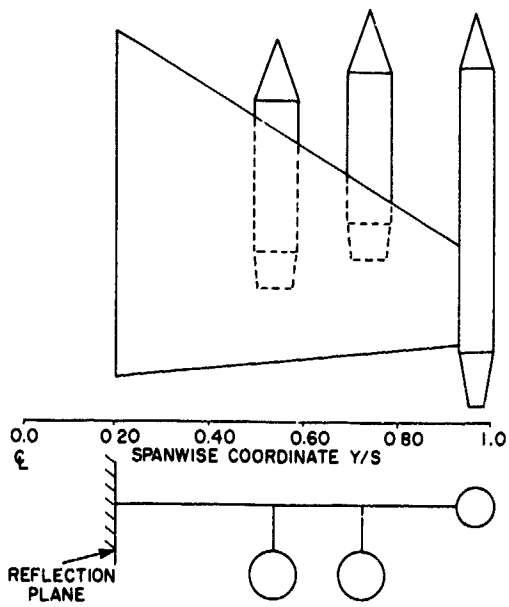

FIG. 19: AERODYNAMIC CONFIGURATION FOR DOUBLET LATTICE

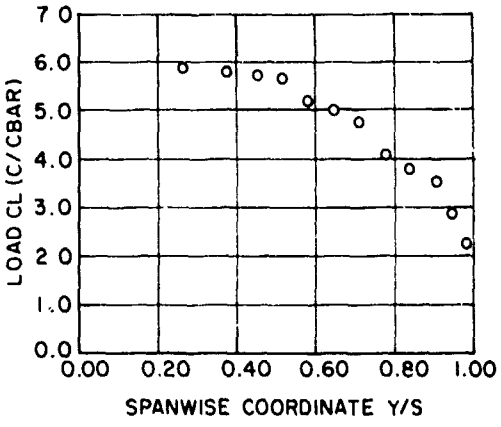

FIG. 20a: CF-5 STEADY STATE LOAD DISTRIBUTION

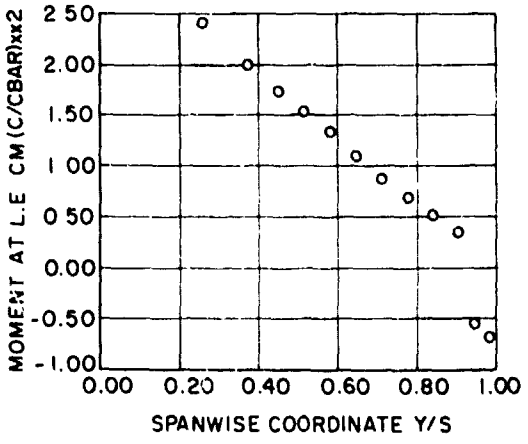

FIG. 20b: CF-5 STEADY STATE MOMENT DISTRIBUTION

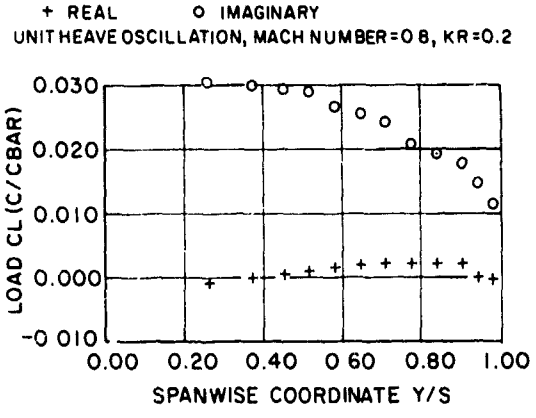

FIG. 21a: CF-5 COMPLEX AERODYNAMIC LOAD DISTRIBUTION

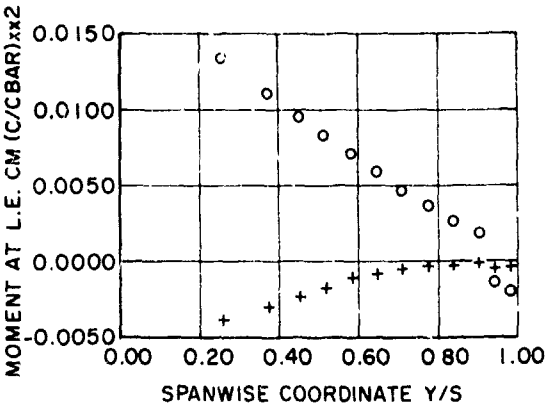

FIG. 21b: CF-5 COMPLEX AERODYNAMIC MOMENT DISTRIBUTION

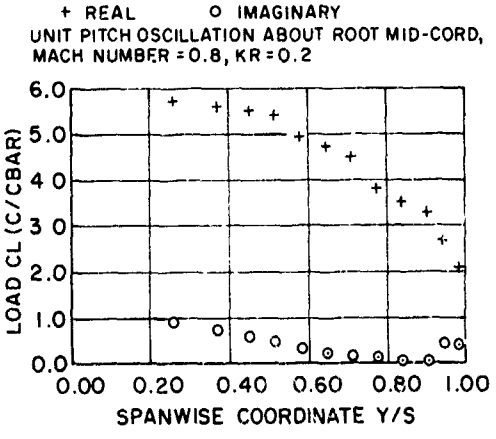

FIG. 22a: CF-5 COMPLEX AERODYNAMIC LOAD DISTRIBUTION

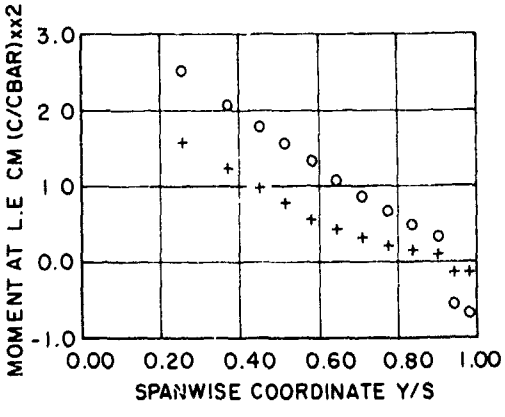

FIG. 22b: CF-5 COMPLEX AERODYNAMIC MOMENT DISTRIBUTION

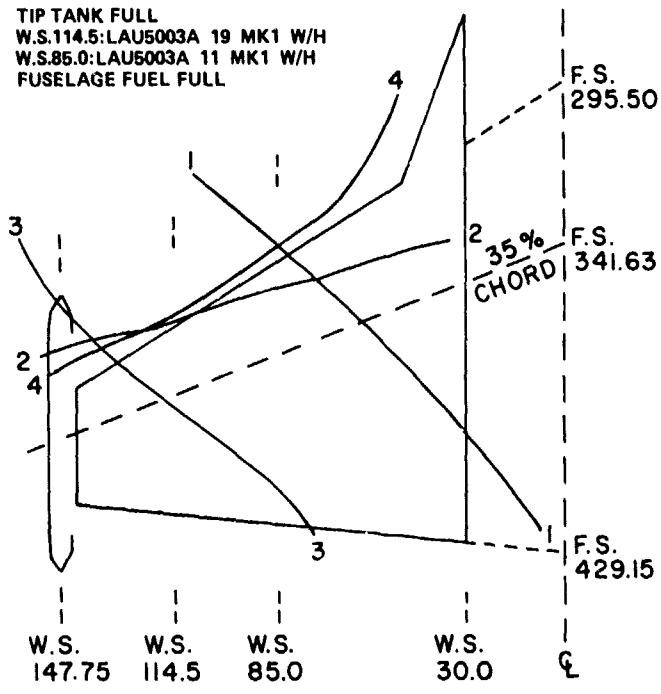

FIG. 23: CF-5 WING NODE LINES

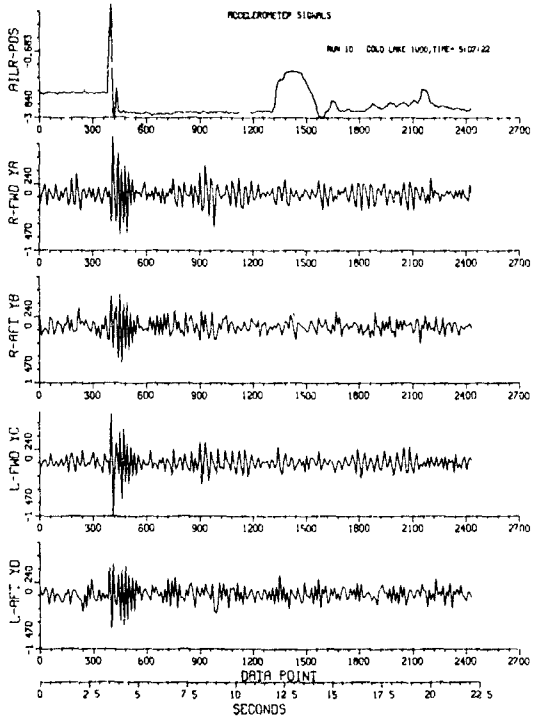

FIG. 24: TYPICAL PLOTS OF AILERON POSITION AND ACCELEROMETER SIGNALS

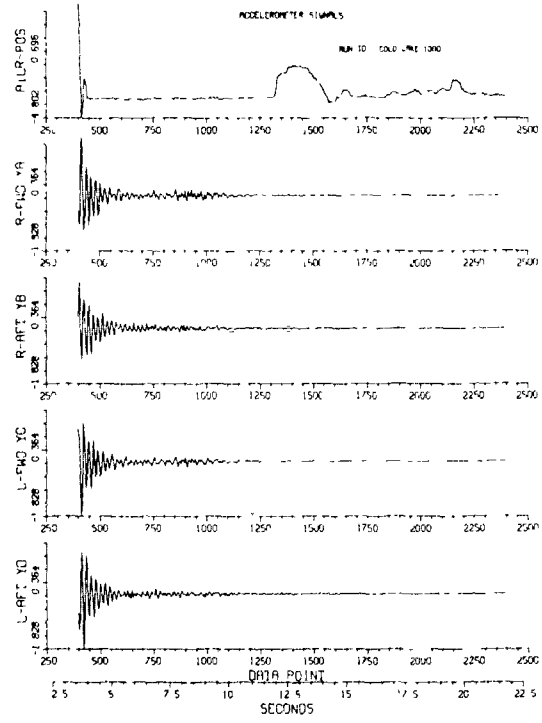

FIG. 25: AILERON POSITION AND ACCELEROMETER SIGNALS WITH EXPONENTIAL WINDOW APPLIED

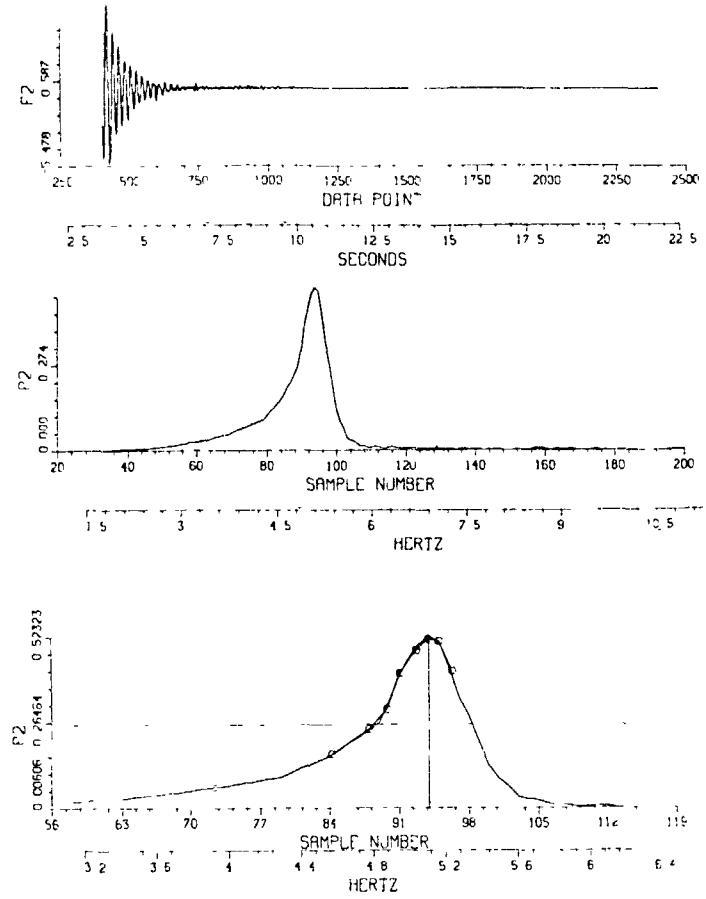

FIG. 26: TIME HISTORY OF FUNCTION F_2 AND POWER SPECTRAL DENSITY PLOTS FOR ANTI-SYMMETRIC TORSION MODE

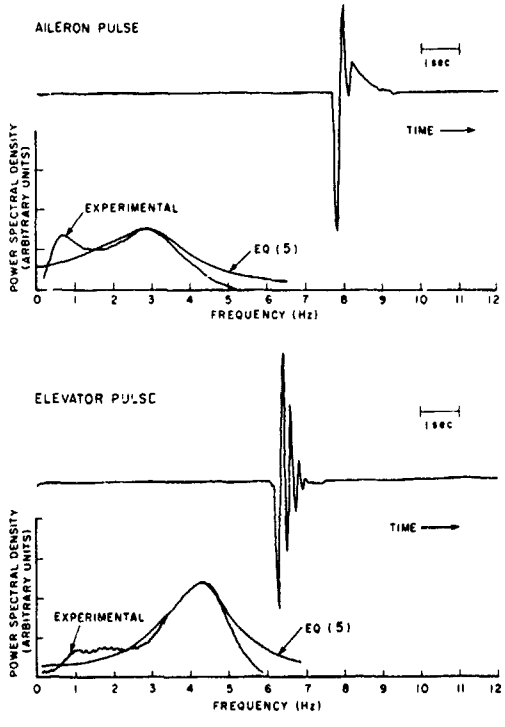

FIG. 27: TIME HISTORY AND POWER SPECTRAL DENSITY FOR AILERON AND ELEVATOR DISPLACEMENTS

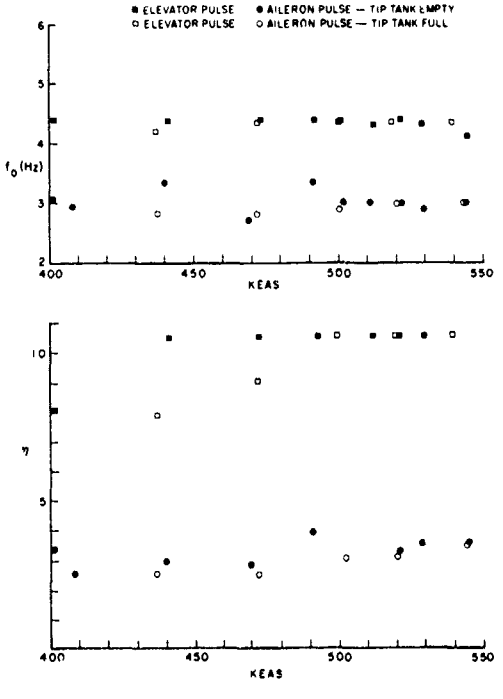

FIG. 28: VARIATION OF FREQUENCY AND η WITH AIR SPEED

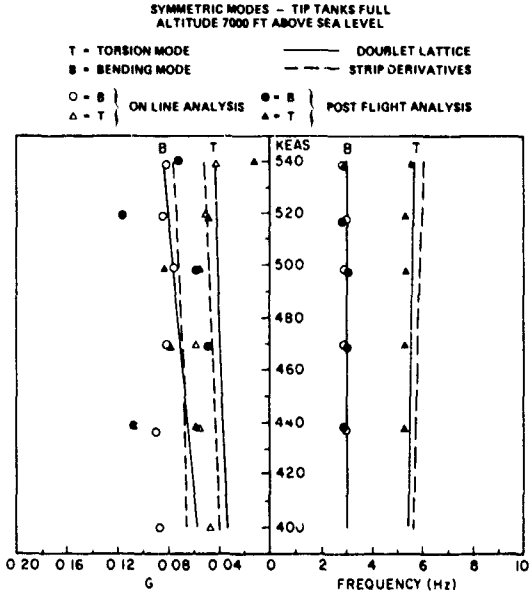

FIG. 29: DAMPING AND FREQUENCY FOR SYMMETRIC MODES WITH FULL TIP TANKS

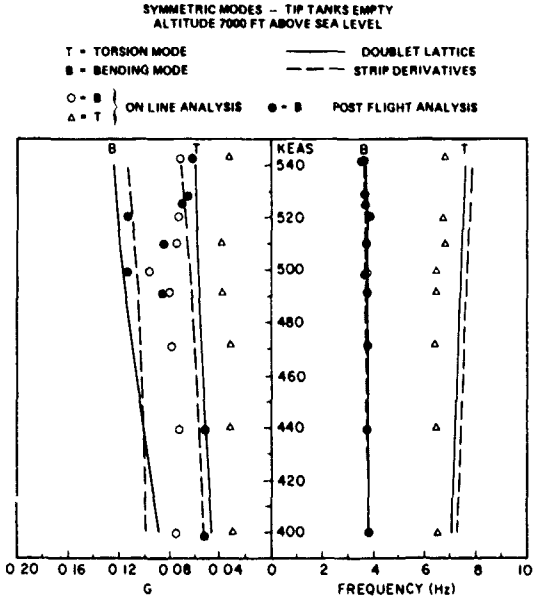

FIG. 30: DAMPING AND FREQUENCY FOR SYMMETRIC MODES WITH EMPTY TIP TANKS

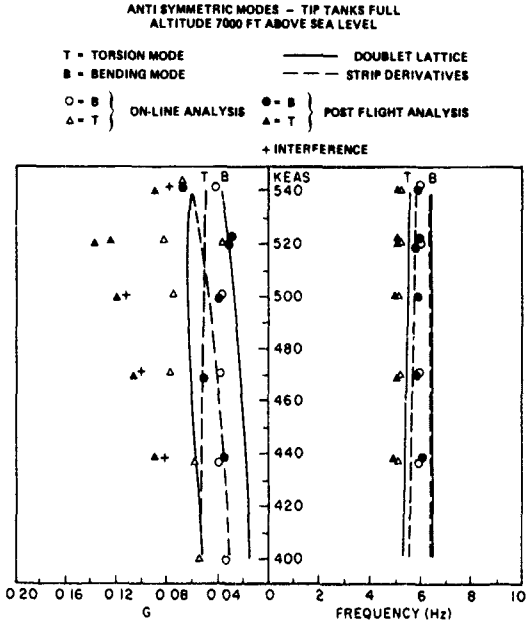

FIG. 31: DAMPING AND FREQUENCY FOR ANTI-SYMMETRIC MODES WITH FULL TIP TANKS

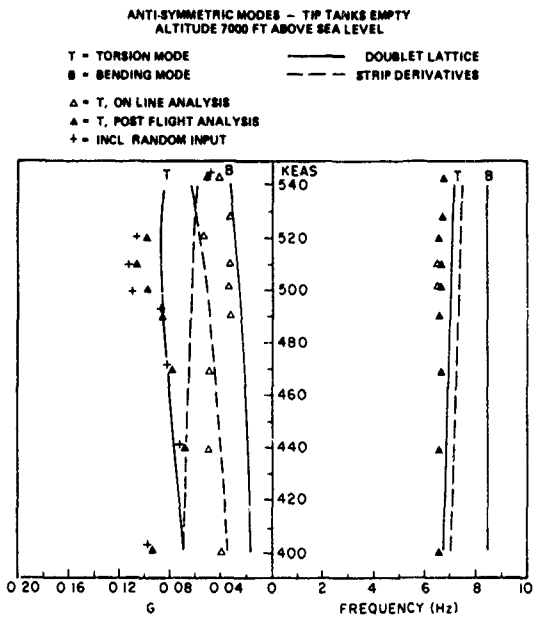

FIG. 32: DAMPING AND FREQUENCY FOR ANTI-SYMMETRIC MODES WITH EMPTY TIP TANKS

FLUTTER INVESTIGATIONS IN THE TRANSONIC FLOW REGIME FOR A FIGHTER TYPE AIRCRAFT

by

W. Luber
H.Schmid

MESSERSCHMITT-BÖLKOW-BLOHM GMBH.
Unternehmensbereich Flugzeuge
Postfach 801160 - 8 München 80
W.-Germany

SUMMARY

A correction method for subsonic potential airforces especially for the transonic flow regime is proposed. The airforces are corrected by modifying the theoretical pressure coefficients locally with measured static pressure slopes. Trends of transonic airloads and moments with reduced frequency, Mach-number and mean static incidence are given. The application of corrected airforces in flutter calculations is described, and its effect on flutter behaviour is analyzed. It could be confirmed by analysis that the aerodynamic damping of the most important low-frequency vibration modes is reduced by aerodynamic transonic effects, which was indicated by flight flutter test results.

1. LIST OF SYMBOLS

c_p, Δc_p	pressure coefficient, pressure jump
c_l	sectional steady lift coefficient normal to elastic axis
$c_L = L/q \cdot S$	lift coefficient
$C_M = M/q \cdot S \cdot s$	wing bending moment coefficient in 1st wing bending mode
g	aerodynamic damping coefficient
k	reduced frequency
M_∞, M_{loc}	free-stream, local Mach number
NORA	abbreviation for the organisations NLR, ONERA, RAE and AVA
q	stagnation pressure
S	surface
s	semispan
V_f	flutter speed
V_r	reference speed
$w = w' + iw''$	elements of NLR correction matrix
α_o	mean incidence of aircraft
$\alpha = \alpha' + i\alpha''$	amplitude of unsteady angle of attack
ϕ	velocity potential
ϕ_x	longitudinal wash
l.e.	leading edge
t.e.	trailing edge

2. INTRODUCTION

It is well known that the most common used linear flat-plate theories for predicting unsteady airloads fail in the transonic flow regime. The reasons for this fact are phenomena as shocks and their movement with periodic deflections, flow separation, viscous or boundary layer effects, non-linear aspects, appearance of bubbles etc. At high angles of attack these effects become more pronounced and seem to move beyond the point to be treated any longer by linear calculation methods.

Therefore, there is an urgent need for approximate transonic techniques for estimating 3-d unsteady airforces.

A list of trials in this direction - far from being complete - is given below.

E.C. Yates (Ref. 1, 2) presented a modified-strip-analysis method for flutter calculations. The steady state spanwise local lift distributions c_l and spanwise aerodynamic center locations $a_{c,n}$ (normal to elastic axis) are required as aerodynamic input parameters for determining the oscillatory lift- and moment distributions. If measured aerodynamic data are used instead of pure theoretical ones it is assumed that viscous and transonic effects are incorporated automatically, at least in terms of nearly steady flow.

The NLR correction procedure of Bergh and Zwaan (Ref. 3) is based on unsteady pressure measurements for a given single vibration mode and assumes that the data information can be transferred to all other modes. The correction expression is given by

$$\left(\Delta C_p' + \iota \Delta C_p''\right)_{corr} = \left(\Delta C_p' + \iota \Delta C_p''\right)_{theo} \cdot \left(w' + \iota w''\right) \qquad (1)$$

The correction is a local one, independent of vibration modes but dependent of reduced frequency; w are the elements of the diagonal and complex[W]matrix. They can be evaluated if the above relation is solved for w, where the subscribt "corr" has to be replaced by "exp": $w = \left(\frac{\Delta C_{p,exp}}{\Delta C_{p,theo}}\right)_{\text{test mode}}$. Both magnitude and phase of theoretical loading are changed. Because only incompressible results are reported by the authors, the extension of this technique to transonic flow conditions is yet unproved and questionable.

A strip theory for calculating the aero-damping in fundamental bending mode is described by Lambourne (Ref. 4). The theory starts from given steady pressure measurements on a rigid model and its variation with incidence up to and beyond buffet onset. By using the rate of change of spanwise normal force distributions with steady incidence, it is a quasi-steady strip procedure. Contrary to Yates, Lambourne doesn't introduce Theodorsen's complex circulation function limiting the application of his theory to small values of reduced frequency.

A new approach to transonic loads was given by Garner (Ref. 5, 6), correcting the theoretical complex longitudinal wash by local ratios of test pressure slopes to theoretical pressure slopes. The ratios are assumed to be independent of pressure inducing modes:

$$\left(\phi_x' + \iota \phi_x''\right)_{corr} = \left(\phi_x' + \iota \phi_x''\right)_{theo} \left(\frac{(\partial c_p/\partial \alpha)_{exp}}{(\partial c_p/\partial \alpha)_{theo}}\right)_{steady} \qquad (2)$$

Even if an exact 2-dimensional nonlinear transonic (small pertubation) method is available, one has to adapt for 3-dimensional flows. In a study reported by Couston (Ref. 7), three steady corrections were used to account for viscosity, effective Mach-number and induced stationary angle of attack besides one unsteady correction describing the effective motion of the lifting surface or the effective boundary condition. Since even 2-d transonic airloads are not easy to be determined, such an analysis together with the necessary modifications is not very practicable.

3. DETERMINATION OF THEORETICAL AIRLOADS

For predicting unsteady airloads, the doublet lattice method (DLM) according to Rodden, Giesing and Kálmán (Ref. 8) was chosen because local pressures are obtained directly and not via pressure series. In principle, the same acceleration potential kernel is used as for lifting surface methods but in a somewhat different notation, given by Landahl (Ref. 9).

The DLM is a finite element method and is characterized by trapezoidal panels the vorticity distribution of which is concentrated in the quarter chord lines and whose downwash control points are situated at the 3/4 chord lines. The wing planform of the fighter type aircraft and its subdivision into panels is given in Fig. 1.

4. CORRECTION OF UNSTEADY PRESSURES AND GENERALIZED AIR FORCES

The wing generalized airforces in the transonic flow regime are corrected by modifying the local pressures for the interesting conditions like configuration (clean aircraft or wing with stores), sweep angle, Mach-number, steady pre-inclination of aircraft, inducing deflection mode, (reduced) frequency. Since the correction is punctual, amplitude and phase (or real and imaginary part) of integrated forces were changed as well. Two correction procedures were investigated.

4.1 Multiplicative Correction

The expression for the first version reads as follows:

$$\left(\Delta C_p' + i\,\Delta C_p''\right)_{corr} = \left(\Delta C_p' + i\,\Delta C_p''\right)_{theo} \left(\frac{(\partial \Delta C_p/\partial \alpha)_{exp}}{(\partial \Delta C_p/\partial \alpha)_{theo}}\right)_{steady} \qquad (3)$$

The local factors (ratios) depend on configuration, on Mach-number and on steady state pre-inclination, and are assumed applicable to all pressure generating deflection modes. If the ratios become negative, the phases of the theoretical pressures are changed besides the amplitudes.

4.2 Additive Correction (Incremental Correction)

The second applied correction version can be written in the following complex form:

$$\left(\Delta C_p' + i\,\Delta C_p''\right)_{corr} = \left(\Delta C_p' + i\,\Delta C_p''\right)_{theo} + \left(\left(\frac{\partial \Delta C_p}{\partial \alpha}\right)_{exp,\,M_\infty} - \left(\frac{\partial \Delta C_p}{\partial \alpha}\right)_{theo}\right)_{steady} \cdot \left(\alpha' + i\,\alpha''\right)_{mode\ \mu} \qquad (4)$$

The correction by increments depends (via the term α) not only on the Mach-number and the steady state inclination but on the modes and on the reduced frequency too.

The corrected pressures tend with $k \to 0$ and $(\kappa' + i\,\kappa'') \to 1$ towards $(\partial \Delta c_p/\partial \kappa)_{exp}$ because the terms $\Delta C' + i\Delta C_p''$ and $\left(\partial \Delta c_p/\partial \kappa\right)_{theo,\,steady}$ cancel each other. Both corrections therefore become more reliable the smaller the frequencies are.

5. EVALUATION OF EXPERIMENTAL LOCAL PRESSURE SLOPES

Transonic wind tunnel tests on a 1/14 scaled entire airplane model were evaluated by plotting vs. chord upper and lower side pressures at given sections normal to the elastic axis and at chosen inclinations α_1, α_2. If necessary, curves were smoothed graphically. Then pressure differences were produced and their local slopes according to

$$\left(\frac{\partial \Delta c_p \langle x, y \rangle}{\partial \alpha}\right)_{exp} = \frac{\Delta C_p \langle x, y, \alpha_2 \rangle - \Delta C_p \langle x, y, \alpha_1 \rangle}{\alpha_2 - \alpha_1} \qquad (5)$$

For analytical treatment, the DLM method was employed, and the wing planform was divided into 54 panels (see Fig. 1). At the theoretical collocation points the experimentally given slopes (Eq. 5) were determined by interpolation and extrapolation.

6. REMARKS

Both correction methods can be justified. As already mentioned, they are limited to low reduced frequencies, but confirming experimental data are yet lacking. One example for which the correction could be approved experimentally is given in Fig. 2. The multiplicative and additive correction was applied to upper-side-pressures of the "NORA"-wing-model (for detailed test conditions, see figure description and Ref. 11). The comparison of the test data with theoretical and corrected ones show that an improvement can be obtained with respect to the in-phase pressures, though the peak is overpredicted in both cases. For the imaginary pressure distribution the incremental correction is only a slight improvement of the linear theory while the multiplicative correction apparently fails. For this reason and for reasons concerning trend studies with k (not described here), the latter approach was no longer applied.

7. AERO - RESULTS

7.1 Steady Flow Pressure Curve Slopes (Derivatives)

Chordwise experimental and theoretical steady pressure slope distributions are the basis of aforementioned correction. A typical diagram is shown in Fig. 3. For each geometrical arrangement of the fighter stores and pylons and for each parameter configuration (Mach-number and angle of attack), a set of 9 similar pictures (according the 9 DLM streamwise strips) has to be produced, out of which local differences were taken and fitted into the modified DLM programme. Expressed in quasi-steady terms a negative value of $\left(\partial \Delta c_p/\partial \kappa\right)_{exp}$ means that any deflection mode will be excited at that collocation point or nearby.

7.2 Corrected Local Pressure Jumps

Pressure plots in the 1st wing bending mode along selected DLM streamwise sections are given in Fig. 4. In detail, we can see theoretical pressures and corrected pressures according to Eq. 4.

For the inner chords, say 3 and 4, the agreement between $\Delta C_{p_{corr}}$ and the predictions is fairly good while along the outboard chords the experimentally corrected curves show a similar characteristic but partly large deviations from theory.

7.3 Corrected Integrated Forces and Moments

Wing lift of the clean configuration in 1st wing bending mode vs. frequency parameter k is shown in Fig. 5.

At constant reduced frequency k we can observe that all real and imaginary parts in the sequence "not corrected, clean corrected 2°, 4.5°, 12°". This sequence doesn't change with varying k, since the in-phase correction term is independent of k and the out-of-phase term a linear function of k.

The corrected values therefore show the same behaviour than the theoretical ones when plotted versus reduced frequency.

Diagram 6 shows the wing bending moment associated with wing bending motion.

The variation of real parts and imaginary parts with reduced frequency is uniform and steady. The effect of the different mean angles of attack on the moment coefficient is the same as observed with the lifts (Fig. 5.).

In Fig. 7 the wing bending moment coefficient in wing bending mode is plotted versus Mach-number. It decreases with increasing Mach-number. For both Mach-numbers wind tunnel tests with a tank on the inboard wing and a store on the outboard wing were evaluated.

8. FLUTTER ANALYSIS

The flutter results presented in this paper use the additive correction. Three-dimensional corrected unsteady aerodynamic forces were calculated only for the wing. Previous investigations showed that in most cases the influence on flutter behaviour caused by unsteady aerodynamic forces on external stores and store-wing interference effects are very small (Ref. 10). Therefore unsteady aerodynamic effects due to stores are not considered here.

According to the wind tunnel measurements, calculations were performed for Mach 0.9 and 0.95.

8.1 Representation of Aircraft Structure

A simplified analytical model of the advanced fighter type aircraft was used for the investigations presented here. The 45° sweptback wing could be idealized by a beam whereas the attachments for the inboard and outboard wing pylons were represented by individual points. It could be demonstrated by preceding analyses that the flexibility of fin, taileron and fuselage have little effect on store flutter. For this reason these components were assumed to be rigid.

Structural damping as measured in ground resonance tests was not taken into account here.

Using the "Required Damping Method" the flutter equation was solved for the equivalent amount of structural damping g necessary for harmonic motion.

9. FLUTTER RESULTS

The following discussion will concentrate on some selected results where the effects of corrected aerodynamic forces are considerable.

9.1 Clean aircraft

First, flutter results for the clean configuration are shown which were obtained by evaluating the corresponding wind-tunnel tests on the same clean configuration. In Fig. 8 the first two mode shapes are depicted which affect the flutter behaviour. Fig. 9 shows the considerable influence of modified airforces on flutter speeds at Mach 0.9 for the three investigated steady-state incidences $\alpha_0 = 2°, 4.5°$ and $12°$. It is evident that the dampings of the wing bending mode and of the fuselage bending mode decrease, if correction is applied. Comparing the two modes we observe that at high angles of attack the wing bending mode shows a detrimental instability while the fuselage bending flutter instability occours at a higher velocity. The frequency of the wing bending mode is increased from 7.9 Hz to 12.2 Hz.

In addition to this symmetrical analysis an antisymmetrical analysis for the same Mach-number, identical configuration and the same mean incidence was done using the equivalent antisymmetrical aerodynamics and natural modes. Because the results were quite similar they will not be shown here.

9.2 Inboard and outboard underwing store configuration

The second example deals with the influence of transonic airloads in flutter analyses for a symmetrical inboard and outboard underwing store configuration. The most important resonance mode shapes are depicted in Fig. 10. Fig. 11 illustrates the influence of corrected aerodynamic forces at Ma 0.9 and Fig. 12 shows the effect at Ma 0.95.

Comparing the V-g plots obtained for two Mach-numbers the most significant flutter phenomena will be discussed now.

In both graphs the lowest flutterspeed is obtained by using pure theoretical aerodynamics. There are drastic damping reductions in the wing bending mode at high angles of attack. This effect is especially pronounced for M = 0,95.

Although for this configuration the lowest possible flutter speed was already found employing theoretical aerodynamics, the results may become important, if wing bending reveals as the flutter critical mode like it was in the clean case. Admittedly this guess is not proved by the present calculations.

9.3 Outboard store configuration

The last example is given by an underwing outboard store configuration oscillating symmetrically and three fundamental resonance mode shapes of which are sketched in Fig. 13.

As can be deduced from Fig. 14 and Fig. 15 the correction for mean angles of 2°, 4° and 6° affects only the bending branch to a great extent. Additional statements about the flutter behaviour do not result from these calculations.

10. CONCLUSION:

It should be pointed out that determination of pressure gradients with respect to mean incidence demand high accuracy and repeatability of tunnel data. For a critical consideration one should take this fact into account.

In addition we emphasize again that the present correction mechanism is not yet proved sufficiently by experiment and is valid only for low reduced frequencies.

The present results indicate that the conservative flutter behaviour with pure theoretical aerodynamics changes if corrections are applied. At high mean incidences a possible instability of wing bending mode was found.

11. REFERENCES

1) E.C.YATES Jr.: Modified-Strip-Analysis Method for Predicting Wing Flutter at Subsonic to Hypersonic Speeds.
J. Aircraft, Vol. 3, No. 1, 1966, pp. 25-29

2) E.C.YATES Jr., R.M. BENNETT: Analysis of Supersonic-Hypersonic Flutter of Lifting Surfaces at Angle of Attack.
J. Aircraft, Vol. 9, No. 7, 1972, pp. 481 - 489

3) H.BERGH, R.J. ZWAAN: A Method for Estimating Unsteady Pressure Distributions for Arbitrary Vibration Modes from Theory and from Measured Distributions for one Single Mode.
NLR-TR F.250, 1966

4) N. C. LAMBOURNE: Some Remarks on the Aerodynamic Damping Appropriate to Wing Buffeting.
RAE Technical Memorandum Structures 871, 1975.

5) H. C. GARNER: A Practical Framework for the Evaluation of Oscillatory Aerodynamic Loading on Wings in Supercritical Flow.
RAE Tech. Memo Structures 900, 1977 or
AGARD-CP-226, Paper 16 (1977)

6) H. C. GARNER, B. W. PAYNE: Experimental Flutter at High Subsonic Speeds and its Theoretical Prediction, Taking into Account Wing Thickness and Reynolds Number.
AGARD-CP-296, Paper 7 (1980)

7) M. COUSTON, J.-J. ANGELINI, J.-L. MEURZEC: Comparaison de Champs de Pression Instationnaires Calculés et Mesurés sur le Modèle ZKP.
ONERA Rept. Provisoire, 1980

8) W. P. RODDEN, J. P. GIESING, T. P. KÁLMÁN: New Developments and Applications of the Subsonic Doublet-Lattice Method for Nonplanar Configurations.
Douglas Paper 5826 (1970)

9) M. T. LANDAHL: Kernel Function of Nonplanar Oscillating Surfaces in a Subsonic Flow.
AIAA J. V.5, May 1967, pp. 1045 - 1046

10) J. BECKER, H. SCHMID: Unsteady Load Predictions for External Stores.
MBB-Rept. No. UFE 1266, July 1976

11) N. LAMBOURNE, R. DESTUYNDER, K. KIENAPPEL, R. ROSS: Comparative Measurements in Four European Wind Tunnels of the Unsteady Pressures on an Oscillating Model (The NORA Experiments).
AGARD-R-673 (1979)

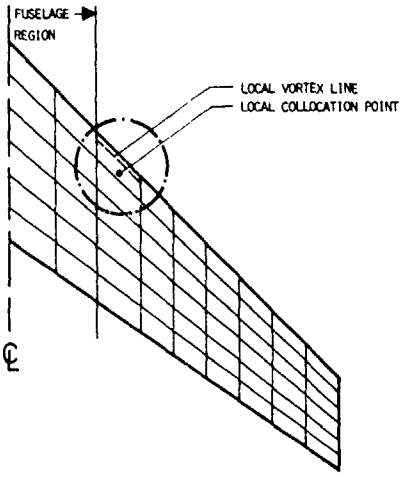

FIG. 1 WING PLANFORM DIVIDED INTO PANELS. BOUND VORTEX AT LOCAL 1/4 CHORD LINE, DOWNWASH COLLOCATION POINT AT 3/4 CHORD

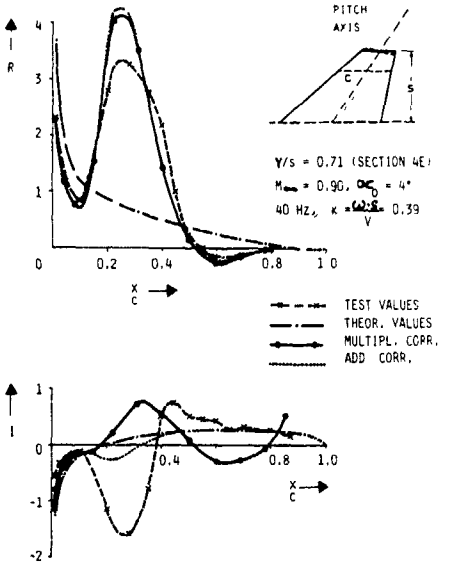

FIG. 2 UPPER SIDE PRESSURE DISTRIBUTION ON NORA-WING ROTATING ABOUT INDICATED AXIS. R = −p'/p_TOTAL, I = −p''/p_TOTAL

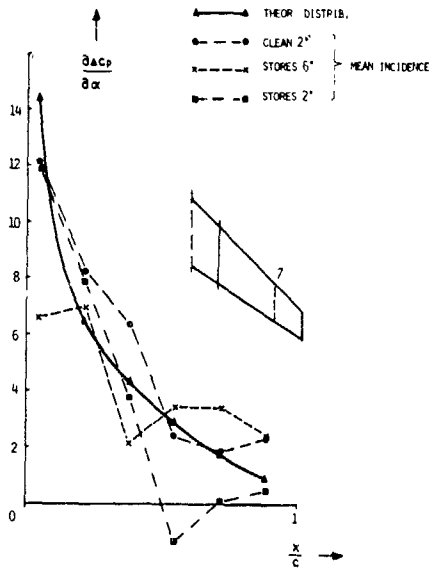

FIG. 3 SLOPE OF STEADY PRESSURE DIFFERENCE AT VARIOUS TEST CONDITIONS. 45° SWEPTBACK WING, SECTION "7", M = 0.9

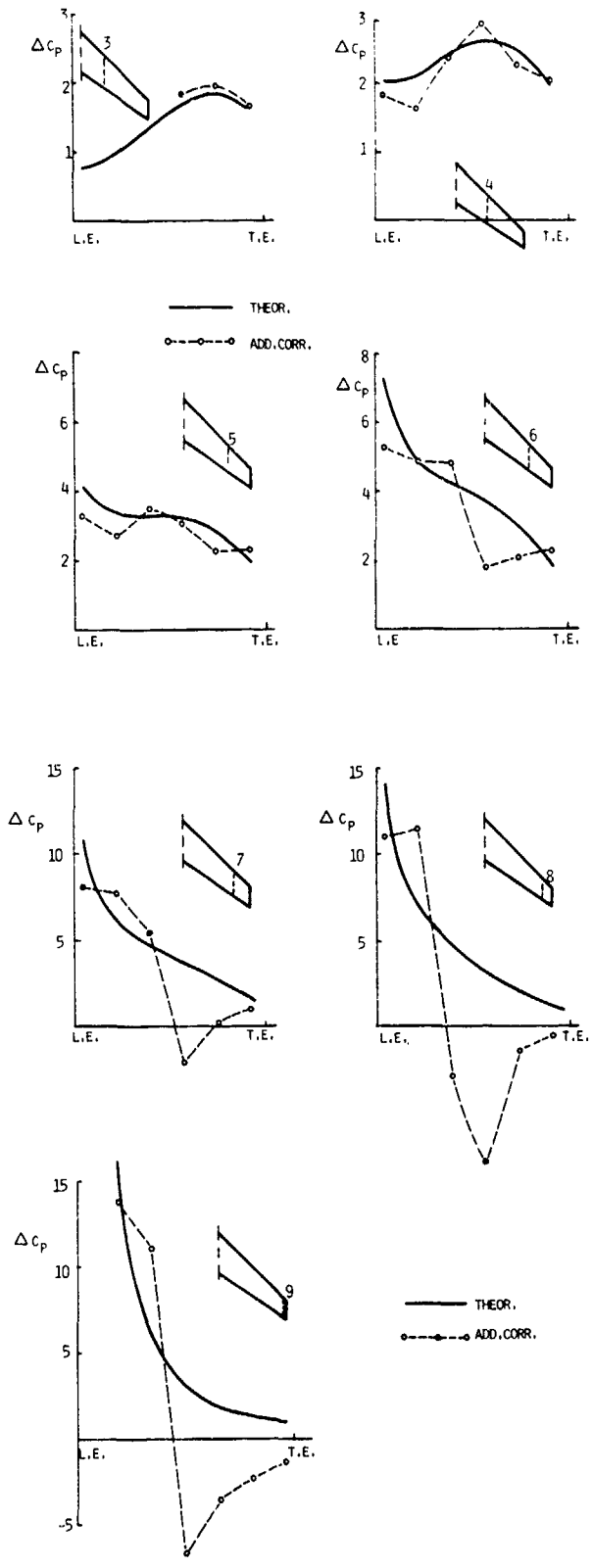

FIG. 4 CHORDWISE PRESSURE DISTRIBUTIONS FOR 7 DLM SEMISPAN STATIONS AT M = 0.9 , k = 0

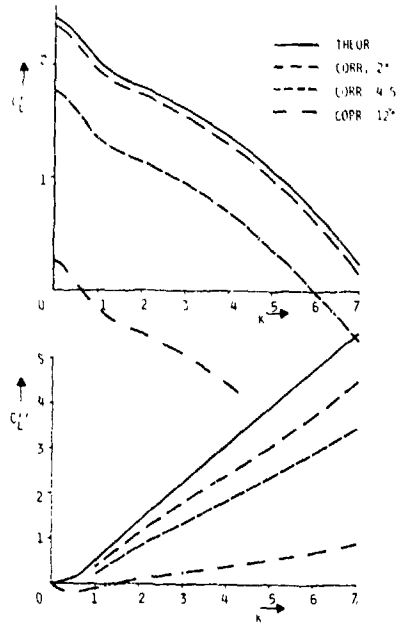

FIG. 5 VARIATION OF LIFT-COEFFICIENT IN SYMM. BENDING WITH REDUCED FREQUENCY.

M = 0.9, CLEAN CONFIGURATION

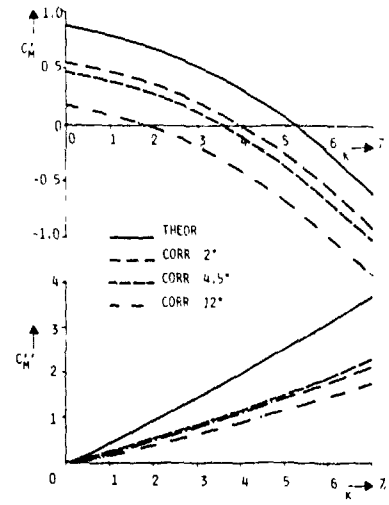

FIG. 6 VARIATION OF WING BENDING MOMENT-COEFFICIENT WITH REDUCED FREQUENCY.

M = 0.9, CLEAN CONFIGURATION, SYMMETRICAL CASE

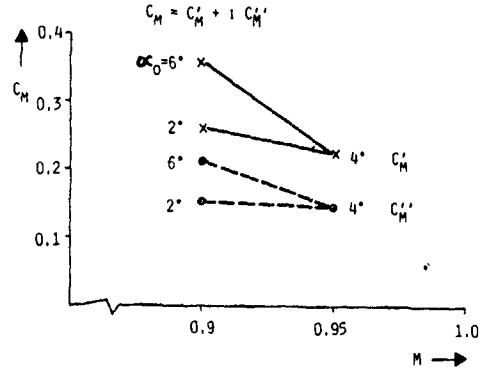

FIG. 7 SYMMETRICAL WING BENDING MOMENT COEFFICIENT VERSUS MACH-NUMBER. WING STORE CONFIGURATION ADDITIVE CORRECTION, k = 1

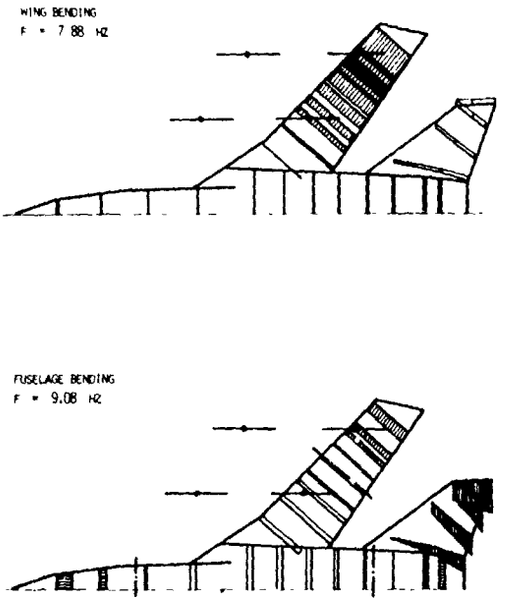

FIG. 8 CALCULATED SYMMETRICAL NORMAL MODES FOR CLEAN AIRCRAFT

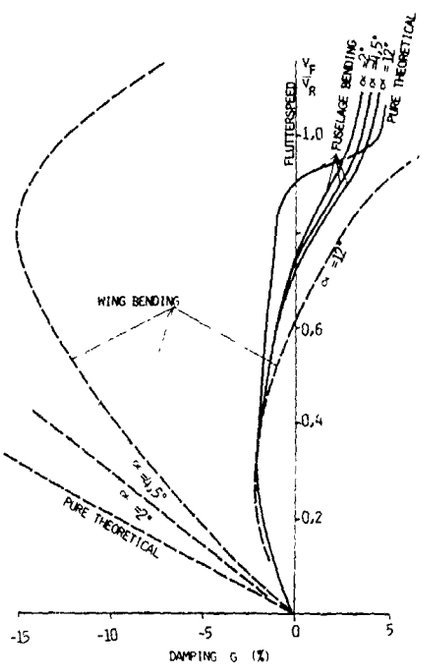

FIG. 9 VARIATION OF DAMPING WITH FLUTTERSPEED FOR CLEAN AIRCRAFT MACH = 0.9

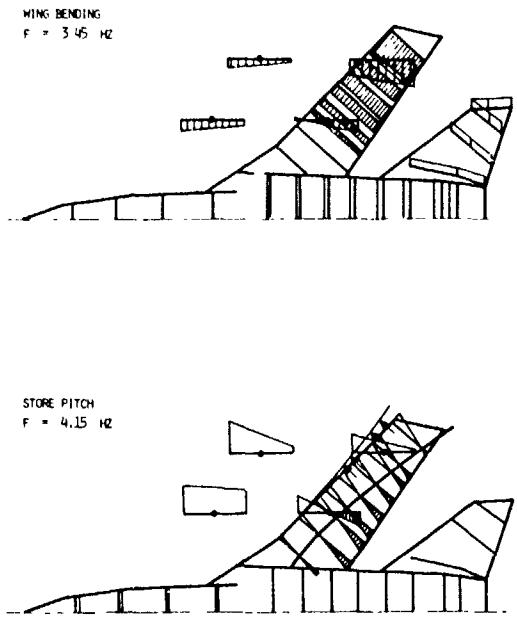

FIG. 10 CALCULATED SYMMETRICAL NORMAL MODES FOR AIRCRAFT WITH INBOARD AND OUTBOARD STORE CARRIAGE

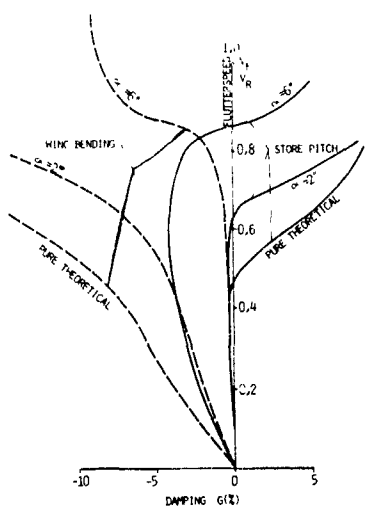

FIG. 11 VARIATION OF DAMPING WITH FLUTTERSPEED FOR INBOARD AND OUTBOARD STORE CARRIAGE MACH = 0.9

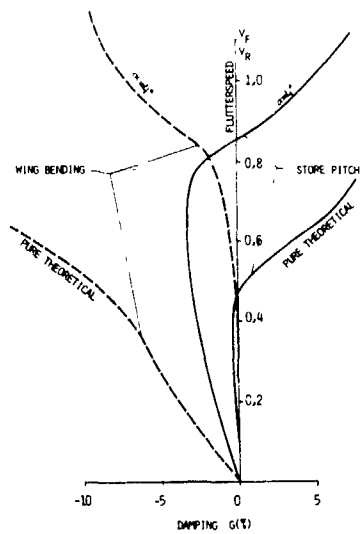

FIG. 12 VARIATION OF DAMPING WITH FLUTTERSPEED FOR INBOARD AND OUTBOARD STORE CARRIAGE MACH = 0.95

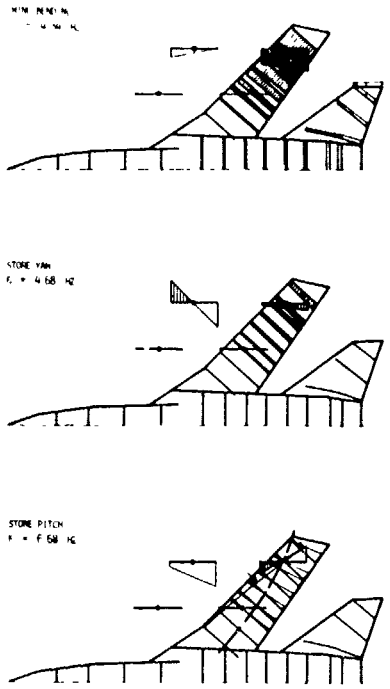

FIG 13 CALCULATED SYMMETRICAL NORMAL MODES FOR AIRCRAFT WITH OUTBOARD WING STORE CARRIAGE

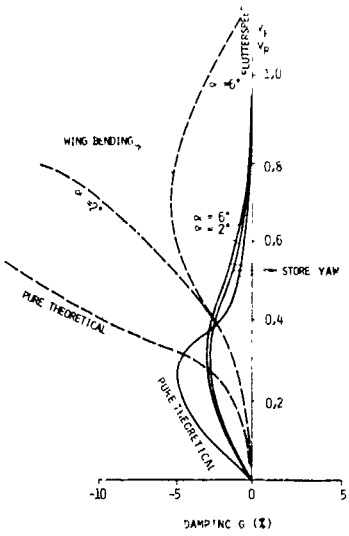

FIG. 14 VARIATION OF DAMPING WITH FLUTTERSPEED FOR OUTBOARD STORE CARRIAGE MACH = 0.9

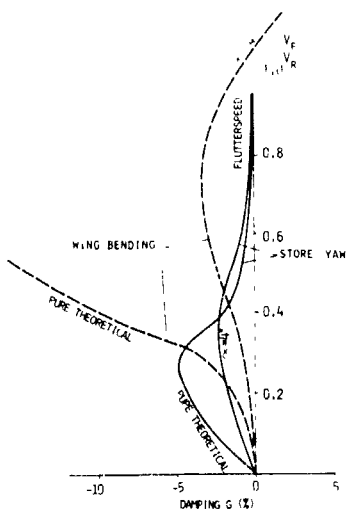

FIG. 15 VARIATION OF DAMPING WITH FLUTTERSPEED FOR OUTBOARD STORE CARRIAGE MACH = 0.95

FLUTTER AND STEADY/UNSTEADY AERODYNAMIC CHARACTERISTICS OF SUPERCRITICAL AND CONVENTIONAL TRANSPORT WINGS

by

William F. Grosser
Staff Specialist-Flutter
R. T. Britt
Dynamics Engineer, Senior
C. B. Childs
Dynamics Engineer
O. J. Crooks
Specialist Engineer

Preliminary Design Structures Department
Lockheed-Georgia Company
Marietta, Georgia 30063

and

F. W. Cazier, Jr.
Aerospace Engineer
Loads and Aeroelasticity Division

NASA-Langley Research Center
Hampton, Virginia 23665

SUMMARY

This paper presents the technical details and results of a high-speed wind-tunnel test program of an aeroelastic cantilevered transport type wing with two pylon-mounted engines. The tests were conducted in the NASA-Langley 16-foot Transonic Dynamic Tunnel (TDT) during December 1981. Flutter boundaries were determined for an advanced technology supercritical airfoil and a conventional airfoil of identical planforms, mass properties, and stiffness. The test parameters included different values of model stiffness and wing loading at various angles of attack. The models were instrumented at spanwise wing stations to determine bending and torsion deflections and vertical accelerations. At two model wing stations, pressure transducers were distributed along the chord to record static and unsteady oscillatory pressures during the approach to and onset of flutter. This paper presents the test program with results of the flutter characteristics and selected steady and unsteady aerodynamic data for both airfoils at different angles of attack for various Mach numbers and dynamic pressures.

INTRODUCTION

For more than 20 years, engineers have considered high-speed flutter model testing to be necessary as final verification before first flight that an aircraft is free from flutter. Why has the flutter engineer had to choose such an expensive and difficult method? In the early days of high-speed aircraft design, the aeroelastician realized that non-compressible aerodynamic theory and flutter model testing in a low-speed wind tunnel would not define the sensitivity of flutter to compressible-flow effects, which could greatly reduce the flutter speed. The complex effect of transonic aerodynamics on flutter appears to be even more important with the advent of the supercritical airfoil designs. Recent model tests indicate conflicting results as to the severity of the compressibility effects of supercritical airfoils on flutter speed. Several of the more important factors considered have been Reynolds number and angle of attack, which can vary considerably throughout the flight envelope (see References 1 and 2).

An investigation was initiated by the Lockheed-Georgia Company to determine a practical and inexpensive experimental aeroelastic model program that would provide insight into the effects of Reynolds number and angle of attack on various airfoil designs regarding flutter. Also, if we could determine the flutter boundaries, why not gather additional information from the same tests: the steady and unsteady aerodynamic behavior as flutter was approached and at the onset of flutter? This investigation quickly settled around the type of model design that would achieve these objectives. In the early days of high-speed testing, flutter modeling technology followed similar designs used for low-speed testing: a single-spar design with sectionalized aerodynamic sections attached to it. This simple and economical design made it relatively easy to match the stiffness, mass, and aerodynamic airfoils of a full-scale aircraft. High-speed models were tested for many years, using this sectionalized model construction, however there was increasing concern that the unevenness and gaps between the sections created interference with the formation of shock waves and other aerodynamic characteristics. As a consequence, smooth skin models have been built recently. However, if the sectionalized model design with its advantages - ease in matching mass and stiffness, simpler construction, and ease of model changes, thereby shortening tunnel test time - could be proven to be technically satisfactory, this design would still be desirable. In order to evaluate the effects of sectionalized models, an investigative test was conducted in the Lockheed-Georgia Company Compressible Flow Facility (see Reference 3). The test model shown in Figure 1 has airstream chordwise slots which represent two typical section widths of a sectionalized model. The outboard slot near the wingtip represented only the inboard side of a typical section, since the aerodynamic flow characteristics would normally be outward and beyond the pressure ports. The slot depths were nominally 0.125 inch, and the leading and trailing edges were cut through approximately three-quarters of an inch from their respective edge. The gap widths, approximately 0.05 inch, were also scaled proportionally to larger model gaps. The aerodynamic airfoil was of an advanced supercritical design.

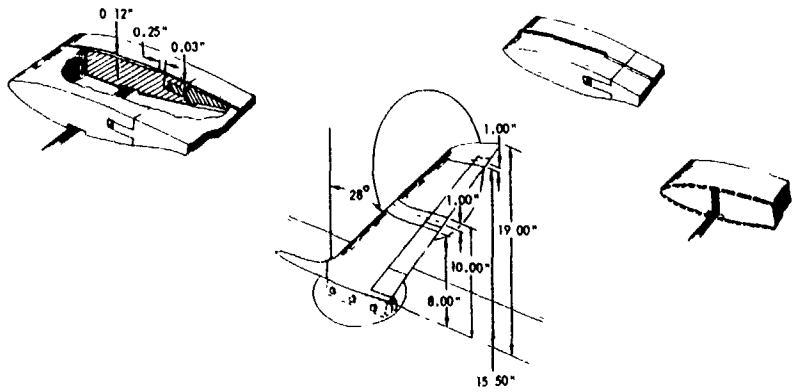

Figure 1. Slotted Wing Test Model Used for Aerodynamic Study

Five slot configurations were tested to simulate the various conditions that were considered important in comparing a sectionalized model with a smooth-skin model. The first slot configuration was with the slots open; the second configuration was with soft foam rubber in the slots; the third and fourth configurations were with fences in the slots which were 1/8" and 1/16", respectively, above the wing surface to typify the steps that result when a flexible model twists; the fifth configuration was with the slots filled and sanded smooth with the surface. Each of the five slot configurations was tested at four Mach numbers: 0.67, 0.80, 0.875, and 0.95; and at five angles of attack: -2°, -1°, -0°, $+1^{\circ}$, and $+2^{\circ}$ at each Mach number.

The model was mounted in the tunnel on the five-component strain-gage balance. The model had 35 pressure ports distributed chordwise: 19 upper surface and 16 lower surface at the inboard slotted section centerline, and 35 pressure ports - 18 upper and 17 lower - at the outboard section. Data were recorded at each Mach number and angle-of-attack combination for each model configuration. Direct comparison plots of C_p versus chord station for each model configuration were made for each Mach number and angle of attack. These comparative pressure plots were nearly identical overlays and the slight difference is attributable to run repeatability and/or small differences in test Mach number. The test results (see Figures 2 and 3) show very conclusively that sectionalized flutter model design is aerodynamically accurate when testing in the transonic speed range. (See Reference 3).

Once these tests were completed and the results were satisfactory, the test program that is described in this paper was undertaken.

TEST PLAN

The test plan was to conduct an extensive multipurpose aeroelastic investigation of an advanced-technology supercritical airfoil and a conventional airfoil, both of a transport-type wing in the high subsonic and transonic speed range.

Certain aerodynamic and structural conditions have been questioned with regard to their effect on flutter. Probably the two most prominent in this category are the effects of Reynolds number and wing deformation or angle of attack on the aeroelastic stability. Now that the supercritical airfoil has made its debut on the flutter scene, these and other effects that may increase the sensitivity of the supercritical airfoil to flutter over the more conventional airfoils are even more paramount. Another aerodynamic condition, and one that should not be considered of lesser importance than the first two, is the unsteady oscillatory aerodynamic effects on flutter behavior by the interaction between the steady and unsteady flow fields through the periodic motion of the shock waves.

These three flutter aerodynamic effects - Reynolds number, deformation and unsteady oscillatory aerodynamics - are the objectives of this aeroelastic investigation, involving important comparisons between the conventional and supercritical airfoil.

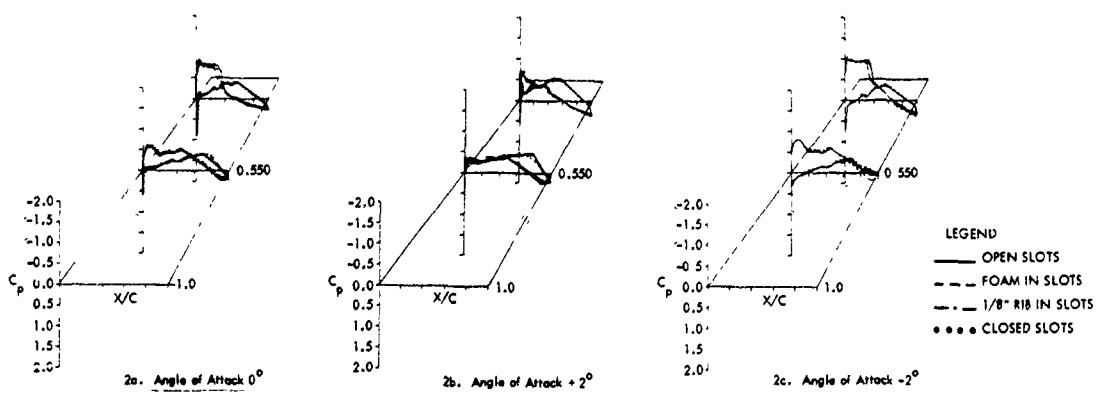

Figure 2. Slotted Model Pressure Distribution Overlap Mach 0.95

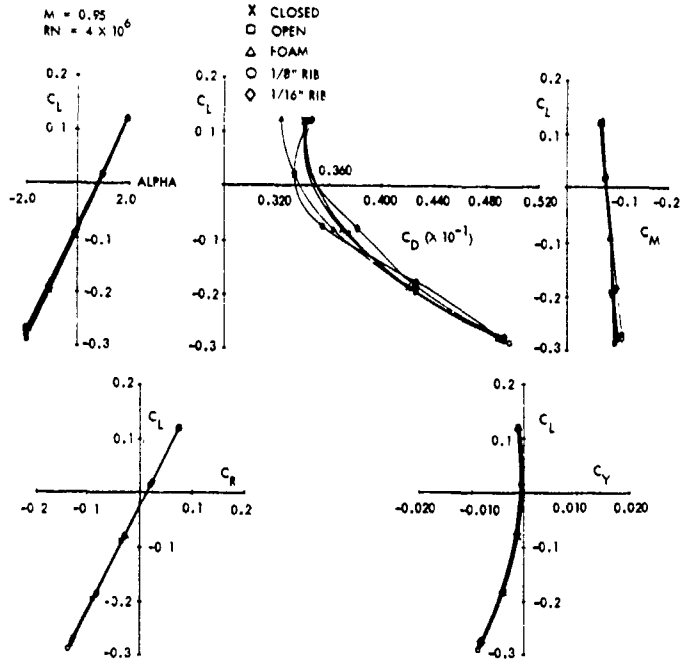

Figure 3. Slotted Wing Root Loading Aerodynamic Coefficients

MODEL DESIGN

A typical advanced transport wing with two pylon-mounted engines was chosen as the test model (see Figure 4). The model design and scaling are shown in Figure 5. The model was a cantilevered wing mounted to the tunnel balance system with a half-body root fairing. Two airfoil configurations were picked: one design, referred to in this paper as a conventional airfoil, was a "peaky" type airfoil that is a forerunner of today's advanced supercritical airfoil and has been in use for the past 15 years; and the other is an advanced highly aft loaded airfoil that is 25% thicker, non-dimensionally for the same cruise speed at a lift coefficient 15% higher than the peaky airfoil (see Figure 6). Both airfoils have the same planform geometry, and the same two wing pylon-mounted engines. The wing section mass properties were easily duplicated and checked. The wing stiffnesses were the same for both models since, with the use of the sectionalized model design, one spar was used with both models. Another spar was built four times stiffer than the first, thus giving four times the test dynamic pressures at flutter and four times the Reynolds number.

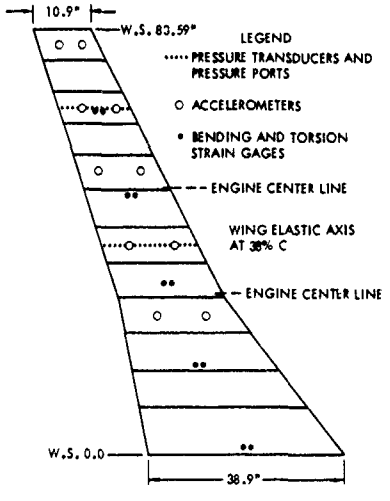

Figure 4. Aeroelastic Model Wing Planform and Instrumentation Layout

	SPAR #3 0.50% NOMINAL STIFFNESS	SPAR #4 0.125% NOMINAL STIFFNESS	SPAR #3 / SPAR #4
GEOMETRY b_m/b_o	1/12	1/12	1
VELOCITY V_m / V_o	1/2.02	1/2.02	1
$V/b\ \omega_m / V/b\omega_o$	1.4	2.83	1/2
MACH	1	1	1
VIRTUAL MASS RATIO μ_m / μ_o	1.96	8.00	1/4
DENSITY ρ_m / ρ_o	1.2	1.2	1
ρ AIR / ρ FREON	1.633	6.667	1/4
FREQUENCY ω_m / ω_o	4.24	2.10	2
DEFLECTION $\delta_m / b_m / \delta_o / b_o$	0.6665	2.721	1/4
DYNAMIC PRESSURE $q_m\ q_o$	0.150	0.037	4
WEIGHT W_m / W_o	1/1,440	1/1,440	1
UNBALANCE S_m / S_o	1/17,280	1/17,280	1
INERTIA I_m / I_o	1/207,360	1/207,360	1
STIFFNESS EI_m / EI_o	1/138,205	1/546,016	1/4
REYNOLDS NO Re_m / Re_o	1/29.905	1/122.06	1/4

SUBSCRIPTS m = MODEL, o = AIRPLANE

SPAR #2 (NOMINAL STIFFNESS) AND SPAR #1 (1.5 NOMINAL STIFFNESS) WERE PLANNED BUT NOT COMPLETED.

ASPECT RATIO 8.0

SUPERCRITICAL ROOT t/c = 0.152
BREAK t/c = 0.14
TIP t/c = 0.127

Figure 5. Aeroelastic Model Scaling

Figure 6. Model Airfoil Profiles for Instrumented Pressure Sections

The model angle of attack was changed remotely through operation of the tunnel turntable with planned test excursions of -2°, 0°, and $+1\text{-}1/2^{\circ}$. The wing had a root incidence of $+4^{\circ}$, which was considered the 0° flight position.

The wing was sectionalized with 12 sections made of balsa covered with fiberglass and attached to a solid aluminum spar at the section center bridge system. (see Figure 7). The model spar was built to the jig position of 4° root to tip.

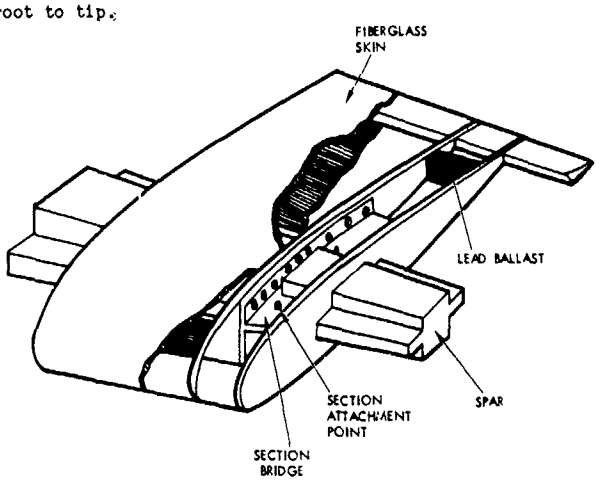

Figure 7. Typical Wing Section Construction

The wing planform and instrumentation layout are shown in Figure 4. The elastic axis inboard of the break had a sweep angle of 29.4°, and outboard of the break 23.75°. The two engines were mounted on pylons suspended beneath the wing at 38% and 63% of the wing semispan. The wing was mass-balanced to represent approximately 30% fuel to obtain the desired flutter mode. Some of the fuel mass was used for strengthening the wing sections to carry the higher wing loads during angle of attack studies. Figure 8 shows the model mounted in the tunnel with normal engine design and Figure 9 shows the model with the dummy engines.

Figure 8. Aeroelastic Model with Normal Engine Design

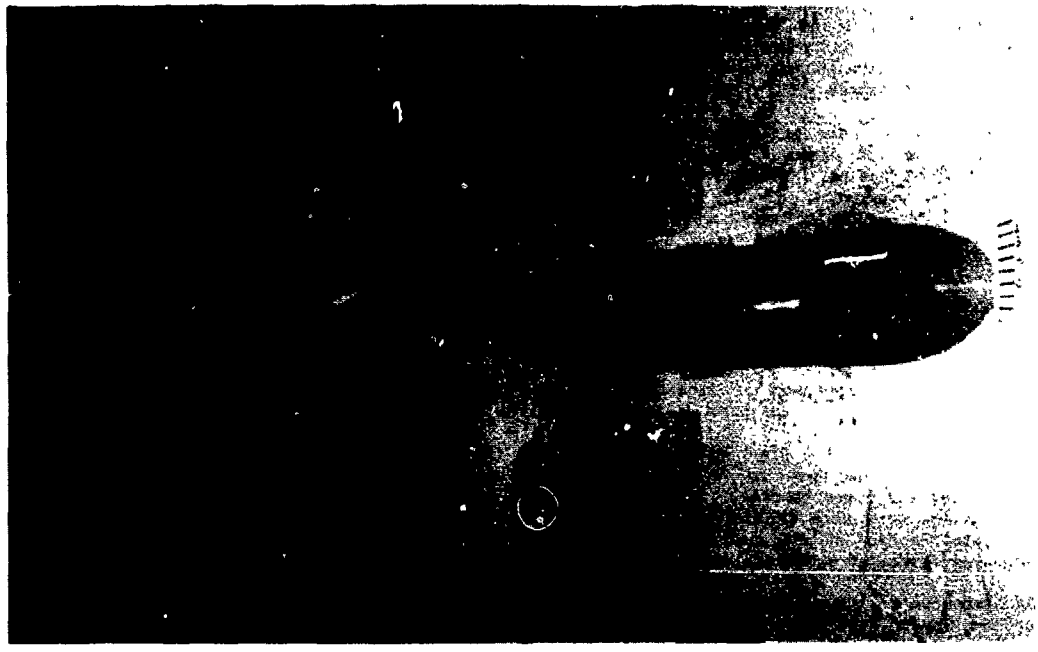

Figure 9. Aeroelastic Model with Dummy Engines Installed

The ground vibration tests for both test configurations - the conventional and supercritical airfoil - were identical in modal response and frequencies, verifying the structural similarity. Figure 10 compares the frequencies of the analysis and the model with the #4 spar (minimum stiffness design).

STIFFNESS SPAR #4
SUPERCRITICAL WING SECTIONS

TEST (Hz)	ANAL.	% DIFF.	DESCRIPTION
2.1	2.12	-	1ST BENDING
5.	5.01	-	1ST TORSION, 2ND BENDING
5.73	5.77	-	1ST FORE AND AFT BENDING
8.77	8.33	5.0	2ND BENDING, 1ST TORSION
11.69	11.67	-	2ND TORSION
14.76	13.7	7.3	3RD BENDING
16.7	16.73	-	IB ENG

Figure 10. Vibration Analysis Frequency Comparison

MODEL INSTRUMENTATION

Since the test plan was to record steady and unsteady aerodynamic pressures, two of the model sections were instrumented with surface pressure transducers and ports. Wing sections 6 and 9 were selected as the instrumented sections, 49.6% and 82% of the wing span, respectively. The pressure measuring sensors and ports were chordwise along the section centerline, and between the section center bridge ribs that attached the section to the spar. Each section had 39 pressure ports, 19 upper and 19 lower surface, with one on the leading edge. Each section also had 8 pressure transducers, 4 upper and 4 lower surface, to be used as reference and correlation with the scani-valve pressures.

The wing spar had bending and torsion strain gages located at the root, 20%, 40%, 60%, and 80% span; accelerometers were located at approximately 25% and 75% chord at 20%, 40%, 60%, 80%, and 95% span. The strain gages and accelerometers defined the static and dynamic motion of the wing. The wing was mounted to the tunnel side wall through the balance system to measure lift, drag, and other total wing behavior.

Instrumentation Calibration

All of the model instrumentation was calibrated prior to wind tunnel testing and recalibrated and recorded on the test magnetic tapes after installation.

Strain Gages - The bending and torsion strain gages were calibrated by applying loads and torques to each spar and recording the resultant outputs in mv/lb in.

Scani-Valves Transducers - Eight scani-valves were used during the test. The scani-valves were ganged in groups of four - one set to measure pressure of the inboard test section and one set to measure the outboard instrumented section. Each scani-valve measured one half of the section chord. All of the scani-valve transducers were calibrated and certified in the NASA calibration laboratory for several static pressures with their outputs recorded in mv/psi.

Pressure Ports - The pressure port orifices were connected to the scani-valve transducers using 0.043-inch ID temflex tubing. Each outboard section port used 9-foot tubing and each inboard section port used 7-foot tubing. Each port was referenced to the tunnel static pressure by a common source located in the wing root fairing. The system was checked for tube blockage or leaks by applying several static pressures to each port with their outputs being recorded.

A wind-off dynamic pressure calibration of the tubes and scani-valve pressure transducers was performed. The calibrator consisted of a pneumatic cylinder driven by an electromagnetic shaker and a tube from the cylinder to be fitted over each pressure port. As the oscillation frequency of the shaker was varied, the signals from the scani-valve pressure transducer and the calibrated pressure transducer in the cylinder were analyzed using a frequency-response analyzer. The magnitude and phase of the scani-valve relative to the cylinder pressure were expressed at several static pressure levels. The wind-on dynamic pressures of each port were adjusted in phase and magnitude to agree with the pressure transducers along the chord in a manner similar to the method described in Reference 4.

Pressure Transducers - Eight pressure transducers (Endeveco piezoresistive, differential pressure transducers with thread mounting) were used for each instrumented section; four along the upper surface and four along the lower surface. Each transducer was referenced to the tunnel static pressure. The pressure transducers were calibrated with the same tube calibrator as the pressure ports. Pressure response was recorded at one static pressure and at an oscillatory pressure at 10 Hz, which was near the expected flutter frequency.

Accelerometers - All accelerometers were calibrated in mv/g in the calibration laboratory. Phasing was checked for correct installation during the ground vibration test.

Balance Instrumentation - Sensitivity factors were determined from laboratory tests and checked after model installation by applying known loads to the model.

Model Angle of Attack - The model root angle of attack was obtained by visually setting the model pitch angle by marks on the tunnel wall and more accurately by recording the output from an angular accelerometer calibrated by using an inclinometer.

TEST RESULTS - FLUTTER

The test was outlined primarily to determine the flutter characteristics at transonic speeds including affects of angle of attack and Reynolds number of a supercritical airfoil and a conventional airfoil; the secondary test objective was to measure steady and unsteady aerodynamic behavior as flutter was approached.

In an approach to save the expensively instrumented pressure sections, the initial model configuration was selected as the supercritical airfoil with regular sections replacing the instrumented sections, and the less stiff spar affording the best opportunity of obtaining flutter at the lowest dynamic pressure.

Unfortunately, this conservative desire to approach the first flutter point as safely as possible may have been unwise and cost some valuable test time. The first test runs were made at very low tunnel dynamic pressures (below 40 psf) by increasing q and Mach number along a constant tunnel total head pressure line. At these low q's, the model behaved very erratic, and although appearing to be near flutter - it was beating in several modes - the sweeps were stopped at 0.9 Mach number. It was thought that, by observing a minimum damping in the predicted flutter mode by going under the flutter boundary, the critical Mach number could be determined and a safer approach to flutter at higher q's could be made. However, in this q range this didn't seem conclusive. Several questions were raised at this time; one, did the model have sufficient aerodynamic flow transition point; and two, did the large engines (aerodynamically blow-through) cause unrealistic aerodynamic forces coupling with the wing modes. To eliminate these questions, a strip of #46 grit, 0.10 inch wide, was added along the wing at 10% chord on the upper and lower surfaces, and the engines were replaced with dummy engines that represented the mass properties (except roll inertia) but with minimum aerodynamic effectiveness (see Figure 9). After the initial runs it also seemed apparent that violent flutter would not occur and it would be reasonably safe to install the instrumented sections and continue the test.

With these changes, the tunnel pressure was increased to represent higher dynamic pressures, and at a constant tunnel head pressure, the q and Mach number were increased until flutter was reached. This procedure was repeated for several higher and lower tunnel pressure lines until the flutter boundary for the supercritical airfoil was plotted (see Figure 11).

Angle of Attack Tests

Although two noteworthy conditions were observed during this portion of the test program, no explanations are offered at this time as to the probable cause. At several of the flutter points with the wing at 0° Fuselage Reference Line (wing root incidence $+4^{\circ}$), the test conditions of Mach and q were backed off, the angle of attack of the wing root was increased to $+1\text{-}1/2^{\circ}$ and subsequently decreased to -2°. For both angle-of-attack settings, the Mach and q were increased to or above the previous flutter point, and in both incidences the flutter mode was higher damped and flutter was not obtained for either the plus or the minus angle-of-attack settings. This same phenomenon occurred when the conventional airfoil was tested. It should be noted that the wingtip deformed under load and did not necessarily change the same as the root.

The second interesting phenomenon that occurred with the supercritical airfoil was a subflutter low-damped boundary. It was observed that, during each sweep up a constant pressure line, a very low damped, almost neutrally stable area was passed through. The low damped mode had the same frequency, and by visual comparison the same mode shape that eventually fluttered, the low damped boundary paralleled the flutter boundary but at a considerably lower Mach number. This low damped boundary was reasonably narrow and once through it the flutter mode became heavily damped until the true flutter boundary was approached. Figure 12, an online response of amplitude versus frequency plot, shows this condition occurring at approximately Mach 0.75 at 9.75 Hz. It is interesting to note on Figure 12 that the 11 Hz mode does not indicate the same subflutter, low damping as the 9.75 Hz mode. It appears that each mode may have its own flutter characteristics since the 9.75 Hz mode is outer wing bending and the 11 Hz mode is outer wing torsion.

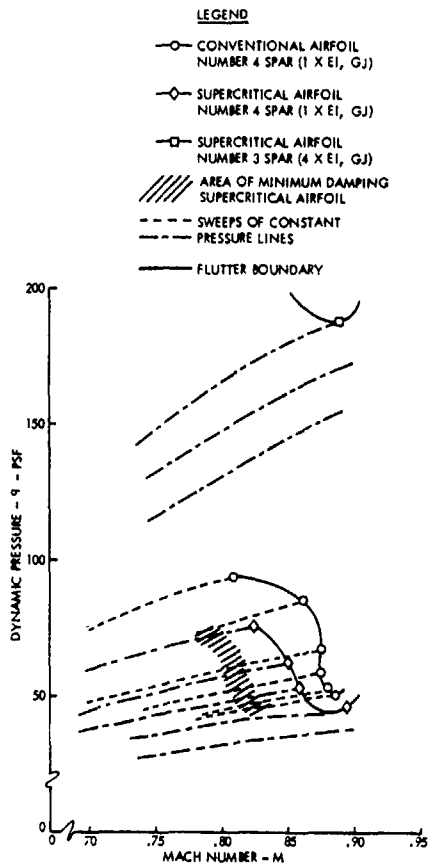

Figure 11. Flutter Boundaries for Supercritical Airfoil vs. Conventional Airfoil

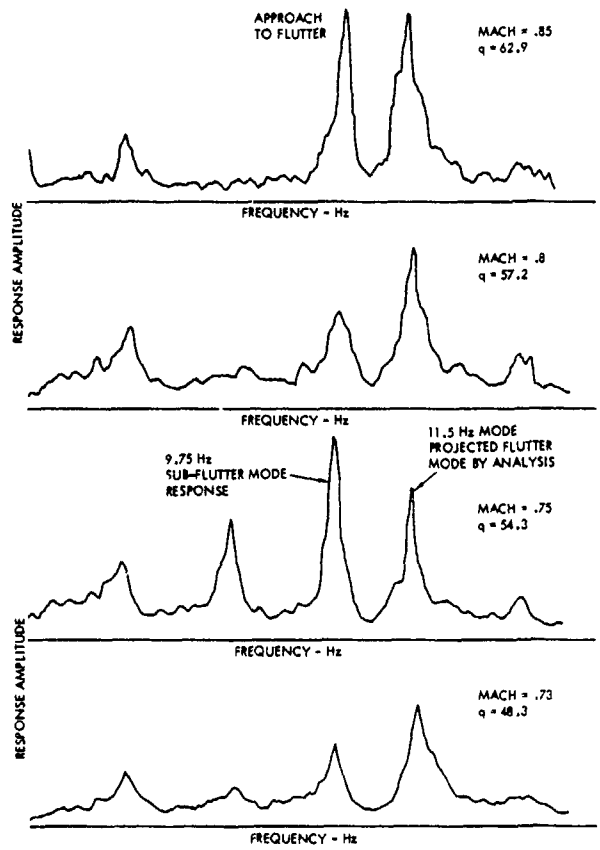

Figure 12. Approach to Flutter Response Amplitude for Two Modes Showing Subflutter Minimum Damping Prior to Flutter

Unlike the angle-of-attack flutter similarity between the supercritical and conventional airfoils, the low damped boundary observed with the supercritical airfoil did not occur with the conventional airfoil.

The flutter boundary for the conventional airfoil was obtained using the same test technique used for the supercritical airfoil.

The test to this point had been conducted for both airfoils using the same spar and stiffnesses. Figure 11 shows the flutter boundary for each airfoil. These boundaries, although showing different severity, did represent the same flutter mode shape and frequency.

Reynolds Number Tests - The following test objective was to investigate the effect of Reynolds number on flutter. The plan called for testing a stiffer spar causing the flutter boundary to occur at higher dynamic pressures, and thus higher Reynolds number. The stiffnesses of Spar #3 were increased by a factor of four uniformly over Spar #4 stiffnesses used in the initial tests. This would give a Reynolds number four times greater, which was considered the maximum practical dynamic pressure at which this type of model construction could safely be tested.

Constant pressure sweeps were made for increasing pressures in an attempt to locate the bottom of the flutter boundary. After the first sweep, it was observed that minimum damping occurred at the same Mach number as the first spar tests. The sweeps were terminated at Mach 0.90 after minimum damping was passed. When the pressure sweep line was tested where flutter was expected but did not appear, it was observed that the engines were responding violently laterally at 18 Hz just below the wing flutter mode of 20 Hz. It was decided to make an even higher tunnel pressure sweep in an attempt to make the wing flutter, but again the engine lateral vibrations seemed to kill the wing flutter mode, which at this

point was very strong. The dummy engines were like a blade and had considerable aerodynamic lateral lift, so much in fact that the engines were almost at flutter. To eliminate this engine/wing coupling the engine fairings were greatly cutaway minimizing the flat aerodynamic surface. Again, a pressure sweep was made below the anticipated flutter point, and this time the wing flutter mode was clean and passed through a minimum damping at approximately Mach number 0.88 with little interference from the engine mode. The third pressure line sweep netted flutter at the same Mach number as with the previous spar and at a q four times higher, indicating little or no Reynolds number effect.

Before the discussion of flutter is left, some comment should be made about the flutter characteristics of the cantilevered wing; conventional and supercritical airfoils both exhibited the same aeroelastic modal response, frequency, and mode shape, and both exhibited two flutter modes. Prior to mass-balancing the model, a preliminary flutter analysis parametric study had been conducted. A flutter condition was desirable that had an attainable flutter speed - not too violent or conversely not too shallow an approach to flutter and with little coupling with other modes. From this analysis, a wing fuel loading of 30% was chosen which demonstrated a clean, moderate flutter behavior with a flutter frequency of 11 Hz. During the model tests, the 11 Hz mode which was primarily outer wing torsion with inner wing bending became the predominate mode. As the Mach and q were increased and flutter seemed eminent in the 11 Hz mode, a slightly lower frequency mode, 9.75 Hz, which was mostly a third bending-torsion mode (that proved less desirable for recording unsteady pressure measurements since the outer node line was near the outer instrumented section center chordline) became rapidly less damped and in every case fluttered before the higher frequency predicted flutter mode (see Figure 12). Subsequent to the test, further analysis has been conducted and as shown in Figure 13, the two flutter modes cross at very nearly the same wing fuel loading. It was concluded that the test objectives could be accomplished with the 9.75 Hz flutter mode. In a future test, it will be interesting to obtain similar data with the 11 Hz flutter modes by using a lower fuel loading.

TEST RESULTS - STEADY STATE AERODYNAMICS

Figure 14 is a map of the test points that are presented in this paper. They were chosen from the many steady state pressure measurements that were recorded as a good cross-section of the test data. Several of the test points show pressure distributions for the -2°, 0°, and $+1\text{-}1/2^{\circ}$ wing root angle of attack conditions. The flutter boundaries are included in Figure 14 for reference to location of pressure data presented. Each pressure point on Figure 14 gives the plot number and root angle of attack [examples 5 (4.12°) and 11 (1.963°)]. The scani-valve steady pressure data for the forward 50% chord lower surface inboard section was not reduced initially due to online computer problems but will be reduced later.

The steady state pressure plots are grouped in Figure 15 for all the conventional airfoil pressure distributions and in Figure 16 for all the supercritical data.

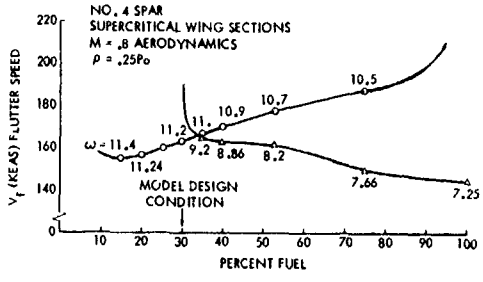

Figure 13. Flutter Analysis Subsequent to Test

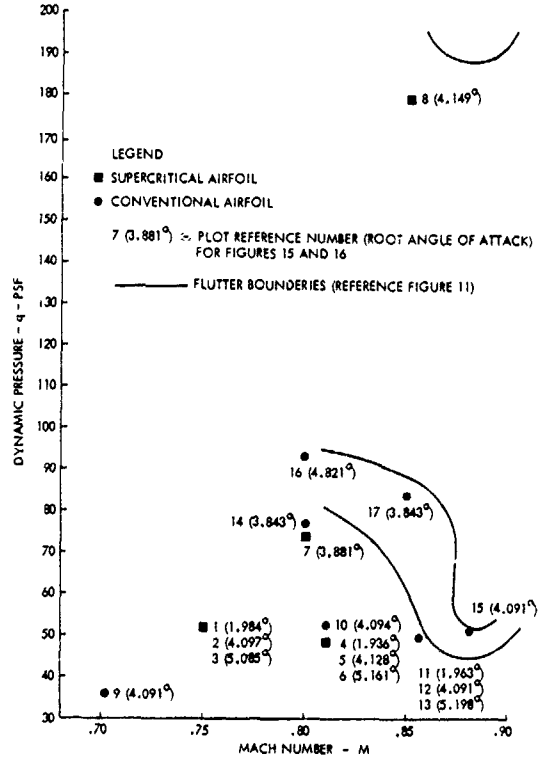

Figure 14. Conditions Presented for Steady State Aerodynamic Pressure Plot Comparisons

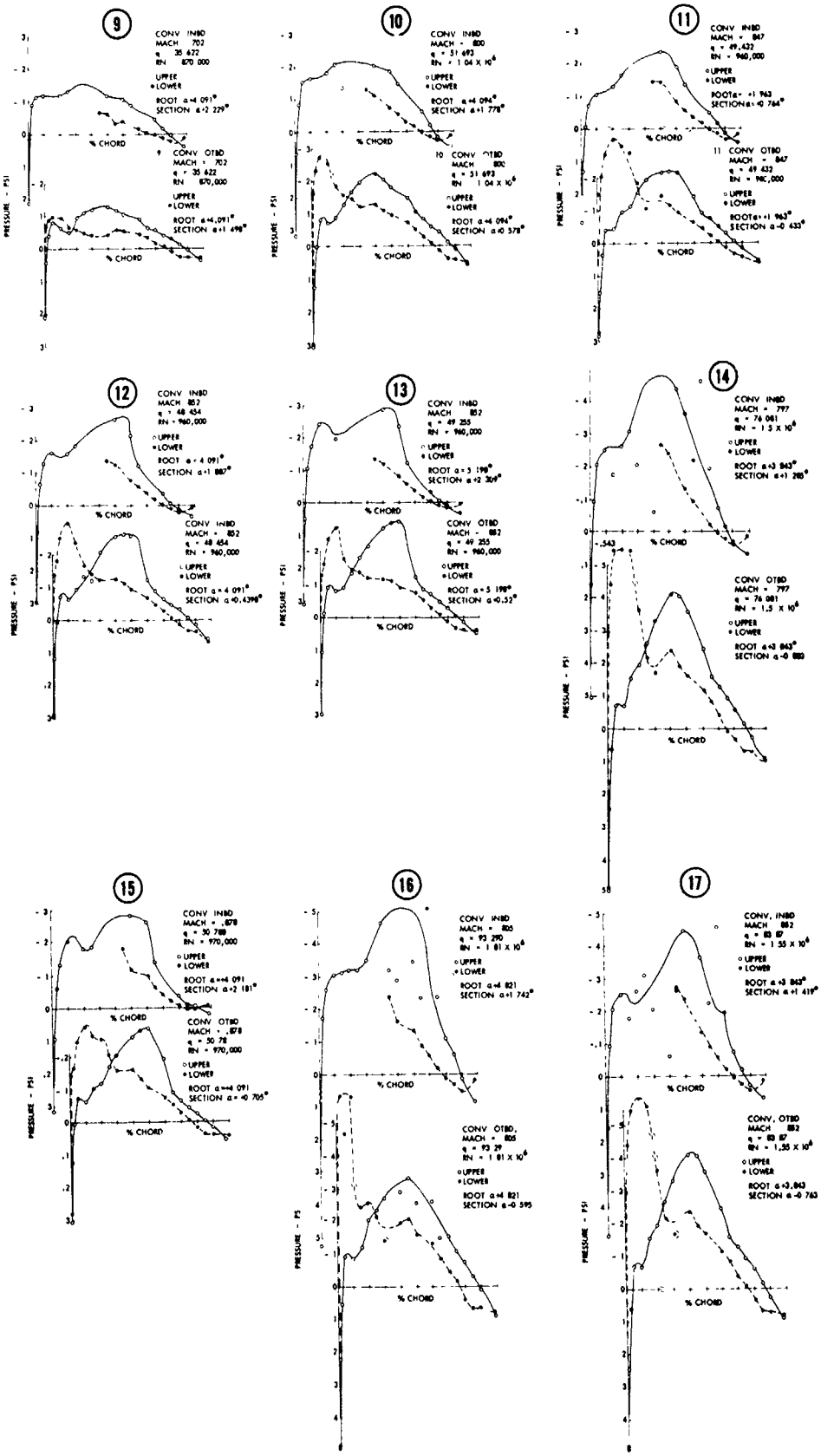

Figure 15. Conventional Airfoil Steady State Aerodynamic Pressure Distribution

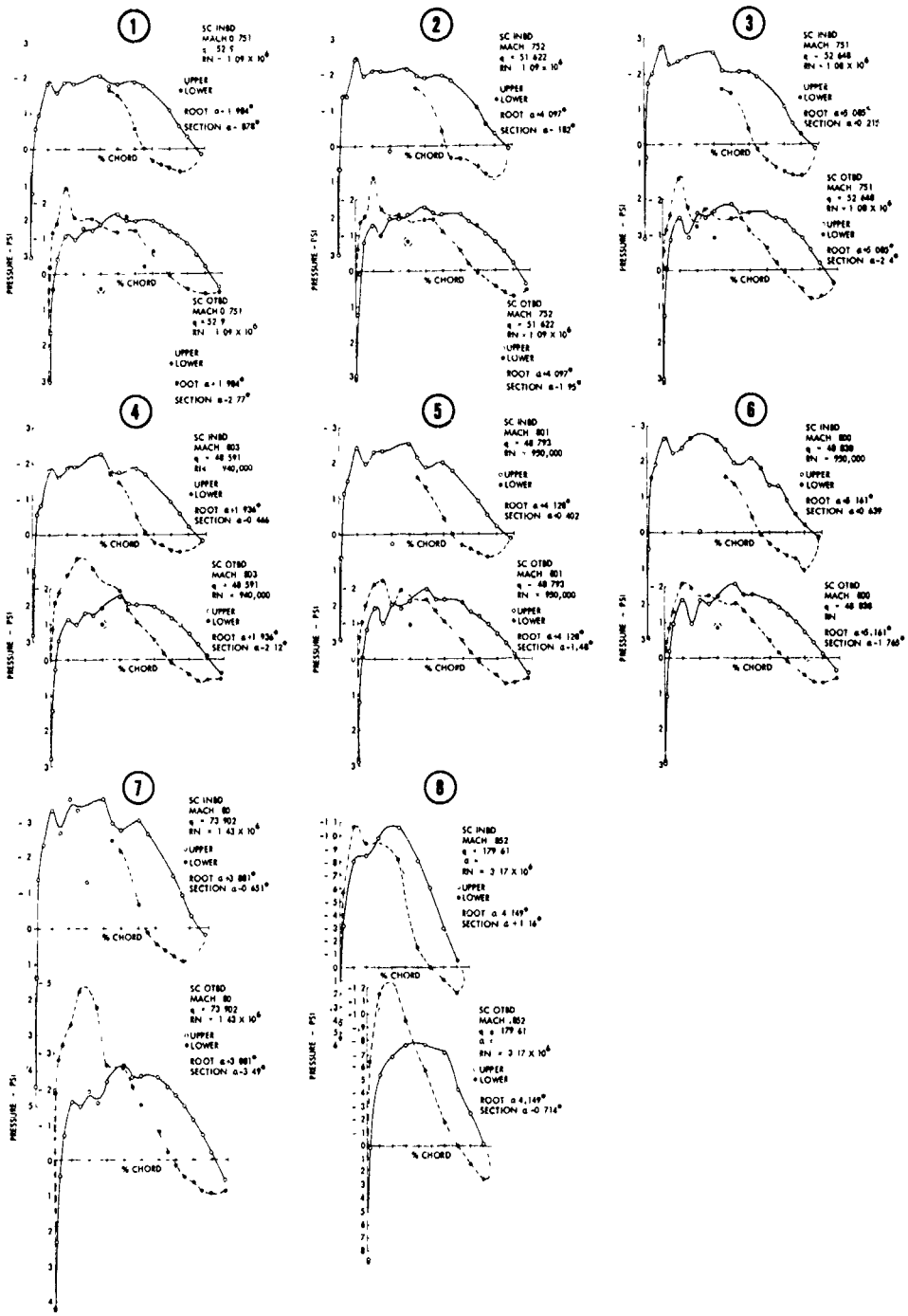

Figure 16. Supercritical Airfoil Steady State Aerodynamic Pressure Distribution

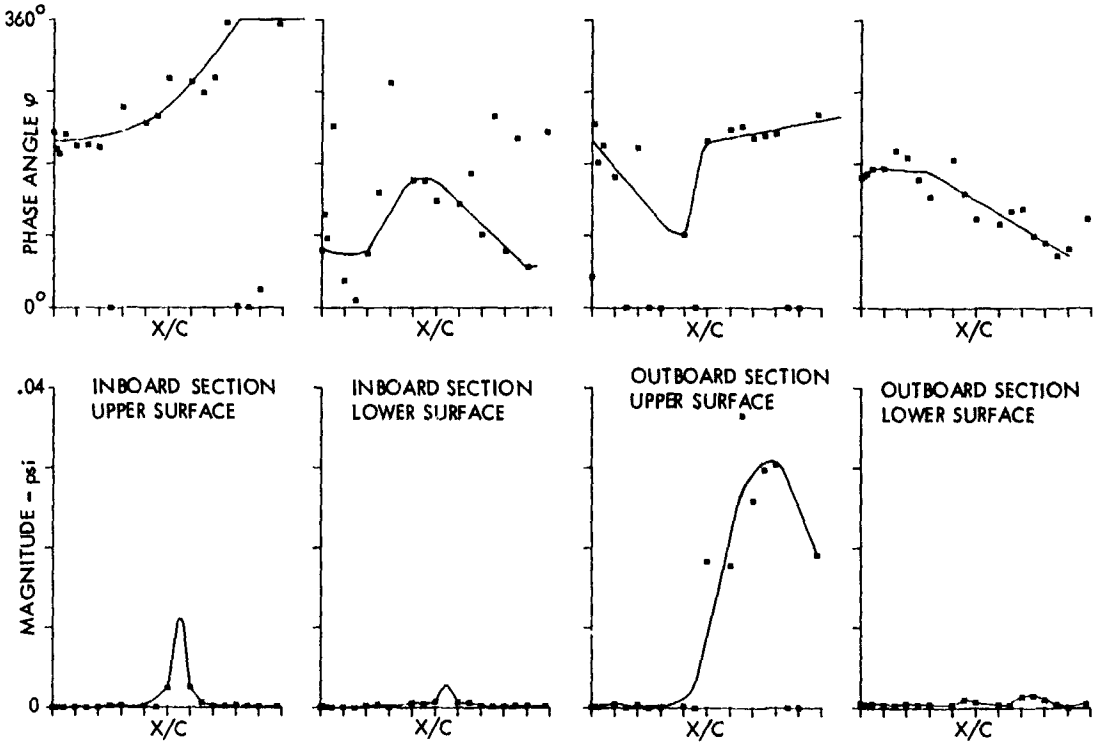

Figure 17. Conventional Airfoil Unsteady Pressure Distribution, Mach. No. 0.852, q = 83.87 psf.

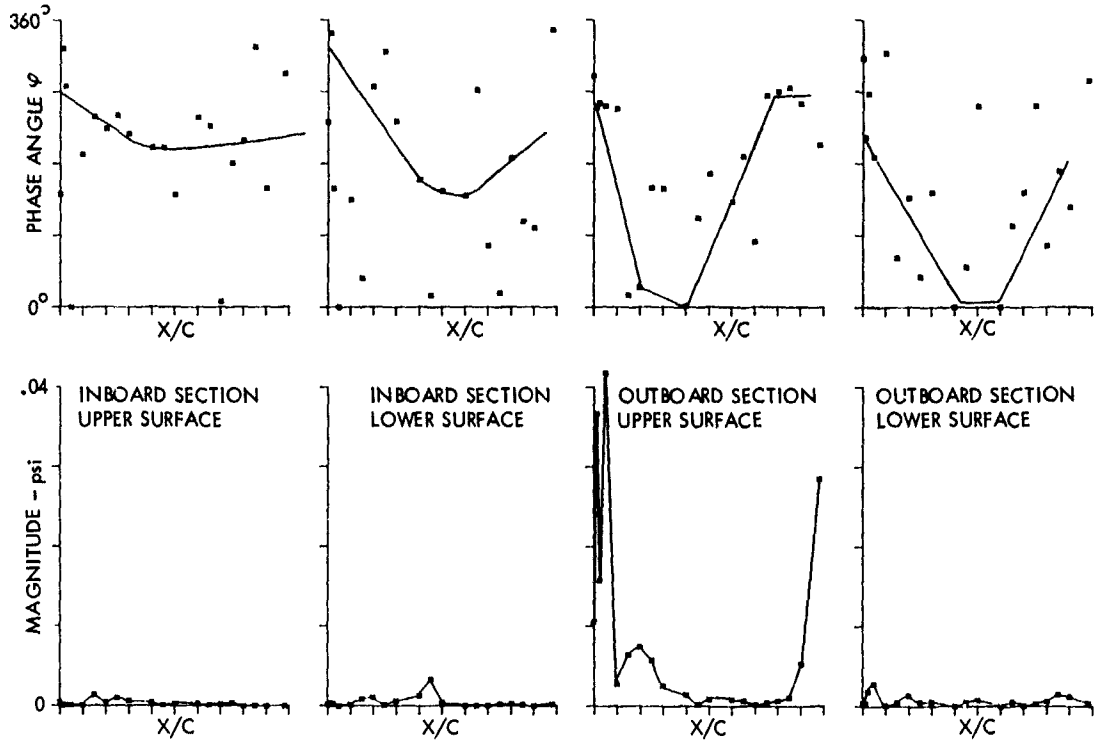

Figure 18. Supercritical Airfoil Unsteady Pressure Distribution, Mach. No. = 0.80, q = 73.902 psf.

Each pressure plot gives the plot number, airfoil, Mach number, dynamic pressure, Reynolds number, root angle of attack and inboard or outboard test section angle of attack with reference to the tunnel.

The test sections' true angles of attack were determined from the bending and torsion strain gage data at each of five spanwise locations. A corresponding set of applied loads was derived and the deflections and twists then determined from simple beam theory using experimentally verified stiffness data.

TEST RESULTS - UNSTEADY AERODYNAMICS

Data Reduction

Four 14-channel tape recorders were used to store the pressure and load information in real time. Typically, each recorder had one of the four sets of pressure transducers, the accelerometers associated with them, and the two associated scani-valves. The remaining tape channels on each recorder were used for the other accelerometers and strain gage information necessary for the calculation of the airfoil twist.

To analyze this information, a HP5451C Fourier Analysis System with a 64-channel multiplexer was used. Twelve channels were sampled simultaneously, with the system being triggered on the first scani-valve step. This procedure provided assurance that the proper time relation between sensors was preserved. The computer then contained a collection of time histories, each of which represent one second of information, made up of 1024 points. This time interval gives approximately 10 cycles of data at the flutter frequency.

Once these time histories were stored on the mass storage device, calibration factors were applied and the data were digitally filtered. The time history is Fourier transformed into the frequency domain. Then, all the Fourier components except in the frequency band of interest are cleared. At this point the operator is free to retransform the data back into the time domain or to leave it where it is, depending on the type of presentation to be used.

Data Presentation

Two different presentations are used: a frequency domain and a time domain. The frequency presentation gives phase and amplitude with respect to a reference versus chordwise position (see Figure 17 conventional airfoil, and Figure 18 supercritical airfoil).

The time domain presentation is somewhat more complex, since the program uses the filtered time history. At some point in the time history, the program reads the frequency and amplitude, and continues to do so at predetermined intervals for one complete cycle. The values are then plotted as vectors for the appropriate pressure distribution. The plots are at 15-degree intervals during one cycle (see Figure 19 conventional airfoil and Figure 20 supercritical airfoil). The reference chord (25 to 75% C) shown at each 15-degree interval represents the pitch and plunge of the instrumented test sections at that time frame. The unsteady pressure data were recorded during dynamic response of the wing, excited by tunnel turbulence, as flutter was approached.

COMMENTS

There are several results from this test where the authors have not attempted to draw any conclusions. It is the objective that as these data are studied and analytical correlations made that a better understanding will be had regarding the subflutter low damping boundary and the flutter speed increases observed with both positive and negative changes in angle of attack.

Future tests investigating various flutter modes, stiffness and mass distributions, and store locations will be of great importance in studying flutter characteristics for the developing new airfoils. The use of surface-mounted pressure transducers exclusively in lieu of a mixture between transducers and pressure ports will be important in obtaining steady and unsteady aerodynamic pressures simultaneously for all locations up to and including flutter. This will greatly reduce the data reduction errors associated with tube length, phasing and attenuation and data compared at different cycles.

REFERENCES

1. Farmer, M. G. and Hanson, P. W., "Comparison of Supercritical and Conventional Wing Flutter Characteristics," Proc. AIAA/ASME/SAE 17th Structures, Structural Dynamic and Materials Conf., 1976.

2. Houwink, R., Kraan, A. N., Zwaan, R. J., "Characteristics of a Supercritical Wing," Presented at the AIAA/ASME/ASCE/AHS 22nd Structures, Structural Dynamics, and Materials Conf., April 1981.

3. Grosser, W. F., "A Wind-Tunnel Study of the Aerodynamic Characteristics of a Slotted Versus Smooth-Skin Supercritical Wing," Presented at the AIAA/ASME/ASCE/AHS 23rd Structures, Structural Dynamics and Materials Conf., May 1982.

4. Tijdeman, H., "Investigation of the Transonic Flow Around Oscillating Airfoils," NLR TR 77090U (1977).

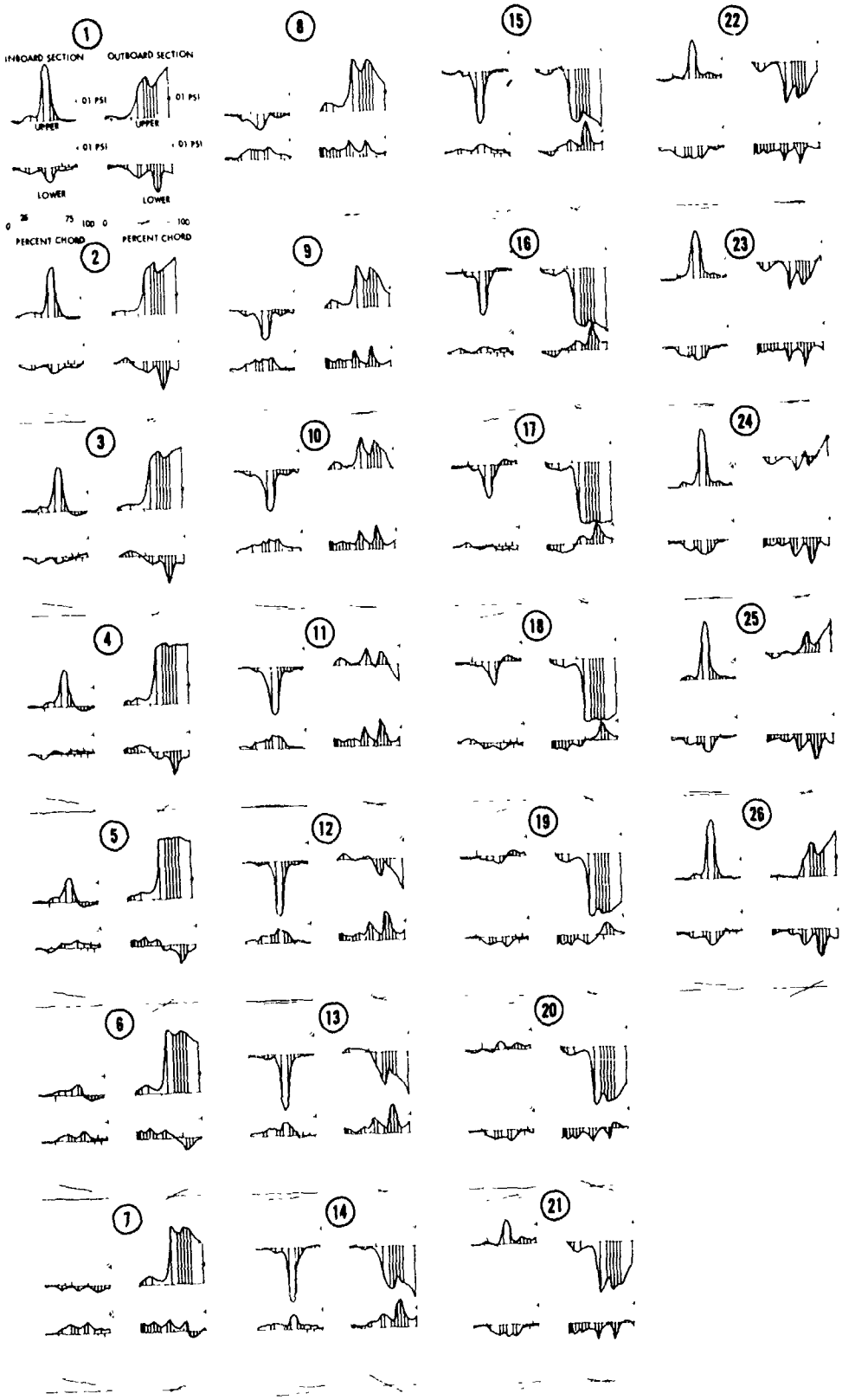

Figure 19. Conventional Airfoil Unsteady Aerodynamic Pressure Distribution, Mach No. = 0.852, q = 83.87 psf.

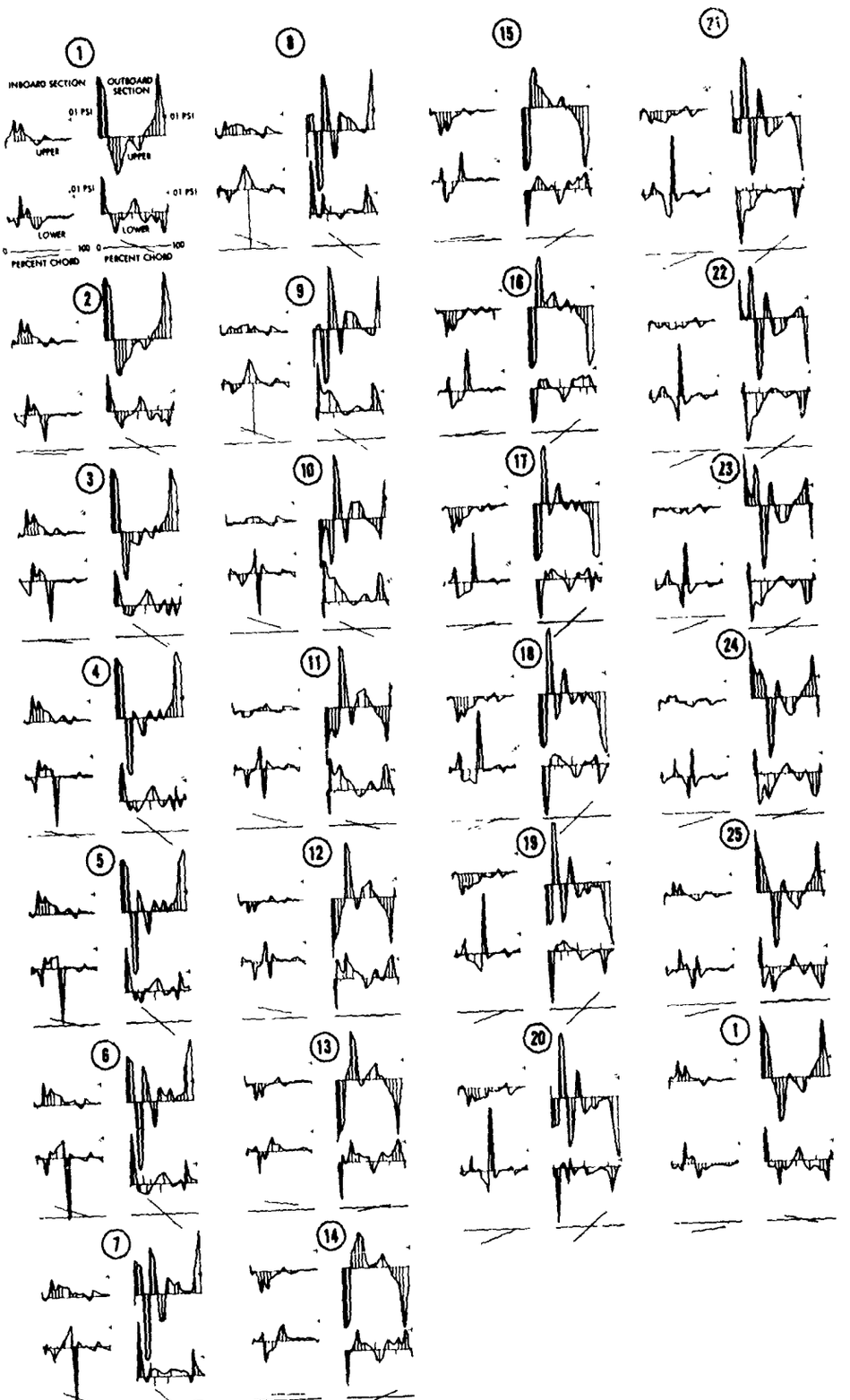

Figure 20. Supercritical Airfoil Unsteady Aerodynamic Pressure Distribution, Mach No. = 0.80, q = 73.902 psf.

ADAPTIVE FLUTTER SUPPRESSION - ANALYSIS AND TEST

by
E.H. Johnson, C. Hwang and D.S. Joshi
Northrop Corporation, Aircraft Division
One Northrop Avenue
Hawthorne, California 90250, USA

C.A. Harvey
Honeywell, Incorporated
Systems and Research Center
2600 Ridgway Parkway
Minneapolis, Minnesota 55413, USA

L.T. Huttsell
Flight Dynamics Laboratory
Air Force Wright Aeronautical Laboratories
Wright-Patterson Air Force Base
Ohio 45433, USA

M.G. Farmer
NASA Langley Research Center
Hampton, Virginia 23665, USA

SUMMARY

Methods of adaptive control have been applied to suppress a potentially violent flutter condition of a half-span model of a lightweight fighter aircraft. This marked the confluence of several technologies with active flutter suppression, digital control and adaptive control theory the primary contributors. The control algorithm was required to adapt both to slowly varying changes, corresponding to changes in the flight condition or fuel loading and to rapid changes, corresponding to a store release or the transition from a stable to an unstable flight condition. The development of the adaptive control methods was followed by a simulation and checkout of the complete system and a wind tunnel demonstration. As part of the test, a store was released from the model wing tip, transforming the model abruptly from a stable configuration to a violent flutter condition. The adaptive algorithm recognized the unstable nature of the resulting configuration and implemented a stabilizing control law in a fraction of a second. The algorithm was also shown to provide system stability over a range of wind tunnel Mach numbers and dynamic pressures.

INTRODUCTION

Active flutter suppression has long been regarded as a means of avoiding flutter placards of high performance aircraft when they are carrying stores. Research in this area has progressed from analytical studies to wind tunnel tests (Ref. 1-2) and limited flight tests. This research has led to a high degree of confidence in the methods and the hardware used in this technology. The work reported on in this paper extends this technology in two important ways: 1) It uses a digital control system rather than the analog systems used in most previous programs, and 2) it applies methods of adaptive control theory to the active flutter suppression task.

The use of a digital computer to perform the control task is in line with the general transition of aircraft control systems from analog to digital devices. The flexibility and complexity available from the digital computer make it an attractive choice for any control application. Adaptive control, with its requirements for decision-making and iterative parameter estimate calculations, makes digital control a virtual necessity. The work performed to effect the digital implementation has been reported on previously in References 3 and 4. These references describe the computer system used, the techniques used to digitize the control laws and presents the results of a November 1981 wind tunnel entry that tested non-adaptive digital control laws. This report stresses the adaptive aspects of the program with the digital aspects mentioned only as required.

The primary motivation for investigating adaptive control is that the multiplicity of stores that a modern fighter aircraft carries in numerous combinations makes it impossible to anticipate and correct for all potential flutter instabilities with a fixed control system. The ultimate requirement of the adaptive system is that it be able to accommodate any of these instabilities with a minimal foreknowledge of the store condition. A secondary motivation is that non-adaptive control laws can suffer from a lack of adequate gain and phase margin at flight conditions different from those at which they were designed. An adaptive system should be able to enhance these margins and thereby expand the aircraft's flight envelope.

Before proceeding further, it is desirable to define what is meant by adaptive control in the context of this paper. One could think of there being a continuum of levels of non-adaptive and adaptive control. The highest, i.e., the most demanding, level of non-adaptive control would entail gain scheduling wherein the control law is designed to be a function of air data parameters and the aircraft configuration. The first level of adaptive control is defined to be detection and discrimination. At this level, the digital computer is called upon to determine, based on response information, whether one

of several specified conditions exists. If a flutter condition is detected, a control law is engaged to suppress it.

At the second level of adaptive control, it is assumed that the parameters of the flutter condition are not known exactly and input/output data are to be processed to provide estimates that result in an improved ability to control the flutter condition.

At a final level of adaptability, the system would be asked to not only identify the flutter condition, but also to construct an appropriate control law to suppress it with no foreknowledge of its nature

The work performed in the program discussed here limited itself to the first two levels of adaptation. It is felt that the third level exceeds the capability of current off-the-shelf computers and possibly the capability of adaptive algorithms.

The work described in this paper was performed under contract for the United States Air Force Wright Aeronautical Laboratories under a contract entitled, "Test Demonstration of Digital Adaptive Control of Wing/Store Flutter." The work was performed by a Northrop/Honeywell team in which Northrop, as the prime contractor, contributed its capability in active flutter suppression (References 1 and 2) while Honeywell, acting as a subcontractor, contributed its expertise on adaptive control as it applies to flutter instabilities (Reference 5). The wind tunnel test was conducted during April 1982 in the NASA Langley Research Center's Sixteen-Foot Transonic Dynamics Tunnel. AFWAL and NASA engineers participated actively in the test program.

In this paper, a theoretical discussion of the adaptive technique precedes a description of the wind tunnel model and the instrumentation used to perform the test. Limited results from simulations that were carried out prior to the wind tunnel test are given and are followed by a description of the wind tunnel test results.

ADAPTIVE CONCEPTS

Two distinct adaptation algorithms were designed which correspond to the first two levels of adaptation discussed above. The first algorithm is identified as the Least Squares Detector and Discriminator (LSDD) and, as the name implies, uses a least squares fitting procedure to determine whether the system response corresponds to one of several prespecified flutter modes. If a correspondence is found, the second algorithm, the Maximum Likelihood Estimator (MLE) is engaged to provide a continuous updating of the flutter parameters which are then used to provide an appropriate feedback signal for flutter suppression.

Least Squares Detector and Discriminator

Figure 1 is a block diagram of the LSDD concept. The algorithm makes the decision as to whether one of a number of possible flutter modes exists for the aircraft. Detection is defined as determining whether any flutter mode exists while discrimination decides which of the several modes is present. The first step requires the construction of signals that combine the outputs of the wing accelerometers in a way (see Reference 5) that the resulting signals approximate the velocity of a flutter mode, if it exists. That is, the combination strives to produce a signal that has a Laplace transform of the form

$$\frac{y}{u} = \frac{K\omega e^{j\phi}}{s^2 + 2\zeta\omega s + \omega^2} \tag{1}$$

where y is the sensor output, u is the control surface input and ω, ξ, K and ϕ are, respectively, the frequency, damping, gain and phase of the flutter mode. The key to the successful performance of the adaptive algorithm is in providing an adequate estimate of the four latter parameters when a flutter condition exists.

The detector takes the output of this combination, after it has been passed through a bandpass filter, as well as information on the control surface position and fits these data to a model of the form

$$y_k + p_1 y_{k-1} + p_2 y_{k-2} = p_3 u_k + p_4 u_{k-1} \tag{2}$$

where k represents the discrete time step. The fit is performed by finding the vector (with components p_1, p_2, p_3 p_4) which minimizes

$$J = \sum_{k = k_0}^{k_0 + N} (y_k - p^T z_{k-1})^2 \tag{3}$$

where N is the length of the data segment and

$$z_{k-1} = (-y_{k-1}, -y_{k-2}, u_k, u_{k-1})^T \tag{4}$$

The least squares estimate of P that minimizes J is

$$\tilde{p} = \left(\sum z_{k-1} \, z_{k-1}^{T} \right)^{-1} \left(\sum z_{k-1} \, y_k \right) \tag{5}$$

and the minimum value of J is defined as J*. The accuracy of the least squares fit is defined to be

$$\tilde{J}^* = J^*/J_o, \quad J_o = \sum_{k = k_0}^{k_0 + N} (y_k)^2 \tag{6}$$

Thus, the output of the least squares detector and discriminator is the "goodness" of fit, J*, and the corresponding parameter vector $\tilde{p}$. The value of J* gives an indication of the dominance of an oscillation and the accuracy of the parameter estimate.

The values of $\tilde{p}$ can be used to calculate the frequency and damping of the flutter mode. A flutter mode is said to exist when each of the following four criteria is satisfied:

1) J_o is greater than a specified value

2) $\tilde{J}^*$ is less than a specified value

3) The frequency estimate is within a specified range and

4) The damping estimate is less than a specified value

If all four criteria are satisfied, the MLE is engaged. It is seen that the definitions of the criteria include specifications that can be thought of as parameters in the algorithm. As the discussion in the test results section of this paper indicates, the specification of these values was a major concern of the wind tunnel test. An additional parameter that required specification was the value of N in Equation 3. The tradeoffs involved are between speed and accuracy, and between irritating false alarms, i.e., the algorithm identifying a flutter condition when there is none, and the catastrophic failure of the algorithm to identify a flutter condition when there is one.

MAXIMUM LIKELIHOOD ESTIMATOR

It is conceptually possible to use the $\tilde{p}$ vector of Equation 5 to calculate all the parameters necessary to provide adequate control for the flutter condition. However, it was found in practice that the quality of the estimates was insufficient to provide reliable control. This motivated the search for an alternative scheme and the program of Reference 5 identified and mechanized the MLE technique for the flutter suppression application. Figure 2 is a block diagram of this concept. The accelerometer combination of the identified flutter mode is again used in combination with the control surface input to obtain estimates of the flutter parameters. These parameters are then sent to the flutter controller which develops a control law to suppress the flutter condition.

The analytical basis of the MLE algorithm starts with the recursive relation of Equation 2 restated in first order form:

$$\begin{Bmatrix} X_1 \\ X_2 \end{Bmatrix}_{k+1} = \begin{bmatrix} 0 & 1 \\ -p_2 & -p_1 \end{bmatrix} \begin{Bmatrix} X_1 \\ X_2 \end{Bmatrix}_k + \begin{bmatrix} p_3 \\ p_4 - p_1 \, p_3 \end{bmatrix} U_k \tag{7}$$

with $Y_k = (X_1)_k$ and initial conditions

$$\begin{Bmatrix} X_1 \\ X_2 \end{Bmatrix}_o = \begin{Bmatrix} p_5 \\ p_6 \end{Bmatrix} \tag{8}$$

where we have added two additional parameters for the unknown initial conditions. The MLE algorithm seeks the values of the six p parameters which minimize a likelihood function that is a combination of the natural logarithm of the likelihood function based on N samples and a penalty term added to keep the estimates in proximity of an a priori estimate.

$$L = (p - p_o)^T W_o (p - p_o) + \sum_{k = k_0}^{k_0 + N} \left[\nu_k^2 / B_k + \ell n |B_k| \right] \tag{9}$$

where ν_k is the residual $(y - \bar{X}_1)_k$ generated by a Kalman filter of the form

$$\begin{bmatrix} \bar{X}_1 \\ \bar{X}_2 \end{bmatrix}_{k+1} = \begin{bmatrix} 0 & 1 \\ -p_2 & -p_1 \end{bmatrix} \begin{bmatrix} \bar{X}_1 \\ \bar{X}_2 \end{bmatrix}_k + \begin{bmatrix} p_3 \\ p_4 - p_1 p_3 \end{bmatrix} U_k +$$

$$\begin{bmatrix} k_1 \\ k_2 \end{bmatrix} \left(y - \bar{X}_1 \right)_k \quad ; \quad \begin{bmatrix} X_1 \\ X_2 \end{bmatrix}_{k_0} = \begin{bmatrix} p_5 \\ p_6 \end{bmatrix} \tag{10}$$

and B_K is the convariance matrix of the residual sequence (assumed to be constant in this application).

The minimization task is performed using the Newton-Raphson technique to find the increment in the p vector which make the gradient of L zero:

$$\nabla^2 L \, \Delta p = - \nabla L \tag{11}$$

The stringent time constraints of the adaptive flutter suppression task mandates that a number of approximations be made in the Equation 11 calculation. A key approximation relates to the fact that the ν_k's are linear functions of p_3, p_4, p_5 and p_6. If p_1 and p_2 are thought of as being fixed, L is then quadratic in the remaining four parameters and the solution of Equation 11 does not require iteration. This approximation was implemented in the algorithm by fixing p_1 and p_2 for five successive updates of the p_3 through p_6 parameters and then updating p_1 through p_4 with p_5 and p_6 held fixed. The latter update does require solving Equation 11 for a perturbation in the p values since the ν_k are not linear values of p_1 and p_2.

Control Calculation

Once the six p parameters have been determined, the first four are used to calculate the physical parameters ω, ζ, K and ϕ of Equation 1. These parameters are used in turn to calculate the feedback signal that is used to control the flutter conditon. The analog form of the control signal is given by:

$$U = - \frac{2}{K} \left(\zeta_{CMD} - dc \, \zeta \right) e^{\imath (\phi_{CMD} - \phi)} y \tag{12}$$

where ζ_{CMD} is an algorithm input that specifies the damping level prescribed for the closed loop system, dc is a weighting factor applied to the damping estimate and ϕ_{CMD} is a phase term used to correct for phase lags that are not estimated by the algorithm. These lags can result from the control surface actuator and from delays introduced by the digital control.

MODEL AND INSTRUMENTATION

Figure 3 is a representation of the wind tunnel model used for the demonstration. This model had been used previously in the programs discussed in References 1 and 2 and these references describe the model in some detail. Therefore, only a basic description is given in this paper.

The model is a 30 percent scale half span model of the YF-17 and is mounted on roll bars which permit rigid body longitudinal degrees of freedom. The flutter suppression network basically entails feeding back compensated accelerometer (sensors in Figure 3) outputs to leading and/or trailing edge control surfaces. The adaptive tests were limited to using only the trailing edge surface. Unique features of the system include a "flutter detector," an electronic device that senses when large amplitude oscillatory responses occur, and a flutter stopper, which fires a mass inside the AIM-7S (Sparrow) missile located on the outboard pylon. When the mass is deployed, the flutter mechanism of this configuration is disrupted.

For the adaptive test, an additional store, representing an AIM-9S (Sidewinder) was designed to be releasable from the wing tip launch rail. When this missile was installed on the model, the configuration, which was designated the take off condition, had a flutter speed that was very high. When the missile was ejected by a remote activating switch, the resulting configuration, designated the

downloaded condition, had a relatively low flutter speed. The release of the store at a speed above the flutter speed of the downloaded configuration imposed a severe test on the adaptive control algorithm's ability to detect and control the resulting flutter condition.

Figure 4 depicts the entire flutter suppression system as it was installed at the test site. In the center of the figure is the control console which interconnected all the components of the system. The SEL 32/55 digital computer executed the adaptive control algorithm. This computer is a true 32 bit machine with a floating-point processor. Communication with the wind tunnel model via the control console was performed using 12 bit analog to digital and digital to analog converters. Other features of the system include a hydraulic pump to power the actuators, a trim controller which drives the horizontal tail and various monitoring instruments, including a Hewlett-Packard Fourier Analyzer.

SIMULATION

A key factor in the success of the program was the simulations performed prior to the wind tunnel entry. Honeywell performed one simulation that checked out the adaptive algorithms' performance on an aircraft model with a computer operating in the batch mode. This assisted in the programming and debugging of the algorithm and provided initial insight into the effect of various algorithm parameters.

A more complete, real time simulation was carried out by Northrop that included all the hardware that was used in the wind tunnel demonstration. The behavior of the airframe in the airstream was accounted for either by simulating it on a twin processor of the SEL computer that contained the adaptive algorithm, or by using FM tape data that had been recorded during previous wind tunnel tests.

This simulation served a number of functions. For instance, it assisted in debugging the installation of the algorithm on the SEL computer. Perhaps the most important use of the simulation was to provide information on the algorithms' computational requirements. The wind tunnel test discussed in Reference 3 had shown that 10 milliseconds was a maximum frame time that could provide adequate digital control of the 6.0 Hz flutter mode. The initial version of the MLE algorithm was found to require a maximum of 30 msecs. of computational time. A significant reprogramming effort was required to distribute the MLE computations among a number of time frames and thereby satisfy the 10 msec requirement.

The simulation also proved invaluable in checking out all the interconnections required by the test equipment and in adjusting the scale factors applied in the analog to digital and digital to analog conversions.

Figure 5 shows strip chart traces from a simulation which included a computer simulation of the unstable airframe. The figure shows that the LSDD algorithm quickly identified the unstable condition and invoked the correct controller. The maximum likelihood estimator (MLE) then continuously monitored the sensor output, computing new parameter estimates every five samples. The latest estimates were used to compute revised gain and phase parameters for the controller. In the figure, there is a perturbation in the time histories that occurred when the control loop was opened intentionally. It is seen that the algorithm quickly recovered when the loop was closed.

TEST RESULTS

The wind tunnel test took place in April 1982 at the NASA Langley Research Center's Transonic Dynamics Tunnel and was comprised of six days of wind-on testing. Despite the limited testing time, a number of significant achievements were demonstrated. Among these were:

1. The Least Squares Detection and Discrimination Algorithm was able to correctly identify an impending flutter condition in a timely manner.

2. The Maximum Likelihood Estimator algorithm was demonstrated to be capable of providing rapid estimates of key parameters and providing an effective control of the flutter condition over a broad range of test conditions.

3. The flutter detector and flutter stopper performed superbly, allowing for testing up to a flutter condition with minimal risk to the model.

4. In a culmination of the test activities, a Sidewinder missile was released from the wing tip launcher. The resulting configuration was violently unstable. The adaptive algorithm was able to identify this instability and provide adequate control in a fraction of a second.

A large proportion of the testing time was devoted to identifying the combination of the large number of program parameters that resulted in the best algorithm performance. Once an acceptable combination was found, flutter sweeps were performed that started at a subcritical test condition, then penetrated the flutter boundary with the LSDD identifying the flutter behavior and engaging the MLE. The sweep was then continued to higher dynamic pressure levels until either the response became too violent for the safety of the model or the limits on the control surface travel were reached. Figure 6 shows a composite of the results of this testing. It shows that the adaptive algorithm was able to stabilize the flutter condition over a wide range of Mach numbers and dynamic pressures.

Figure 7 shows a strip chart record that provides some insight into a key aspect of the algorithms, the generation of the flutter mode (Figure 2) signals. The first strip shows the output of an accelerometer as it was obtained from the model. The second strip is the same record after it has been passed through an analog anti-aliasing filter with a 50 Hz cutoff frequency. The third strip is this signal after it has been digitized while the fourth trace is the flutter mode, obtained by blending the outputs of the four accelerometers and passing the resultant signal through a band pass filter. It is seen that whereas the six Hertz flutter mode is masked by other responses in the original accelerometer output, the final flutter mode signal is very clear.

The fifth strip on Figure 7 shows the trailing edge position record as it was measured from a control surface potentiometer and the sixth is the same signal after it has been digitized and filtered. This last trace is the one used in combination with the fourth trace for parameter estimation.

Smoothing

By its nature, adaptive control makes quantization of the algroithm's performance difficult. Measurement techniques used in previous studies that provided transfer function, power spectral density and damping trend data are not applicable to adaptive control testing since the feedback parameters are changing constantly. What follows then is a more qualitative assessment of the test results than is normally given in a paper of this type.

One of the lessons learned during the tunnel test was that there were significant variations in the parameter estimates obtained every 50 msecs by the MLE algorithm. These variations were attributed to the fact that the turbulent environment of the tunnel gave a low signal to noise ratio. The average values of the estimates appeared acceptable and these average values were obtained by applying a smoothing filter to the estimates. The smoothing filter used was a standard first order low pass filter developed for digital computers and has the equation:

$$\bar{p}_{k+1} = \beta\, \bar{p}_k + (1-\beta)\, p_{k+1}$$

where the k subscript designates the time point, the bar superscript refers to the smoothed estimate and β is the smoothing parameter, which can vary from 0 (no smoothing) to 1 (no updating).

The selection of the appropriate β values became a major tradeoff activity of the wind tunnel test. No smoothing filters were applied in the Least Squares portion of the algorithm while five filters were ultimately applied in the Maximum Likelihood portion. These filters can be classified into two sets. The first set was incorporated into the parameter estimation process (Equations 7 through 11) and the second set was incorporated into the updating of the control law (Equation 12)

Nominal values of the five β's were

Parameter(s)	β Value
p_1, p_2	0.6
p_3, p_4	0.4
K	0.94
ζ	0.98
ϕ	0.92

As the list implies, it was necessary to smooth the damping estimate by the largest amount. The variability of the damping estimate was one of the more unpleasant surprises of the test and prompted the majority of the improvisations that took place during the test.

Parameter Variations

The smoothing filters required a change in the MLE algorithm during the test. Other changes were made during the test in the parameters of both adaptive algorithms. A number of these parameters will be discussed briefly here in order to give more insight into the algorithms.

The value of the N parameter of Equation 3 and Equation 9 represented a tradeoff between the quality of the estimates and their timeliness. Values of 60 to 100 were used which, with a sample time of .01 secs, means that the data window varied from 0.6 to 1.0 secs.

A parameter denoted SIGUT controlled the amplitude of the test signal that was applied to the control surface. In this case, the tradeoff was between obtaining a good response signal with a large value of SIGUT and keeping SIGUT small enough so that the test signal did not drive the model too hard or exceed the control surface's capability. The parameter was set so that the peak magnitude of the excitation was approximately 1.5° for the LSDD algorithm and 3.0° for the MLE algorithm.

Parameters ZCMD and DC correspond to ζ_{CMQ} and dc in Equation 12. The nominal value of ZCMD was set at 0.02, implying a request for 2% damping of the critical mode for the closed loop system. The DC value was decreased from 1.5 to 1.0 during the course of the test.

Other parameters controlled the detection parameters discussed in the description of the LSDD algorithm, limited the amount of parameter estimates could vary, emphasized initial values of the parameters to be estimated and provided initial gain and phase estimates to the MLE algorithm.

This list of parameters, which is still only a fraction of those required by the algorithm, gives a sense of the complexity of the adaptive algorithm. Since the wind tunnel test was the first opportunity to test the algorithm in "real world" conditions, it is not surprising that a large amount of trial and error was required to obtain satisfactory performance.

Store Release

The most demanding goal of the test was to demonstrate the ability of the adaptive algorithm to detect and control a flutter condition that was entered into abruptly due to a store release. This goal was achieved during the test entry when a Sidewinder missile was released from the wing tip of the model with the resulting configuration violently unstable. The test point corresponding to this event is marked by a square in Figure 6. The LSDD algorithm recognized this instability very quickly and engaged the MLE algorithm, which stabilized the condition. Figures 8 through 10 are strip chart records of this event and provide insight into the performance of the algorithm. Figures 8 through 10 were reconstructed from the data that were tape recorded during the test since the quality of the oscillograph recordings obtained during the test was poor. The nature of the responses in the reconstruction is very similar to those obtained during the test. Figure 8 shows variables from the digital algorithm. Before the store drop, frequency and damping estimates were made every 0.3 seconds. It is impossible to pinpoint the exact moment of the store drop on this figure, but from studying all the data one can deduce that there was an approximately 0.2 second delay between the store's release and the engaging of the trailing edge surface control. This implies that the LSD algorithm detected the flutter condition at its first opportunity after the store drop. The damping estimate is seen in Figure 8 to go negative after which the MLE algorithm nominally estimates the open loop damping to be a negative one-half percent of the critical damping level. The large discrepancy between the magnitude of the damping estimates given by the MLE and LSD algorithms remains a puzzling factor. Other strips of Figure 8 show that the unfiltered estimates of gain and phase fluctuate greatly, motivating the need for the smoothing filters discussed earlier. The filtered estimates are seen in Figure 9 to be well-behaved. It should be pointed out that Figures 8 and 9 were obtained on two different passes of the tape data through the adaptive algorithm. It is seen that the common strips on the two figures do not correspond exactly. It is, however, reassuring that there is strong resemblance in the records, indicating that the algorithm outputs are repeatable.

CONCLUDING REMARKS

The test demonstration of adaptive control of flutter represented an ambitious advance in active control technology. To the best of our knowledge, this is the first time such a demonstration has been made on an elastically unstable system. It is very gratifying, therefore, that the major goals of the project, i.e., the demonstration of the LSDD and MLE algorithms and of the adaptation to the store release, were met during the test. This sense of accomplishment is reinforced when one considers that the test was carried out under two severe time constraints: 1) the contraint that the adaptive calculations to be made within the 10 millisecond frame time with a digital computer of moderate speed performance, and 2) the constraint that the wind tunnel test was limited to six days.

On the other hand, it must be stressed that this first demonstration should not be thought of as the final word. The performance rating of the adaptive test was considered moderate in both the quality of the parameter estimates obtained by the algorithms and in the range of test conditions over which the algorithms stabilized the model. Improvement in each of these areas is required before flight tests using the adaptive control algorithms can be safely attempted. The data recorded on FM tape during the test is a valuable resource that can be utilized in the search for this improvement.

An important factor in obtaining these improvements is the continued rapid advance in the capabilities of digital computers. The most recent laboratory minicomputers have computational speed capabilities an order of magnitude faster than the computer used in this demonstration. Even further efficiencies could be obtained by using an array processor to speed the vector operations. The use of these state of the art devices would allow more detailed and exact calculations in the MLE algorithm, with a resulting improvement in the parameter estimates and hence the controller's capability.

While the computer gains will provide a dramatic advance in the technology, its viability can come only after a number of incremental improvements in the algorithm and greater understanding of the basic phenomena with a flight test providing the ultimate demonstration.

REFERENCES

1. Hwang, C., Winther, B.A., Noll, T.E., and Farmer, M.G., "Demonstration of Active Wing/Store Flutter Suppression System," AGARD R-668, July 1978.

2. Hwang, C., Johnson, E.H., Mills, G.R., Noll, T.E., and Farmer, M.G., "Wind Tunnel Test of a Fighter Aircraft Wing/Store Flutter Suppression System - An International Effort," in AGARD R-689, August 1980.

3. Johnson, E.H., Hwang, C., Joshi, D.S., Kesler, D.F., and Harvey, C.A., "Test Demonstration of Digital Control of Wing/Store Flutter," AIAA CP82-0645, AIAA/ASME/ASCE/AHS 23rd Structures, Structural Dynamics and Materials Conference, New Orleans, LA., May 1982.

4. Hwang, C., and Johnson, E.H., "Test Demonstration of Digital Adaptive Control of Wing/Store Flutter, Part I: Demonstration of Digital Control," AFWAL TR-82-3044, July 1982.

5. Harvey, C.A., Johnson, T.L., and Stein, G., "Adaptive Control of Wing/Store Flutter," AFFDL TR-79-8081, April 1979.

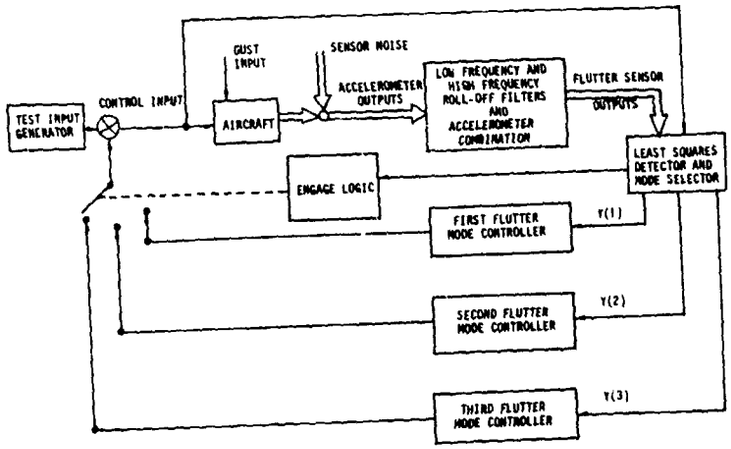

Figure 1. Least Squares Detector and Discriminator Adaptive Control Concept.

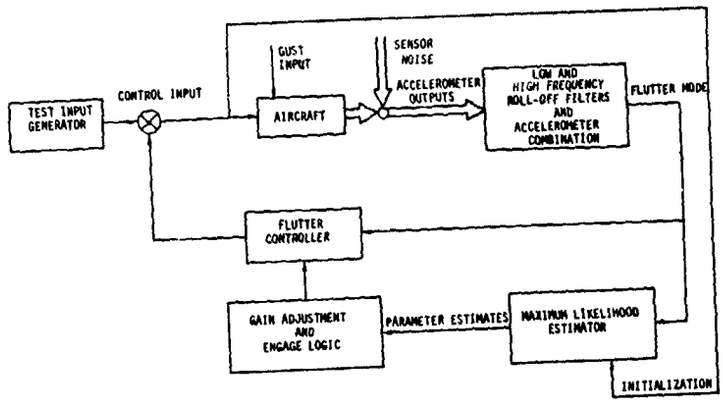

Figure 2. Maximum Likelihood Estimator Adaptive Control Concept.

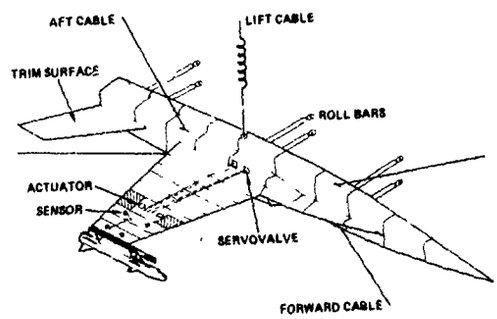

Figure 3. The Wing/Store Flutter Suppression Model.

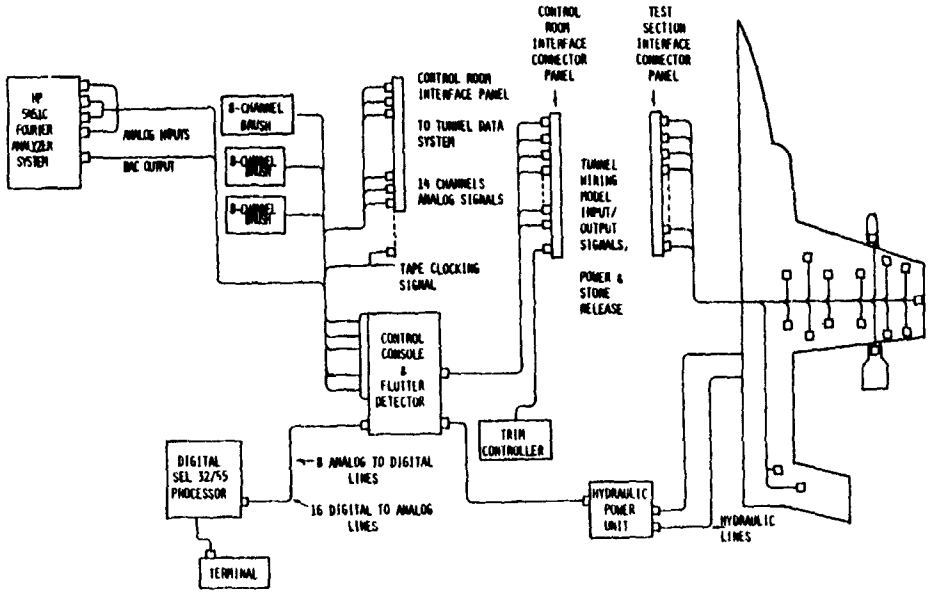

Figure 4. Flutter Suppression System as Installed at the Test Site.

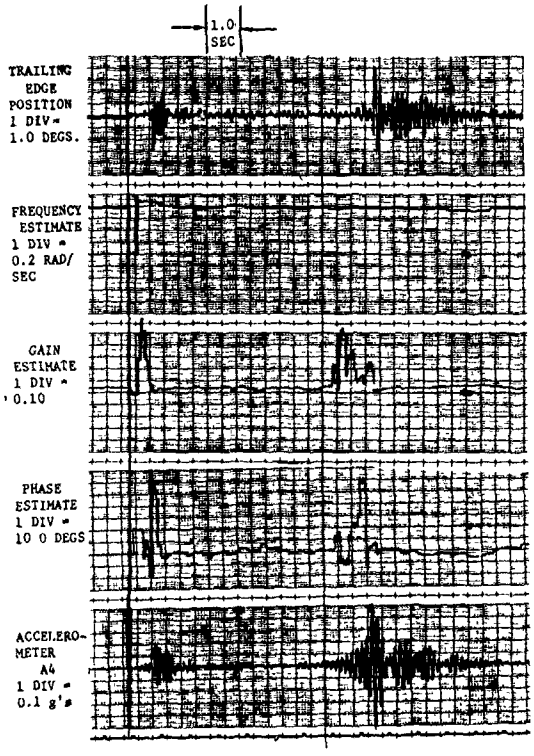

Figure 5. Time History showing the Adaptive Algorithms Performance When Applied to a Simulation of the Unstable Airframe.

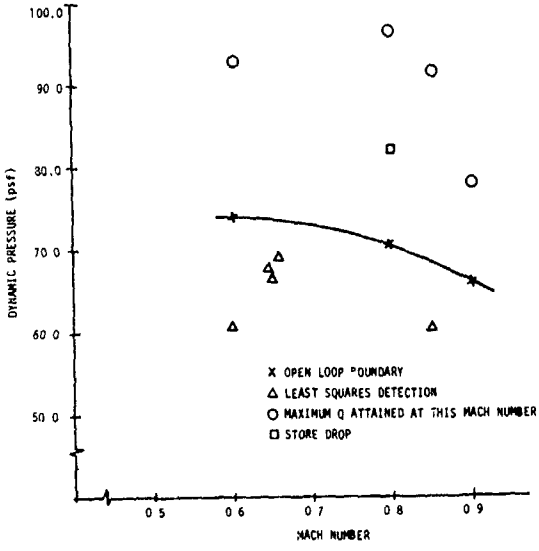

Figure 6. Performance of the Adaptive Algorithms in Expanding the Flight Envelope.

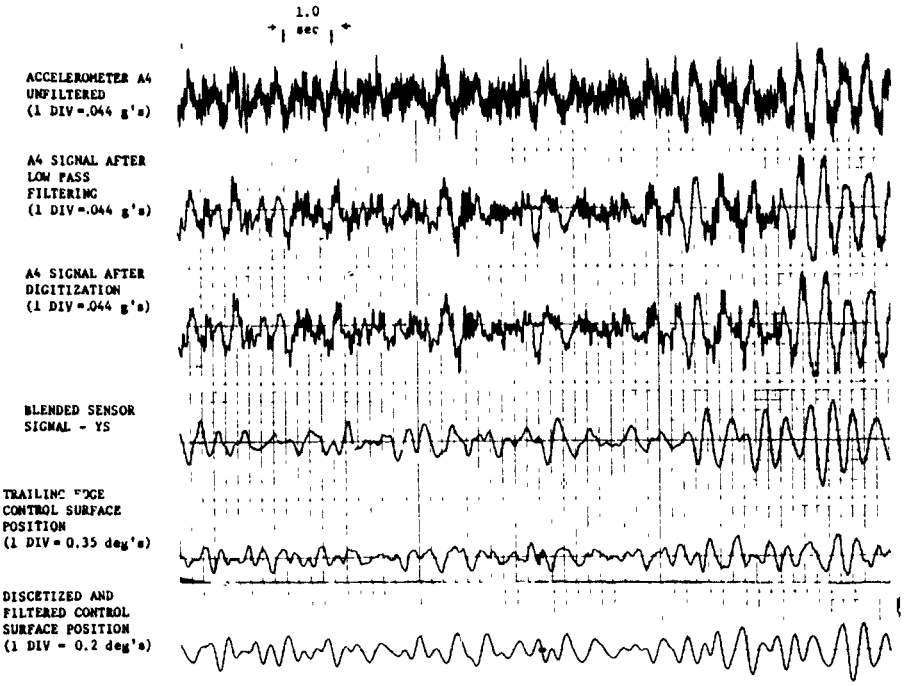

Figure 7. Generation of Signals Used in the Estimation Process.

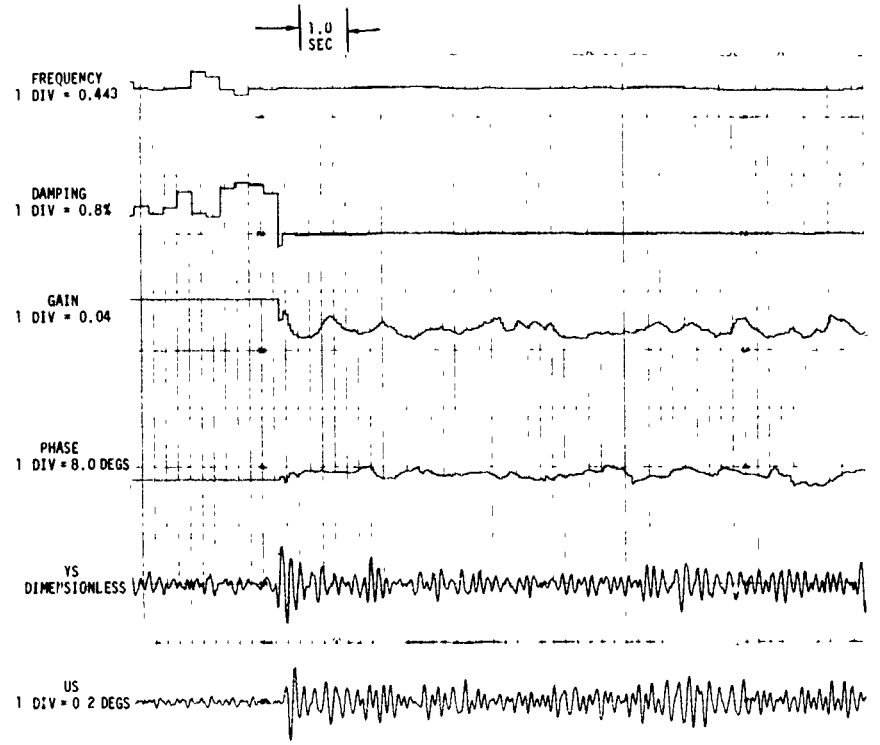

Figure 8. Time Histories of Selected Digital Outputs During the Score Release.

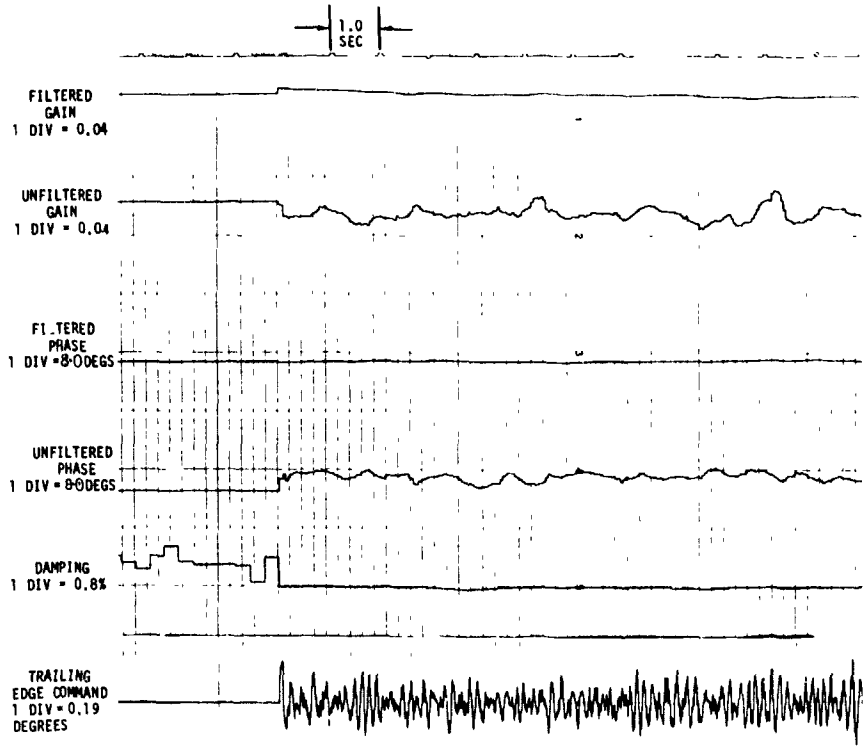

Figure 9. Additional Time Histories of Selected Digital Outputs During the Store Release.

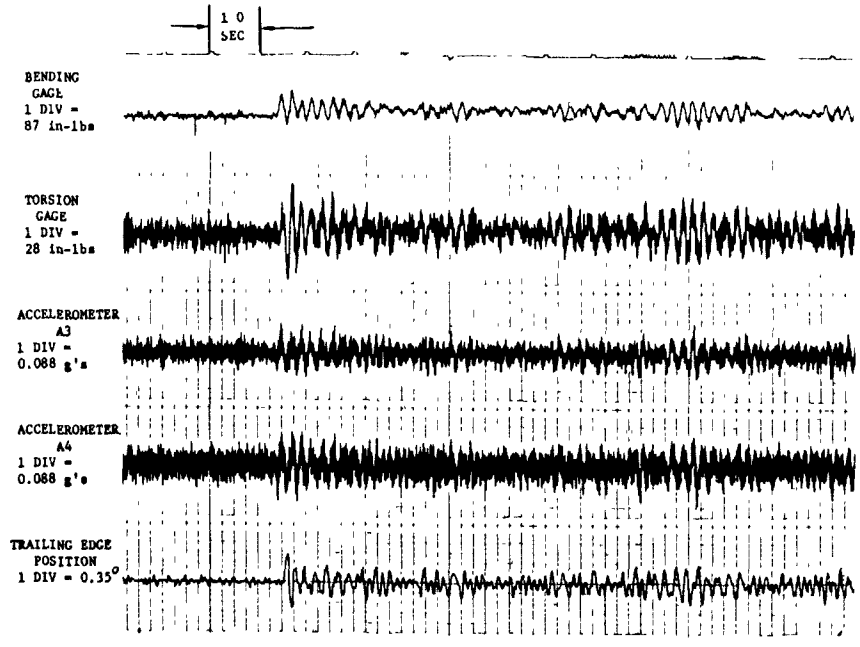

Figure 10. Time Histories of Selected Sensor Outputs During the Store Release.

REPORT DOCUMENTATION PAGE			
1. Recipient's Reference	2. Originator's Reference	3. Further Reference	4. Security Classification of Document
	AGARD-R-703	ISBN 92-835-1443-2	UNCLASSIFIED

5. Originator	Advisory Group for Aerospace Research and Development North Atlantic Treaty Organization 7 rue Ancelle, 92200 Neuilly sur Seine, France
6. Title	RECENT TRANSONIC FLUTTER INVESTIGATIONS FOR WINGS AND EXTERNAL STORES
7. Presented at	the 56th Structures and Materials Panel Meeting held in Toronto, Canada in September 1982.

8. Author(s)/Editor(s)	9. Date
Various	January 1983
10. Author's/Editor's Address	**11. Pages**
Various	66

12. Distribution Statement	This document is distributed in accordance with AGARD policies and regulations, which are outlined on the Outside Back Covers of all AGARD publications.

13. Keywords/Descriptors

Wings	Aeroelasticity
External stores	Transonic characteristics
Flutter	

15. Abstract

This publication includes ~~four~~ 4 papers given to the Aeroelasticity Sub-Committee of the Structures and Materials Panel; they show a cross section of recent activities by NATO countries within the aeroelastic field.

Topics covered are
(1) Subsonic flutter clearance procedures in Canada
(2) Transonic flutter research in Germany
(3) Transonic unsteady aerodynamic measurements in the United States
(4) The use of adaptive control methods to actively suppress flutter of an aeroelastic model wing with a store.

The papers reflect the strides being made in aeroelasticity by the NATO countries.

AGARD Report No.703 Advisory Group for Aerospace Research and Development, NATO RECENT TRANSONIC FLUTTER INVESTIGATIONS FOR WINGS AND EXTERNAL STORES Published January 1983 66 pages This publication includes four papers given to the Aeroelasticity Sub-Committee of the Structures and Materials Panel; they show a cross section of recent activities by NATO countries within the aeroelastic field. Topics covered are (i) Subsonic flutter clearance procedures in Canada P.T.O	AGARD-R-703 Wings External stores Flutter Aeroelasticity Transonic characteristics	AGARD Report No.703 Advisory Group for Aerospace Research and Development, NATO RECENT TRANSONIC FLUTTER INVESTIGATIONS FOR WINGS AND EXTERNAL STORES Published January 1983 66 pages This publication includes four papers given to the Aeroelasticity Sub-Committee of the Structures and Materials Panel, they show a cross section of recent activities by NATO countries within the aeroelastic field. Topics covered are (i) Subsonic flutter clearance procedures in Canada P.T O	AGARD-R-703 Wings External stores Flutter Aeroelasticity Transonic characteristics
AGARD Report No.703 Advisory Group for Aerospace Research and Development, NATO RECENT TRANSONIC FLUTTER INVESTIGATIONS FOR WINGS AND EXTERNAL STORES Published January 1983 66 pages This publication includes four papers given to the Aeroelasticity Sub-Committee of the Structures and Materials Panel, they show a cross section of recent activities by NATO countries within the aeroelastic field. Topics covered are (i) Subsonic flutter clearance procedures in Canada P.T.O	AGARD-R-703 Wings External stores Flutter Aeroelasticity Transonic characteristics	AGARD Report No.703 Advisory Group for Aerospace Research and Development, NATO RECENT TRANSONIC FLUTTER INVESTIGATIONS FOR WINGS AND EXTERNAL STORES Published January 1983 66 pages This publication includes four papers given to the Aeroelasticity Sub-Committee of the Structures and Materials Panel; they show a cross section of recent activities by NATO countries within the aeroelastic field. Topics covered are (i) Subsonic flutter clearance procedures in Canada P T O	AGARD-R-703 Wings External stores Flutter Aeroelasticity Transonic characteristics

(ii) Transonic flutter research in Germany
(iii) Transonic unsteady aerodynamic measurements in the United States
(iv) The use of adaptive control methods to actively suppress flutter of an aeroelastic model wing with a store.

The papers reflect the strides being made in aeroelasticity by the NATO countries.

Papers presented at the 56th Structures and Materials Panel Meeting held in Toronto, Canada in September 1982

ISBN 92-835-1443-2

(ii) Transonic flutter research in Germany
(iii) Transonic unsteady aerodynamic measurements in the United States
(iv) The use of adaptive control methods to actively suppress flutter of an aeroelastic model wing with a store.

The papers reflect the strides being made in aeroelasticity by the NATO countries.

Papers presented at the 56th Structures and Materials Panel Meeting held in Toronto, Canada in September 1982.

ISBN 92-835-1443-2

(ii) Transonic flutter research in Germany
(iii) Transonic unsteady aerodynamic measurements in the United States
(iv) The use of adaptive control methods to actively suppress flutter of an aeroelastic model wing with a store.

The papers reflect the strides being made in aeroelasticity by the NATO countries

Papers presented at the 56th Structures and Materials Panel Meeting held in Toronto, Canada in September 1982.

ISBN 92-835-1443-2

(ii) Transonic flutter research in Germany
(iii) Transonic unsteady aerodynamic measurements in the United States
(iv) The use of adaptive control methods to actively suppress flutter of an aeroelastic model wing with a store.

The papers reflect the strides being made in aeroelasticity by the NATO countries

Papers presented at the 56th Structures and Materials Panel Meeting held in Toronto, Canada in September 1982.

ISBN 92-835-1443-2

B203
4

AGARD
NATO OTAN
7 RUE ANCELLE · 92200 NEUILLY-SUR-SEINE
FRANCE
Telephone 745.08.10 · Telex 610176

DISTRIBUTION OF UNCLASSIFIED AGARD PUBLICATIONS

AGARD does NOT hold stocks of AGARD publications at the above address for general distribution. Initial distribution of AGARD publications is made to AGARD Member Nations through the following National Distribution Centres. Further copies are sometimes available from these Centres, but if not may be purchased in Microfiche or Photocopy form from the Purchase Agencies listed below.

NATIONAL DISTRIBUTION CENTRES

BELGIUM
Coordonnateur AGARD – VSL
Etat-Major de la Force Aérienne
Quartier Reine Elisabeth
Rue d'Evere, 1140 Bruxelles

CANADA
Defence Science Information Services
Department of National Defence
Ottawa, Ontario K1A 0K2

DENMARK
Danish Defence Research Board
Østerbrogades Kaserne
Copenhagen Ø

FRANCE
O.N.E.R.A. (Direction)
29 Avenue de la Division Leclerc
92320 Châtillon sous Bagneux

GERMANY
Fachinformationszentrum Energie,
Physik, Mathematik GmbH
Kernforschungszentrum
D-7514 Eggenstein-Leopoldshafen 2

GREECE
Hellenic Air Force General Staff
Research and Development Directorate
Holargos, Athens

ICELAND
Director of Aviation
c/o Flugrad
Reykjavik

ITALY
Aeronautica Militare
Ufficio del Delegato Nazionale all'AGARD
3, Piazzale Adenauer
Roma/EUR

LUXEMBOURG
See Belgium

NETHERLANDS
Netherlands Delegation to AGARD
National Aerospace Laboratory, NLR
P.O. Box 126
2600 A.C. Delft

NORWAY
Norwegian Defence Research Establishment
Main Library
P.O. Box 25
N-2007 Kjeller

PORTUGAL
Direcção do Serviço de Material
da Força Aerea
Rua da Escola Politécnica 42
Lisboa
Attn: AGARD National Delegate

TURKEY
Department of Research and Development (ARGE)
Ministry of National Defence, Ankara

UNITED KINGDOM
Defence Research Information Centre
Station Square House
St. Mary Cray
Orpington, Kent BR5 3RE

UNITED STATES
National Aeronautics and Space Administration (NASA)
Langley Field, Virginia 23365
Attn: Report Distribution and Storage Unit

THE UNITED STATES NATIONAL DISTRIBUTION CENTRE (NASA) DOES NOT HOLD STOCKS OF AGARD PUBLICATIONS, AND APPLICATIONS FOR COPIES SHOULD BE MADE DIRECT TO THE NATIONAL TECHNICAL INFORMATION SERVICE (NTIS) AT THE ADDRESS BELOW.

PURCHASE AGENCIES

Microfiche or Photocopy
National Technical
Information Service (NTIS)
5285 Port Royal Road
Springfield
Virginia 22161, USA

Microfiche
Space Documentation Service
European Space Agency
10, rue Mario Nikis
75015 Paris, France

Microfiche or Photocopy
British Library Lending
Division
Boston Spa, Wetherby
West Yorkshire LS23 7BQ
England

Requests for microfiche or photocopies of AGARD documents should include the AGARD serial number, title, author or editor, and publication date. Requests to NTIS should include the NASA accession report number. Full bibliographical references and abstracts of AGARD publications are given in the following journals:

Scientific and Technical Aerospace Reports (STAR)
published by NASA Scientific and Technical
Information Facility
Post Office Box 8757
Baltimore/Washington International Airport
Maryland 21240, USA

Government Reports Announcements (GRA)
published by the National Technical
Information Services, Springfield
Virginia 22161, USA

Printed by Specialised Printing Services Limited
40 Chigwell Lane, Loughton, Essex IG10 3TZ

ISBN 92-835-1443-2